Disentangling the Effects of Mergers and Interactions on Bar Formation and Evolution

by

Alexander Joseph Cooke

A thesis submitted in partial fulfilment of the requirements of
Liverpool John Moores University
for the degree of
Doctor of Philosophy

September 2026

Declaration

The work presented in this thesis was carried out at the Astrophysics Research Institute, Liverpool John Moores University. Unless otherwise stated, it is the original work of the author.

While registered as a candidate for the degree of Doctor of Philosophy, for which submission is now made, the author has not been registered as a candidate for any other award. This thesis has not been submitted in whole, or in part, for any other degree.

Alexander Joseph Cooke

Astrophysics Research Institute

Liverpool John Moores University

IC2, Liverpool Science Park

146 Brownlow Hill

Liverpool

L3 5RF

UK

September 2026

Abstract

Bars in disc galaxies are drivers of secular evolution. They are greatly affected in turn by their surroundings, from the immediate influences of the stars, gas and dark matter within their radius to the tidal forces introduced by nearby external galaxies. In this thesis, I investigate the relative importance of these scales of influence on the bar, disentangling the effects of galaxy mergers and interactions from the effects of the host galaxy on its bar. I use the Auriga suite of Milky Way-mass magneto-hydrodynamical cosmological zoom-in simulations to do so, including high temporal resolution reruns for a detailed view of changes in the bar.

I first examine bar formation in the Milky Way using a case study from the Auriga suite with similar present-day chemo-dynamical properties, a consistent bar formation time, and a similar merger history including an analogue for the Gaia-Enceladus/Sausage (GES) merger. I also rerun this simulation from redshift 4 with the GES analogue removed to highlight the effects of the merger. In the original simulation, the GES-like merger event triggers tidal forces on the disc, gas inflows and a burst of star formation, with the formation of a bar occurring within 1 Gyr of the first pericentre. In contrast, the rerun delays bar formation by over 2 Gyr, indicating a strong possibility of the real Milky Way's bar forming around the epoch of the GES merger due to tidal forces on its first pericentre. The rerun also indicates that the GES merger may have been responsible for continued radial growth in the Milky Way disc. I additionally find that, in other Auriga galaxies with GES-like merger events, those with stellar mass ratios below 10% form bars within 1 Gyr of the merger, while bar formation is delayed in the more massive merger scenarios. These include the 4 oldest bars in the simulation suite, reinforcing the importance of GES to the Milky Way bar.

I next investigate the influences on the evolution of bar pattern speed in Milky Way-mass galaxies across the full Auriga suite. I specifically calculate the bar pattern speed and the bar rotation rate – the ratio of corotation radius to bar length – at the time of bar formation and at $z = 0$, and compare these to bar age, bar strength, baryon dominance, galaxy stellar mass, and the history of external galaxy interactions. I find that galaxies which are more baryon dominated at $z = 0$ – and which lie above the observed stellar mass-halo mass abundance matching relation – host faster bars, while more dark matter dominated galaxies host slower bars. Baryon-dominated galaxies also form their bars earlier and their rotation rates stay constant or even decrease over time. This leads to older bars being faster than their younger counterparts – in contrast to the expectation of bar slow-down from dynamical friction imparted by the dark matter halo. I also find a trend in stellar mass, with 'faster' bars being hosted in more massive galaxies, which could be driven by the underlying higher baryon-dominance of more massive galaxies. Furthermore, I find that external interactions correlate with lower bar rotation rates, particularly for strong interactions that occur around bar formation time. However, this correlation is relatively weak, leaving internal baryon dominance as the main driver of fast bar rotation rates.

Lastly, I evaluate the applicability of the Tremaine-Weinberg (TW) method – the primary model-independent method for finding pattern speeds from observations – to the fast, cosmologically motivated bars in the Auriga suite. I find that the method is generally accurate to within 10% for the majority of systems. Nevertheless, with the exception of one double-barred system with large error, I find that the greatest errors in the TW method arise from warps in the disc. I determine that the effect of these warps on errors in the TW method is greatest at angles where the warp is most visible in the plane of the sky. These warps reach the inner disc, so I also reanalyse these results as errors in inclination and position angle of the disc. I find that, while inclination errors have little effect, the errors in the TW method produced by position angle errors are greater than those previously found in idealised simulations.

Publications

In the course of completing the work presented in this thesis, the contents of Chapter 3 have been submitted and accepted for publication in a refereed journal, in Paper 1 below, as have the contents of Chapter 4, in Paper 2 below (using the name Alex Merrow). Additionally, the contents of Chapter 5 are based on a publication which is currently in preparation, Paper 3 below:

Paper 1: 'Did the Gaia Enceladus/Sausage merger form the Milky Way's bar?', **Merrow A.**, Grand R. J. J., Fragkoudi F. & Martig M., 2024, Monthly Notices of the Royal Astronomical Society, 531, 1520.

Paper 2: 'What drives bar rotation? The effect of internal properties and galaxy interactions on bar pattern speeds', **Merrow A.**, Fragkoudi F., Grand R. J. J. & Martig M., 2026, Monthly Notices of the Royal Astronomical Society, 547, stag371.

Paper 3: 'The reliability of the Tremaine-Weinberg method in a fast-barred cosmological simulation', **Merrow A.**, Grand R. J. J., Fragkoudi F. & Martig M., in prep.

During this period of research, I also published Paper 4, following on from my undergraduate research. This research is not presented in this thesis, since some of its content was submitted for my undergraduate degree:

Paper 4: 'The lives and deaths of faint satellite galaxies around M31', **Merrow A.**, Oman K. A. & Fattahi A., 2026, Monthly Notices of the Royal Astronomical Society, 548, stag558.

Acknowledgements

Firstly, I would like to thank Robert Grand and Francesca Fragkoudi, who have been incredible, dedicated supervisors. Discussions with you both have been the cornerstone of this research and I have valued your ideas greatly. Thank you also to Marie Martig, for valuable feedback on the presentation and formulation of my research at all stages. And thanks too to the galactic dynamics group at Durham University, run by Francesca Fragkoudi and Dimitri Gadotti, who have helped with community and discussion through my research.

I would not be here at this stage without my wonderful wife, Lorna, who has kept me going and been responsible for so much of my happiness throughout this degree, and to her mother, who has given me the sanctuary of a family through it all.

Contents

Declaration ii

Abstract iii

Publications v

Acknowledgements vi

List of Figures x

1 Introduction 1
- 1.1 Galaxy morphology . . . 1
- 1.2 Bar formation . . . 3
- 1.3 Bar angular momentum . . . 5
- 1.4 The impact of galaxy interactions on galaxy structure . . . 7
- 1.5 The use of simulations . . . 9
  - 1.5.1 Limitations . . . 10
- 1.6 Thesis overview . . . 12

2 Methodology 13
- 2.1 The Auriga simulations . . . 13
  - 2.1.1 The `Original`/4 and `LowMassMws`/4 suites . . . 13
  - 2.1.2 High temporal resolution reruns . . . 15
- 2.2 Galaxy and interaction properties . . . 19
  - 2.2.1 Disc and bar parameters . . . 19
    - 2.2.1.1 Disc and bar angle . . . 19
    - 2.2.1.2 Bar formation time . . . 21
    - 2.2.1.3 Rotation rate . . . 22
    - 2.2.1.4 Further galaxy properties . . . 25
  - 2.2.2 Galaxy interaction parameters . . . 26

3 Did the Gaia Enceladus/Sausage merger form the Milky Way's bar? 30
- 3.1 Simulations used . . . 30
  - 3.1.1 Auriga 18 . . . 30

3.1.2 Re-simulation . . . 32
3.2 Results . . . 33
3.2.1 Bar formation in Auriga 18 . . . 33
3.2.2 Comparison to a controlled counterpart simulation . . . 39
3.3 Discussion . . . 43
3.3.1 The link between GES and the Milky Way's bar . . . 43
3.3.1.1 Tidal bar formation . . . 44
3.3.1.2 Accelerated internal bar formation . . . 46
3.3.1.3 The wider Auriga simulations . . . 47
3.3.2 GES and the growth of the Milky Way's disc . . . 50
3.4 Conclusions . . . 53

4 What drives bar rotation? The effect of internal properties and galaxy interactions on bar pattern speeds 55
4.1 Results . . . 55
4.1.1 Evolution of bar properties . . . 56
4.1.2 The effect of changes in the host galaxy . . . 59
4.1.2.1 Global galaxy composition . . . 62
4.1.2.2 Baryon dominance in the inner regions . . . 63
4.1.3 The effect of galaxy interactions . . . 65
4.2 Discussion . . . 70
4.2.1 Decreasing rotation rates . . . 70
4.2.2 Comparison with observations . . . 75
4.3 Conclusions . . . 78

5 The reliability of the Tremaine-Weinberg method in a fast-barred cosmological simulation 80
5.1 Introduction to the Tremaine-Weinberg method . . . 80
5.2 Applying the Tremaine-Weinberg method . . . 85
5.3 Results and discussion . . . 88
5.3.1 The effects of warped discs . . . 88
5.3.2 Disc position angle . . . 95
5.4 Conclusions . . . 98
5.4.1 Future work . . . 99

6 Summary and Conclusions 100
6.1 Did GES form the Milky Way's bar? . . . 101
6.2 What drives bar rotation? . . . 102
6.3 The reliability of the Tremaine-Weinberg method . . . 103

A Comprehensive correlations 105

Bibliography **108**

List of Figures

1.1 An illustration of the Hubble sequence. 2

2.1 RGB coloured images of high temporal resolution reruns from Auriga - 1 through 12. 16
2.2 RGB coloured images of high temporal resolution reruns from Auriga - 13 through 25. 17
2.3 RGB coloured images of high temporal resolution reruns from Auriga - 26 through low-mass-run 10. 18
2.4 Summary of the main bar parameters used for halo 22 of the Auriga simulations plotted against lookback time. 20
2.5 An illustration of the ellipse method for finding the bar length for Auriga 24 at $z = 0$. 23
2.6 An illustrative example of the Elmegreen parameter calculation for one interacting halo in Auriga 22. 27

3.1 Six face-on and edge-on RGB projections of Auriga 18 at various snapshots throughout the simulation. 31
3.2 A summary of the evolution of the bar and the disc throughout the Auriga 18 simulation. 34
3.3 The evolution of a selection of galaxy properties in Auriga 18 at lookback times of 10 – 7.5 Gyr. 35
3.4 The evolution of radial stellar and gas mass profiles in Auriga 18 at lookback times of 10 – 7.5 Gyr. 38
3.5 Face-on and edge-on stellar surface density profiles for each of Auriga 18 and my rerun at four different snapshots. 39
3.6 The magnitude of the A_2 Fourier mode in the stellar disc of my re-simulation, at lookback times from 8.5 – 5.5 Gyr. 40
3.7 Comparison between Auriga 18 and my rerun of a selection of galaxy properties from the rerun's beginning until $z = 0$. 42
3.8 The relation between merger times and bar formation times in the Auriga simulations which experience a GES-like merger. 48
3.9 Details of the evolution of angular momentum in the original and the rerun of Auriga 18 from 12 – 3 Gyr lookback time. 51

4.1 Bar length and corotation radius for each halo in my barred sample. . . 56
4.2 The relation between bar formation time and pattern speed/rotation rate. 58

4.3 The dependence at $z = 0$ of bar pattern speed and rotation rate on bar strength. . . . 60
4.4 The relation between rotation rate and the stellar mass-halo mass abundance matching relation at $z = 0$. . . . 61
4.5 The relation between baryon dominance and rotation rate. . . . 64
4.6 The fractional change in rotation rate from bar formation to $z = 0$ shown against the fractional change in baryon dominance over the same time period. . . . 65
4.7 The relation between rotation rate and the maximum Elmegreen parameter (S) for any interaction from 1 Gyr before to 0.5 Gyr after bar formation. . . . 67
4.8 The relation between rotation rate and the maximum Elmegreen parameter (S) for any interaction following 0.5 Gyr after bar formation. . . . 69

5.1 Auriga 24, as viewed for the Tremaine-Weinberg method. . . . 86
5.2 The gradient of $\langle V_{\rm LOS} \rangle$ to $\langle X \rangle$ for Auriga 24. . . . 87
5.3 Tremaine-Weinberg method estimates and direct pattern speeds at $z = 0$ for all Auriga bars. . . . 89
5.4 Illustration of the angles I use to describe a warped disc. . . . 90
5.5 The absolute relative error in the Tremaine-Weinberg method plotted against the angle of the warp from the disc plane at 2.5 kpc. . . . 91
5.6 The variation in relative error in the Tremaine-Weinberg method with warp axis at 5 kpc at $z = 0$. . . . 92
5.7 Average z position and V_z velocity of stars across the face-on projection of Auriga L8 near $z = 0$. . . . 94
5.8 Illustration of the angles used when describing the view for the Tremaine-Weinberg method. . . . 96

A.1 Scatter plots comparing, in pairs, the parameters shown in figures within Sec. 4.1 . . . 106

Chapter 1

Introduction

1.1 Galaxy morphology

Galaxies form the predominant bound stellar structures in the Universe, accreting gas to fuel the formation of stars in a gravitational potential well (Binney, 1977; White & Frenk, 1991; Cole et al., 1994). These are not static structures, but continuously evolving as stars are born and die, further material is accreted, and substructure emerges (Mo et al., 2010; Conselice, 2014). As such, studying galaxy evolution reveals information on the nature of gravity and dark matter (e.g. Rubin et al., 1978; Roshan et al., 2021), and the physical processes which dictate the movement of gas, the lives of stars, and even the life which emerges on planet(s) around them (e.g. Hawarden et al., 1986; Kennicutt, 1998; Gowanlock et al., 2011).

Observations of galaxies in the Universe reach out to redshift 14.44 (Naidu et al., 2026), providing us with snapshots of galaxy evolution from 13.6 Gyr ago all the way up to the present day (with our own Milky Way). These observed galaxies give us insights into how galaxies form, the shapes they can take, and how the galaxy population has transformed over time.

Early galaxy observations led to the Hubble sequence (Hubble, 1926), which categorises galaxies based on their visual morphology. Fig. 1.1 shows the Hubble sequence as in Hubble (1936) - note that the sequence does not indicate any genuine ordering of galaxy

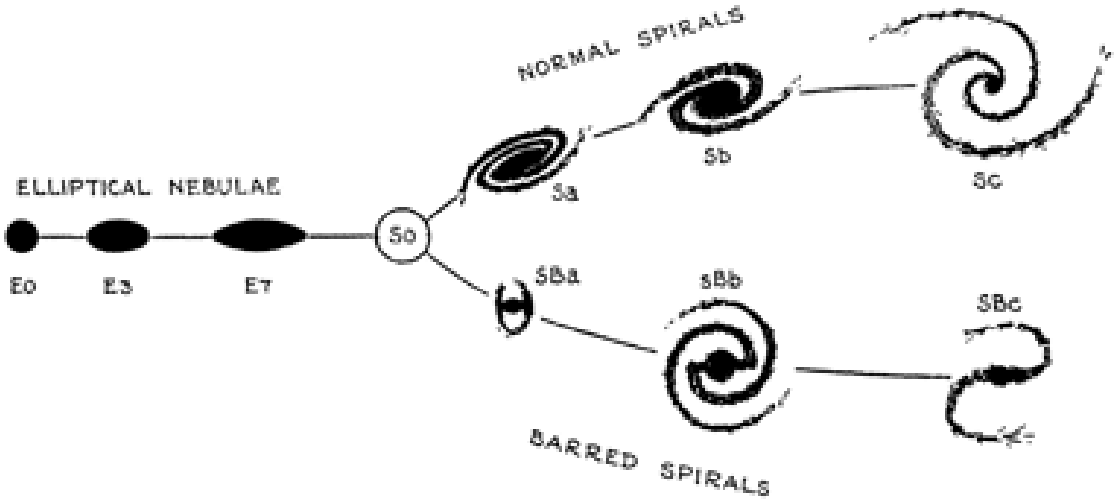


FIGURE 1.1: The Hubble sequence as illustrated in Hubble (1936). Early type galaxies are on the left, with late type galaxies on the right.

evolution. On the left of the sequence are the elliptical galaxies, also known as early type galaxies (early for their position on the sequence only). These are dispersion dominated systems of stars with generally low net rotation, and are further categorised by their shape from round E0 galaxies to more flattened E7 galaxies. At the central vertex of the sequence, are S0 lenticular galaxies. These are rotationally supported, so disc shaped, but kinematically hot and relatively featureless in terms of substructure.

On the right of the Hubble sequence are two branching paths, both representing a subset of spiral disc galaxies, also known as late type galaxies. Disc galaxies attain their thinned shape due to the angular momentum of accreted gas; as this gas falls into the galaxy, conservation of angular momentum leads to faster almost circular motion in a coherent direction (Hoyle, 1953; Mo et al., 1998). Stars then form out of this gas in rotationally supported orbits in a plane. Most isolated galaxies of similar mass to the Milky Way are disc galaxies (Lee et al., 2024). The position along each path of the late Hubble sequence is determined by the shape of the galaxy's spiral arms, but the distinguishing feature between the upper and lower paths is the presence of a bar – an elongated over-density of stars across the centre of the galaxy.

Bars are present in approximately 70% of disc galaxies at redshift zero ($z = 0$; Eskridge et al., 2000; Marinova & Jogee, 2007; Menéndez-Delmestre et al., 2007; Sheth et al., 2008; Buta et al., 2015; Erwin, 2018) and have been detected out to cosmic noon, with

their fraction decreasing to below 10% by $z \sim 4$ (Sheth et al., 2008; Le Conte et al., 2024; Huertas-Company et al., 2025; Géron et al., 2025; Amvrosiadis et al., 2025; Guo et al., 2025; Le Conte et al., 2026). These numbers imply that galactic bars have been present in a significant portion of disc galaxies for much of their evolution: indeed, observations have found some bars to be ancient structures as old as 13.5 Gyr (Gadotti et al., 2015; Bovy et al., 2019; Grady et al., 2020; de Sá-Freitas et al., 2025). The Milky Way itself has a strong bar (Peters, 1975; Weinberg, 1992; Weiner & Sellwood, 1999), and despite our obscured viewing angle from within the galaxy we can determine many of the bar's properties, including a length of 3 – 5 kpc dependent on the inclusion of possible spiral-linked structures at the bar's ends (Bissantz & Gerhard, 2002; López-Corredoira et al., 2007; Robin et al., 2012; Wegg et al., 2015). For a recent comprehensive review of dynamical measurements in the Milky Way, see Hunt & Vasiliev (2025).

Measurements of bar pattern speed are similarly split. Applying the continuity equation to the inner galaxy gives pattern speeds of $34 - 41\,\mathrm{km\,s^{-1}\,kpc^{-1}}$ (Bovy et al., 2019; Sanders et al., 2019; Zhang et al., 2024), largely agreeing with the $33 - 44\,\mathrm{km\,s^{-1}\,kpc^{-1}}$ from most methods which fit features of the galaxy to models (Weiner & Sellwood, 1999; Rodriguez-Fernandez & Combes, 2008; Sormani et al., 2015; Hunt et al., 2018; Kawata et al., 2021; Clarke & Gerhard, 2022; Trick, 2022; Dillamore et al., 2024; Khalil et al., 2025). However, fitting the Hercules stream to models gives conflicting results depending on the bar resonance it is associated with: $\sim 40\,\mathrm{km\,s^{-1}\,kpc^{-1}}$ for the corotation radius (Pérez-Villegas et al., 2017; Monari et al., 2019; Asano et al., 2020; Lucchini et al., 2024) and $\sim 55\,\mathrm{km\,s^{-1}\,kpc^{-1}}$ for the outer Lindblad resonance (e.g. Antoja et al., 2014; Ramos et al., 2018). See Sec. 5.1 for a discussion of methods of bar pattern speed measurement.

1.2 Bar formation

Bars naturally form out of stellar discs due to self-gravity. In a disc which is unstable to structure formation (see below), a non-axisymmetric perturbation can be reinforced by capturing stars from the disc into elliptical orbits. The angular momentum from these

captured orbits is transferred outwards through resonances with more distant material. As the resulting over-density grows, it captures further stars, previously on more circular orbits, which are in resonance with the emerging bar. By this mechanism, the bar forms into a robust structure, a few kpc across (Binney & Tremaine, 1988).

A number of factors affect the likelihood of a disc to form a bar. Early studies found that a pure flat disc almost always forms a bar (Dzyuba & Yakubov, 1970; Hohl, 1971), leading to the question of why do not all disc galaxies have bars? Ostriker & Peebles (1973), Fall & Efstathiou (1980) and Efstathiou et al. (1982) suggest that in order to stabilise a disc against bar formation, there must be a very massive spherical halo component within the disc radius. Toomre (1964) instead place limits on the vertical velocity dispersion within the disc, finding that a disc with high vertical velocity dispersion is less susceptible to forming massive concentrations of matter within it (such as those which might provide a perturbation for bar formation). Athanassoula & Sellwood (1986) confirm this tendency for bars specifically and find that significant vertical velocity dispersion can relax the constraints of a massive halo component. However, precise constraints on conditions for bar formation such as those presented in these studies are rarely reliable (Athanassoula, 2008; Sellwood, 2016; Romeo et al., 2023). The probability of bar formation is also reduced by a large gas fraction (Shlosman & Noguchi, 1993; Athanassoula et al., 2013; Seo et al., 2019), by a large central bulge (Hohl, 1976; Combes & Elmegreen, 1993; Sellwood & Evans, 2001; Kataria & Das, 2018), and by specific properties of the shape and angular momentum of the dark matter halo (Saha & Naab, 2013; Yurin & Springel, 2015; Collier et al., 2018).

In the Milky Way, the time of bar formation is highly debated, due to bars' present properties not having a strong dependence on formation time. Bovy et al. (2019) examine the formation history of the Milky Way's stars across the bar and disc, and find that the bar's population is significantly older than the disc's, from which they conclude that the bar formed around 8 Gyr ago. Oxygen-rich stars in particular trace the shape of the bar for populations as old as 9 Gyr, leading Grady et al. (2020) to conclude that this is when the bar formed. In contrast, Cole & Weinberg (2002) find a population of intermediate age, carbon-rich stars tracing the bar and suggest a much younger age of

3 Gyr. This age is supported by Nepal et al. (2024), whose study focuses on the ages of the metal-rich stars in the Solar neighbourhood.

Looking at other related structures also places limits on the bar's age. It is thought that the nuclear stellar disc formed shortly after the bar (Baba & Kawata (2020) discuss the usefulness and restrictions of this method for dating the bar), and Nogueras-Lara et al. (2020) find that this is dominated by young stars, suggesting that either the bar has been inefficient at inward gas transport for most of its history or else it is just 1 Gyr old. Favouring the first case, Sanders et al. (2024) uses variable stars from the same region to find a minimum age of 8 Gyr, and Schödel et al. (2023) suggest that the nuclear disc is even older. These ages are consistent with the minimum age of the inner ring, found by Wylie et al. (2022) to be 7 Gyr. Despite no agreement, evidence is mounting for an older bar, and it is this earlier formation scenario that I examine the mechanisms of in Chapter 3.

1.3 Bar angular momentum

Bars mediate the exchange of angular momentum and energy of galactic material and, given their prevalence and longevity in disc galaxies, they are significant drivers of secular evolution. This angular momentum exchange is most efficient at resonances – set by the pattern speed of the bar, Ω_p – where the orbits of stars and other matter can be significantly altered by becoming trapped in or pushed away from the resonance (e.g. Contopoulos & Mertzanides, 1977; Dehnen, 2000). In the disc, these resonances have been seen to have strong effects on the presence and properties of spiral arms (Sanders & Huntley, 1976; Schwarz, 1984; Bissantz et al., 2003), the migration and mixing of stellar populations across the disc (Dehnen, 2000; Minchev & Famaey, 2010; Brunetti et al., 2011), and the driving of gas towards the centre of the galaxy, which can in turn form structures such as nuclear discs and rings (Matsuda & Nelson, 1977; Simkin et al., 1980; Sakamoto et al., 1999; Sheth et al., 2005; Cole et al., 2014). Meanwhile, the stellar and dark matter halos absorb angular momentum from the bar, which can also spin these components up and change the overall mass profile of the halo (Sellwood, 1980; Tagger

et al., 1987; Hernquist & Weinberg, 1992; Weinberg & Katz, 2002; Athanassoula, 2003; Athanassoula et al., 2013). Therefore, in order to understand the evolution of disc galaxies, it is essential to understand the evolution of their bars and their pattern speeds in particular.

Angular momentum exchange with the rest of the galaxy has an effect on the bar pattern speed in turn. Studies tend to find that, as they evolve, bars lengthen and slow while trapping more stars on elongated bar-supporting orbits and transferring their angular momentum outwards (Tremaine & Weinberg, 1984a; Martinez-Valpuesta et al., 2006; Elmegreen et al., 2007). Bars can also slow down (without significantly lengthening) due to dynamical friction imparted by the dark matter halo (Tremaine & Weinberg, 1984a; Weinberg, 1985; Little & Carlberg, 1991; Debattista & Sellwood, 2000; Athanassoula, 2003; O'Neill & Dubinski, 2003; Sellwood & Debattista, 2006; Kataria & Das, 2019). To explore the effect of dynamical friction on the slow-down of bars, we can use the ratio of their corotation radius (the radius at which circular orbits within the disc have angular velocity matching the rotation of the bar) to their semi-major axis length (e.g. Debattista & Sellwood, 1998, 2000). This ratio is sometimes referred to as the 'rotation rate' (e.g. Cuomo et al., 2019; Buttitta et al., 2023) and denoted by $\mathscr{R}$. $\mathscr{R}$ increases when the growth of the corotation radius – due to the decrease of the pattern speed – outpaces the lengthening of the bar. Bars with $\mathscr{R} > 1.4$ are considered slow and bars with $1 < \mathscr{R} < 1.4$ are considered fast (Debattista & Sellwood, 2000). Bars with $\mathscr{R} < 1$ are called ultra-fast, since consideration of the main bar-supporting orbits theoretically places the ends of any bar within the corotation radius (Contopoulos, 1980). In practice, observations of ultra-fast bars are not unusual (Buta & Zhang, 2009; Aguerri et al., 2015; Guo et al., 2019) but may be a result of errors, such as artificial lengthening of the bar caused by alignment of spiral arms (Hilmi et al., 2020; Cuomo et al., 2021).

There are a number of factors that can affect the slow-down (or lack thereof) of the bar, leading to departures from the picture of inevitable slow-down in both Ω_p and $\mathscr{R}$. For example, bars in highly baryon-dominated discs will tend to experience less of an impact from dynamical friction (Debattista & Sellwood, 1998, 2000; Athanassoula, 2003). Additionally, Li et al. (2023) show that if the dark matter halo has a high spin, then slow-down from dynamical friction can be halted for an extended period of up to

5 Gyr, due to the wake of the bar in the dark matter following the stellar bar very closely and so imparting very little torque. Athanassoula (2003), Klypin et al. (2009) and Zheng & Shen (2025) also find that a higher vertical velocity dispersion in the disc can reduce the efficiency of angular momentum exchange and delay bar slow-down.

Berentzen et al. (2007), Romano-Díaz et al. (2008), Villa-Vargas et al. (2010), Athanassoula (2014) and Beane et al. (2023) find that bars in galaxies containing higher fractions of gas slow down less compared to those with lower gas fractions: the former either maintain a constant pattern speed or speed up. The speed-up occurs as the gas is directed towards the centre of the galaxy by the bar, but the exact mechanism by which the bar slow-down is delayed/halted is unclear. Bournaud et al. (2005) and Beane et al. (2023) claim that the inflowing gas produces a positive torque on the bar directly, whereas Berentzen et al. (2007) and Romano-Díaz et al. (2008) find that it is instead the build up of mass in the centre of the galaxy due to the inflow which both weakens the bar and speeds it up.

1.4 The impact of galaxy interactions on galaxy structure

Another source of angular momentum for existing bars is interactions and mergers with external galaxies. Interactions can affect bars in a variety of ways: interactions can slow down bars (as in Sundin et al., 1993; Athanassoula, 1996; Jiménez-Arranz & Roca-Fàbrega, 2025), speed-up bars (see Gerin et al., 1990; Lokas et al., 2014; Semczuk et al., 2024), or even destroy them in extreme cases (Kannan et al., 2015; Cavanagh et al., 2022; Bi et al., 2022) – although this last scenario is rare (Zana et al., 2018). While the effects of individual interactions are determined in the above papers, there is no comprehensive understanding of the net effects of multiple galaxy interactions and mergers on a population of galactic bars in a cosmological setting.

Galaxy interactions and mergers can also trigger bar formation in unbarred discs through induced perturbations in the host galaxy (e.g. Noguchi, 1987; Gerin et al., 1990; Lang

et al., 2014; Lokas et al., 2014; Moetazedian et al., 2017). Miwa & Noguchi (1998), Martinez-Valpuesta et al. (2017), Gajda et al. (2017) and Bi et al. (2022) find that tidally triggered bars tend to be slower than their secularly formed counterparts in simulations. However, Zheng & Shen (2025) argue that this trend is due to the internal properties of galaxy simulations which have been set up to require an interaction in order to form their bar: initial conditions for idealised simulations of tidally-induced bars are often tuned such that a bar does not form in isolation. Tuning in this way means that properties like the velocity dispersion of discs are higher than their secular bar-forming counterparts. Zheng & Shen (2025) conclude that this bias in disc initial conditions (mainly the vertical velocity dispersion in the disc, although the circular velocity in the inner disc differs slightly between models) results in slower bars in tidal interaction simulations. However, Pettitt & Wadsley (2018) find no consistent difference in pattern speed between tidally induced bars and bars formed in isolation, and Peschken & Lokas (2019) even find that tidally induced bars tend to be slightly faster than their secularly formed counterparts (in terms of rotation rate $\mathscr{R}$) in the Illustris cosmological simulation (Vogelsberger et al., 2014).

In the Milky Way, a significant accretion event occurred $\sim$ 8-11 Gyr ago (this range of times is consistent with the results of Belokurov et al. (2018), Helmi et al. (2018), Di Matteo et al. (2019), Gallart et al. (2019), Chaplin et al. (2020) and Naidu et al. (2021)), known as Gaia-Encaladus/Sausage (GES). This time is within $\sim$ 2 Gyr of the older estimates of bar formation time in Sec. 1.2. Such an accretion event had been hinted at for some time (Brook et al., 2003, 2007), but was confirmed by Belokurov et al. (2018) and Helmi et al. (2018) using data from Gaia (Gaia Collaboration et al., 2016). GES is thought to have had a stellar mass of $10^{8-9.5}$ $M_\odot$, around 5-10% of the Milky Way's at this time (e.g. Helmi et al., 2018; Deason et al., 2019; Feuillet et al., 2020; Lane et al., 2023). The Milky Way is expected to have had a quiescent merger history after this merger event up to the present day (Ruchti et al., 2015; Fragkoudi et al., 2020), making GES one of the most significant events in our galaxy's history. While uncertainties in the time of this merger and the time of bar formation are much larger than the expected dynamical times involved, the estimated times of both significantly overlap. Because of this overlap and the potential impact mergers can have on bar formation, there may be

some link between the two events. Moreover, the lack of significant mergers after this event suggests that any structures formed at this epoch would evolve by secular processes rather than being disrupted by external interactions.

1.5 The use of simulations

There are three profound limitations to what we can infer from galaxy observations:

- The oldest epochs of galaxy evolution are restricted to observations at low resolution. While the James Webb Space Telescope has recently pushed this boundary further than ever before, the earliest stages of galaxy formation and structure evolution remain unresolved. This leaves gaps in our understanding of this crucial early stage of galaxy formation.

- The angle at which we observe galaxies, limited by our place in the Universe, means we must deal with projections of galaxies rather than the full six dimensional position and velocity information. In distant galaxies, only the position on the plane of the sky is available, with velocities in the line of sight obtainable where spectroscopy can be used, giving three dimensions. Within the Local Group, some proper motions in the plane of the sky can also be measured, and in the Milky Way, Gaia has released the full kinematic information for 33,812,183 sources in its data release 3 (Gaia Collaboration et al., 2023). However, most galaxies can still only be observed in two or three phase space dimensions, leading to degeneracies in inferring their properties - for example an E0 elliptical galaxy is difficult to distinguish from a S0 lenticular galaxy viewed face-on.

- Each galaxy we observe can only be recorded at the time we see it, giving us decades of its evolution rather than the thousands of millennia over which changes to galaxies typically take place. While this is mitigated by taking the observed galaxies as a population over time, we are still left to fill in the gaps of how an individual galaxy evolves over billions of years.

A valuable tool to help supplement observations and fill in these limitations is numerical simulation. These take a model of how gravity and other processes are thought to function in the Universe, and numerically evolve a set of initial conditions to predict the changes which would occur. The first such simulation was carried out using lightbulbs in Holmberg (1941) to model the collision of a pair of galaxies, but since the advent of computers the capabilities of these simulations has exploded. They now range from detailed simulations of individual galaxies reaching up to single star resolution (Hirashima et al., 2025) (in addition to much smaller scale simulations from other fields of science) to cosmological simulations of 2400 Mpc cubes of cosmology (Euclid Collaboration et al., 2025).

Many results around bars have been found due to simulations, including those in the above sections. Early simulations of self-gravitating disc galaxies already showed bar formation (e.g. Dzyuba & Yakubov, 1970; Miller et al., 1970; Hohl, 1971; Ostriker & Peebles, 1973). Sellwood (1980), Weinberg (1985), and later Athanassoula (2002) uncovered the importance of the response of the (dark matter) halo in bar evolution by the introduction of a live halo component to simulations. While debated for a time (e.g. Hasan & Norman, 1990; Bournaud & Combes, 2002), bars were confirmed to be long-lived structures due to results from simulations in Sparke & Sellwood (1987), Marinova & Jogee (2007), Kraljic et al. (2012) and Athanassoula et al. (2013). At present, our understanding of bar evolution is driven by simulations, with the contents of Sec. 1.3 and Sec. 1.4 above being primarily discovered through simulation.

1.5.1 Limitations

Simulations encounter resolution limitations, since it is currently impossible to simulate at once the $\sim$ 15 orders of magnitude separating the masses of individual stars and galaxy clusters, a problem only accentuated when considering the need for a statistically representative population of galaxies or models for the behaviour of gas. Simulations are also inherently based on models of how the Universe behaves. As such, any conclusions drawn from simulations must be accompanied by the caveat that it is based on the assumptions of gravity, cosmological parameters and baryon physics which produce

it. These choices are physically motivated to represent our current understanding of cosmology (e.g. Crain et al., 2015) and one of the aims of cosmological simulations is to test this understanding (see for example discussions in Vogelsberger et al., 2014; Schaye et al., 2015; Marinacci et al., 2018).

Bars have proven especially difficult to match to observation in cosmological simulations. Observations in Rautiainen et al. (2008), Corsini (2011), Aguerri et al. (2015) and Guo et al. (2019) point towards most bars in the nearby Universe being fast, or close to fast. While more recent data suggest that there may instead be an approximately equal number of slow and fast bars (Garma-Oehmichen et al., 2022; Géron et al., 2023), these bars are not extremely slow, with bars slower than $\mathscr{R} = 2.5$ being relatively uncommon. In contrast, cosmological simulations show either a lack of bars, as Reddish et al. (2022) shows in the NewHorizon simulation (Dubois et al., 2021), or a prevalence of slow bars. Algorry et al. (2017), Peschken & Lokas (2019), Roshan et al. (2021) and Habibi et al. (2024) show that the bars in the EAGLE (Crain et al., 2015; Schaye et al., 2015), Illustris (Vogelsberger et al., 2014) and IllustrisTNG – both TNG100 (Marinacci et al., 2018; Naiman et al., 2018; Nelson et al., 2018; Pillepich et al., 2018; Springel et al., 2018) and TNG50 (Nelson et al., 2019; Pillepich et al., 2019) – simulations have rotation rates much slower than those from observations (most have $\mathscr{R} > 2.5$), and Ansar et al. (2025) find no fast bars (i.e. with $\mathscr{R} < 1.4$) in the FIRE-2 simulations (Hopkins et al., 2018; Wetzel et al., 2023) despite lower average rotation rates. Frankel et al. (2022) attribute the lack of fast bars in the IllustrisTNG simulations to the bar lengths being too short on average in comparison to observations, which is exacerbated for low numerical resolution. However, Fragkoudi et al. (2021) show that the Auriga cosmological zoom-in simulations do produce fast bars, in keeping with observations. They argue that these faster bars are because Auriga galaxies have a higher stellar mass to dark matter mass ratio compared to other cosmological simulations, which minimises the slow-down impact from dynamical friction. This is the simulation suite which I use in this thesis, and I describe it in detail in Sec. 2.1 below.

1.6 Thesis overview

In Chapter 1, I introduced bars, their role in galaxy evolution, the primary mechanisms which govern their formation and evolution, and how simulations can be used to discover their properties.

In Chapter 2, I outline the Auriga simulations which I use for this thesis' research (both original and rerun). I then explain my methods for extracting bar parameters, galaxy properties, and parametrisations of galaxy interaction histories from these simulations.

In Chapter 3, I present the results of my investigation into the formation of the Milky Way bar using an example simulation from the Auriga suite. I also describe a re-simulation that I perform to further confirm the formation mechanism, and explain how the wider Auriga suite fits into this picture.

In Chapter 4, I present the results of my research into bar rotation rates in the Auriga simulations. I show correlations including with bar age, bar strength, baryon dominance, stellar mass and accretion history to evaluate the primary influences on bar rotation.

In Chapter 5, I present the results of my tests applying the Tremaine-Weinberg method to the Auriga simulations. I evaluate the method in this context both in general and in the presence of distortions to the galactic discs.

Lastly, in Chapter 6, I summarise this thesis and reiterate the main conclusions that I have drawn from the research presented.

Chapter 2

Methodology

2.1 The Auriga simulations

2.1.1 The `Original/4` and `LowMassMws/4` suites

Throughout this thesis, I use the Auriga suite of simulations (Grand et al., 2017, 2019), a set of 39 magneto-hydrodynamical cosmological zoom-in simulations of Milky Way-mass halos. The initial conditions for the simulations were generated by first identifying halos with $0.5 < M_{200}/10^{12}\,\mathrm{M}_\odot < 2$ from the $z = 0$ snapshot of the dark matter-only run of the Lambda cold dark matter (ΛCDM) EAGLE cosmological simulations (Crain et al., 2015; Schaye et al., 2015). The most isolated quartile of these halos was randomly sampled (see Grand et al., 2017, for details). Once identified, the resolution of the dark matter particles of the Lagrangian region of each halo at $z = 127$ was refined to higher resolution, whereas the particle resolution outside of this region was progressively worsened to increase computational efficiency while retaining the large-scale gravitational tidal field from the Cosmic Web. Dark matter particles were then split into dark matter-baryon pairs according to cosmological parameters taken from Planck Collaboration et al. (2014): $h = 0.677$, $\Omega_\mathrm{b} = 0.048$, $\Omega_\mathrm{m} = 0.307$, and $\Omega_\Lambda = 0.693$. Typical mass resolutions in the highest resolution region are $5 \times 10^4\,\mathrm{M}_\odot$ for baryons and $3 \times 10^5\,\mathrm{M}_\odot$ for dark matter. The dark matter and stars were given a softening length of

$500h^{-1}$ cpc up to being fixed at 369 pc from $z = 1$ onward. The softening length of a gas cell varies from these values as a minimum up to a maximum of 1.85 kpc, scaling with the size of the gas cell.

The simulations were run with the moving-mesh magneto-hydrodynamic code AREPO (Springel, 2010; Pakmor et al., 2016), which includes a TreePM gravity solver and the AURIGA sub-grid galaxy formation physics model. The subgrid physics include:

- Reionisation modelled as uniform UV background radiation until $z = 6$ (as in Faucher-Giguère et al., 2009).
- Primordial and metal line cooling.
- A model of the interstellar medium with two phases: a hot phase and a phase of embedded cold dense clouds (Springel & Hernquist, 2003).
- Star particles, each representing a simple stellar population, which form stochastically out of the gas if it is denser than 0.1 atoms cm^{-3}. If a gas cell is fully converted to star particle(s), then it is removed, otherwise the cell retains a reduced mass.
- A stellar evolution model which tracks the age, metallicity, and colour band luminosities of star particles from a Chabrier (2003) initial mass function. The evolution includes type Ia and type II supernovae and AGB stars, whose mass and metals are distributed to nearby gas cells using yields from Portinari et al. (1998), Thielemann et al. (2003), Travaglio et al. (2004) and Karakas (2010).
- Feedback from type II supernovae, modelled as the formation of a wind particle instead of a gas particle (Vogelsberger et al., 2013). This particle travels in a random direction, with velocity dependent on the local dark matter motion (motivated by Okamoto et al., 2010), until it deposits its mass, metals, momentum and energy (split between kinematic and thermal) in a non-star-forming gas cell.
- Black hole seeding at the point of densest gas in $5 \times 10^{10}\,M_{\odot}h^{-1}$ mass halo groups, with subsequent accretion and merger following Springel et al. (2005). Active galactic nucleus (AGN) feedback is then implemented in a quasar mode,

with even thermal heating of neighbouring gas cells, and a radio mode, with heated gas bubbles placed nearby.

- A model of magnetic fields, initially seeded as an even 10^{-14} G across the simulation (Pakmor et al., 2014, 2017).

For full details of the AURIGA code, see Vogelsberger et al. (2013), Marinacci et al. (2014) and Grand et al. (2017). For further information on the details of the Auriga simulations as a whole, see Grand et al. (2017) and references therein.

2.1.2 High temporal resolution reruns

While the original Auriga suite of 39 simulations serves as the basis for the work of this thesis, I use rerun versions of these with higher temporal resolutions. The initial conditions of these simulations are the same as those of the `Original`/4 and `LowMassMws`/4 suites described in Grand et al. (2024)[1]. However, my analysis requires a much finer snapshot cadence than these simulations provide, in order to accurately order bar formation and mergers (in Chapter 3) and to directly measure the patterns speeds of bars (in Chapters 4 and 5).

A rerun of Auriga 18 already exists with 3000 snapshots (i.e. outputs every ~ 5 Myr) at the same resolution. For the remaining 38 simulations, I re-simulated each halo that produces a barred galaxy at $z = 0$ (according to Fragkoudi et al., 2025) with additional 5 Myr-cadence snapshots of the stellar particles only. These higher cadence outputs, which I refer to as "snipshots", allow the computation of pattern speed directly from the change in the phase angle of the bar without using any assumptions such as those required for the commonly used Tremaine-Weinberg method (Tremaine & Weinberg, 1984b). In addition, the re-simulation approximately doubles the number of full snapshots (which contain dark matter particles, gas cells, black holes, and tracer particles as well as star particles) such that their cadence becomes ~ 60 Myr at late times. These snapshots are

[1]These initial conditions and simulations are publicly available and accessible via https://wwwmpa.mpa-garching.mpg.de/auriga/data.html.

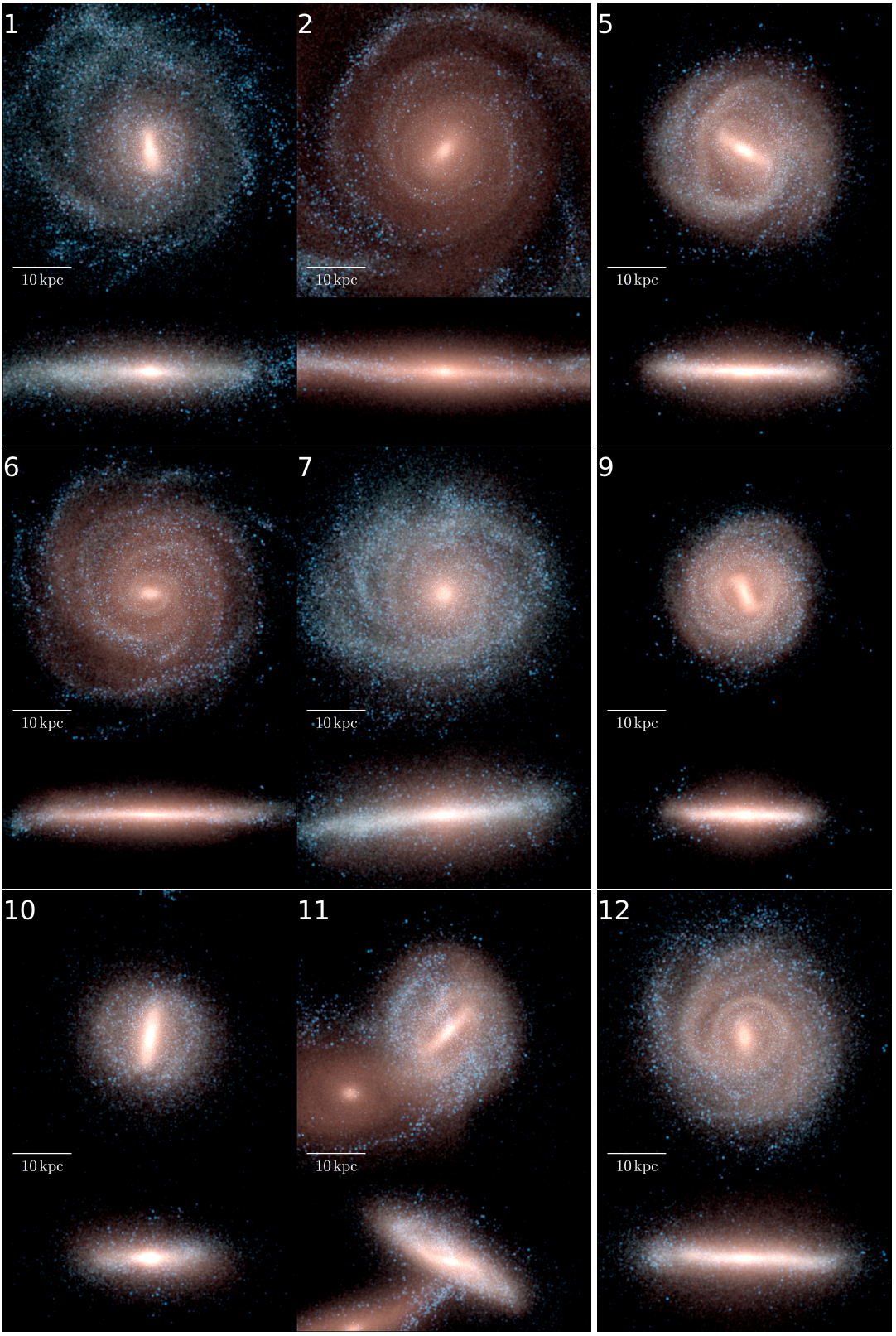


FIGURE 2.1: RGB coloured images of high temporal resolution reruns from Auriga - 1 through 12. Each takes the star particles' K-, B- , and U- band luminosities and shows them here in red, green, and blue respectively. This gives the older star particles in red and the younger star particles in blue.

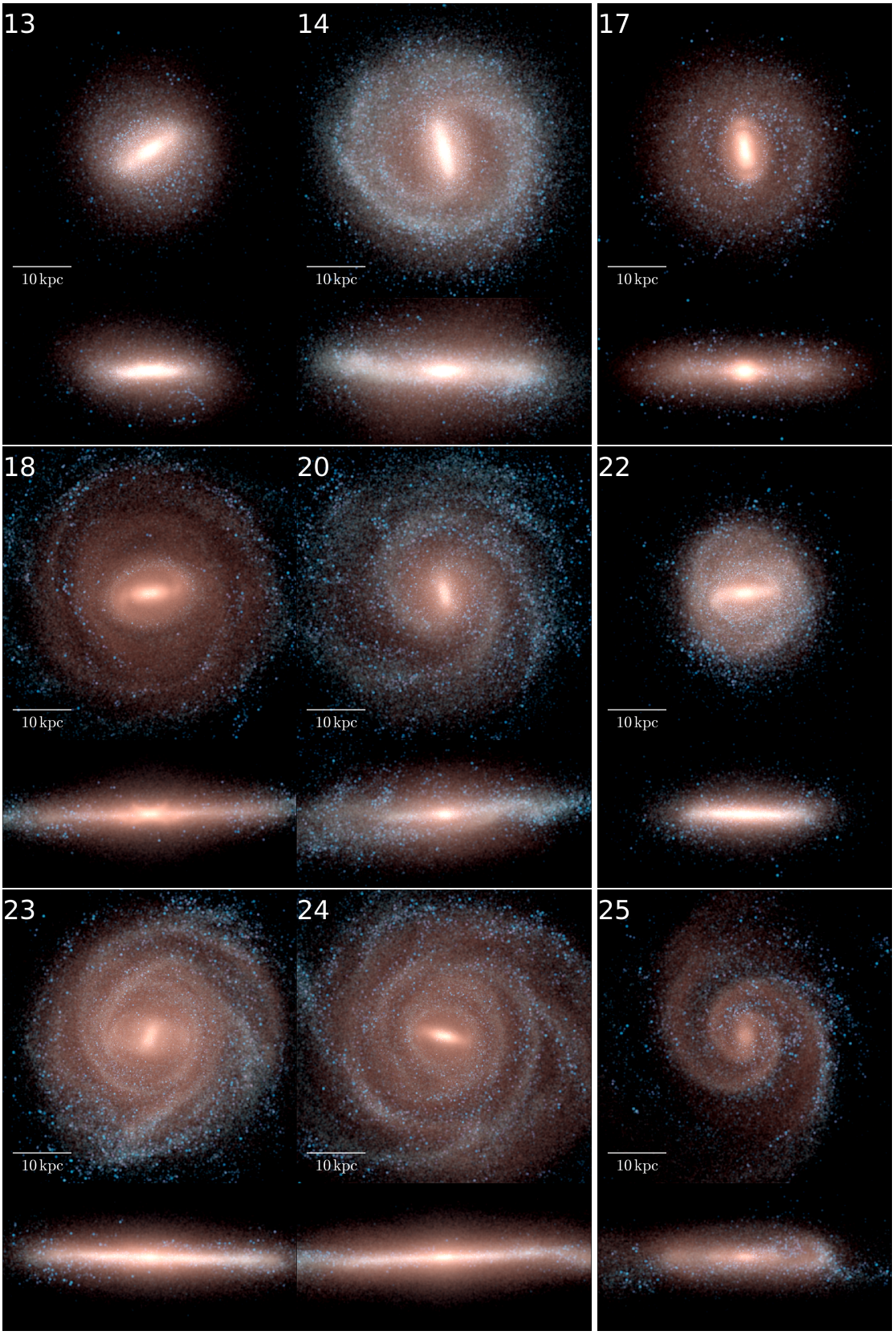


FIGURE 2.2: RGB coloured images of high temporal resolution reruns from Auriga - 13 through 25, constructed as in Fig. 2.1.

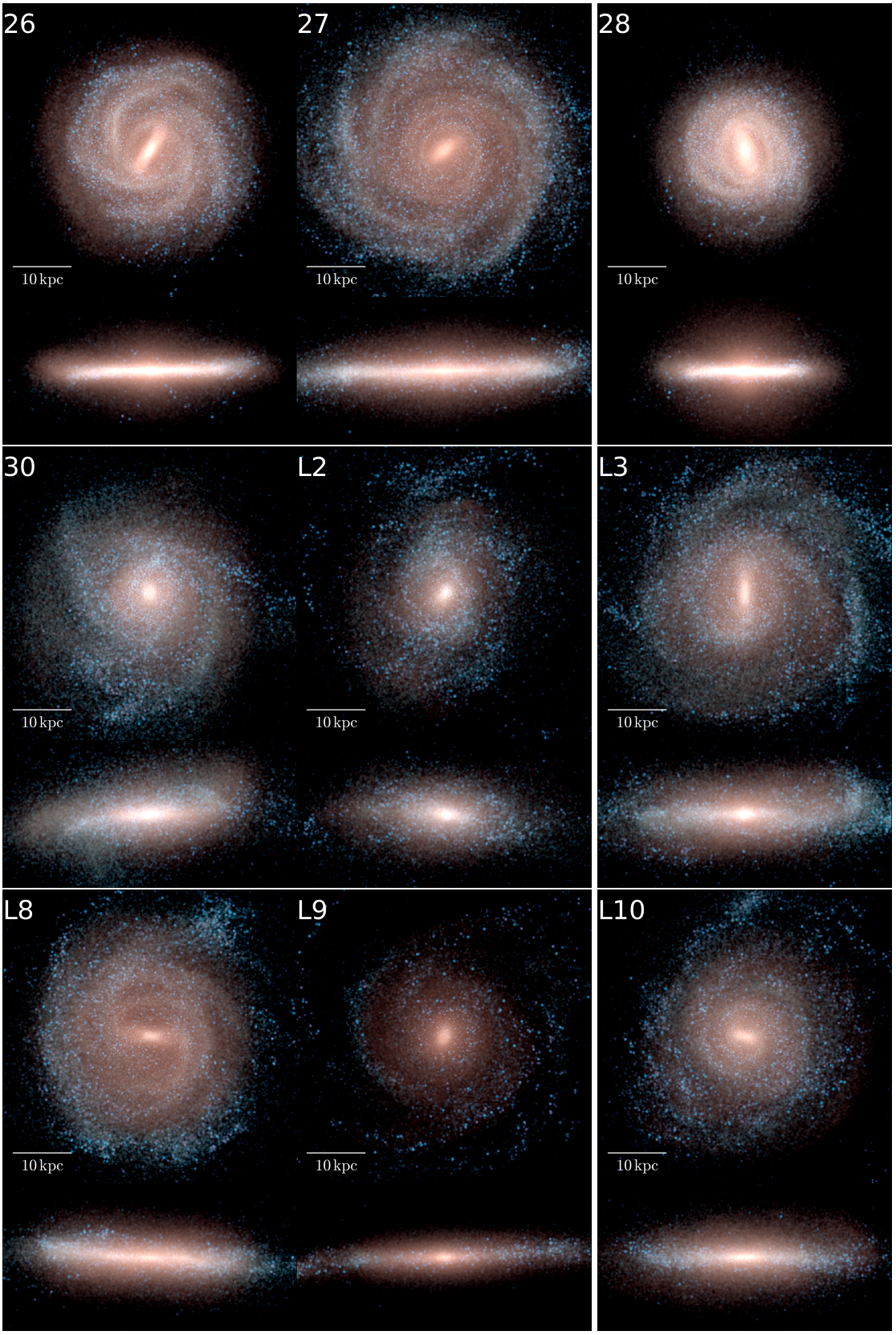


FIGURE 2.3: RGB coloured images of high temporal resolution reruns from Auriga - 26 through low-mass-run 10, constructed as in Fig. 2.1.

accompanied by a merger tree, which tracks the paths and merger histories of each dark matter halo in the simulation.

The final snapshots resulting from these 27 re-simulations, including Auriga 18, are shown in Fig. 2.1, Fig. 2.2, and Fig. 2.3 as face on and edge on images of their stars. The star particles are coloured by their K-, B- , and U- band luminosities to give the appearance of a visible light observation.

2.2 Galaxy and interaction properties

2.2.1 Disc and bar parameters

2.2.1.1 Disc and bar angle

Before analysing each snipshot, I first centre and rotate the galaxy. Beginning with the interpolated coordinates from the merger tree at the snapshot times, I centre the galaxy by taking the centre of mass of the stars within a sphere of radius 30 kpc, repeating for spheres of radius 10 kpc and 4 kpc to converge on the true centre. I then align the median angular momentum vector of the stars within the effective (half-mass) radius of the galaxy with the z-axis, such that the region containing most of the mass, and therefore most of the bar, lies within the x-y plane.

I also find the angle between the bar and the x-axis for each snipshot, using the angle of the second Fourier mode A_2 of the stellar mass profile in the inner 4 kpc, excluding the inner 0.5 kpc and restricting to within 1 kpc of the disc plane. This angle is calculated as

$$\Theta_2 = \frac{1}{2} \arctan \frac{\sum_k m_k \sin 2\theta_k}{\sum_k m_k \cos 2\theta_k} \tag{2.1}$$

with an associated magnitude for the mode given by

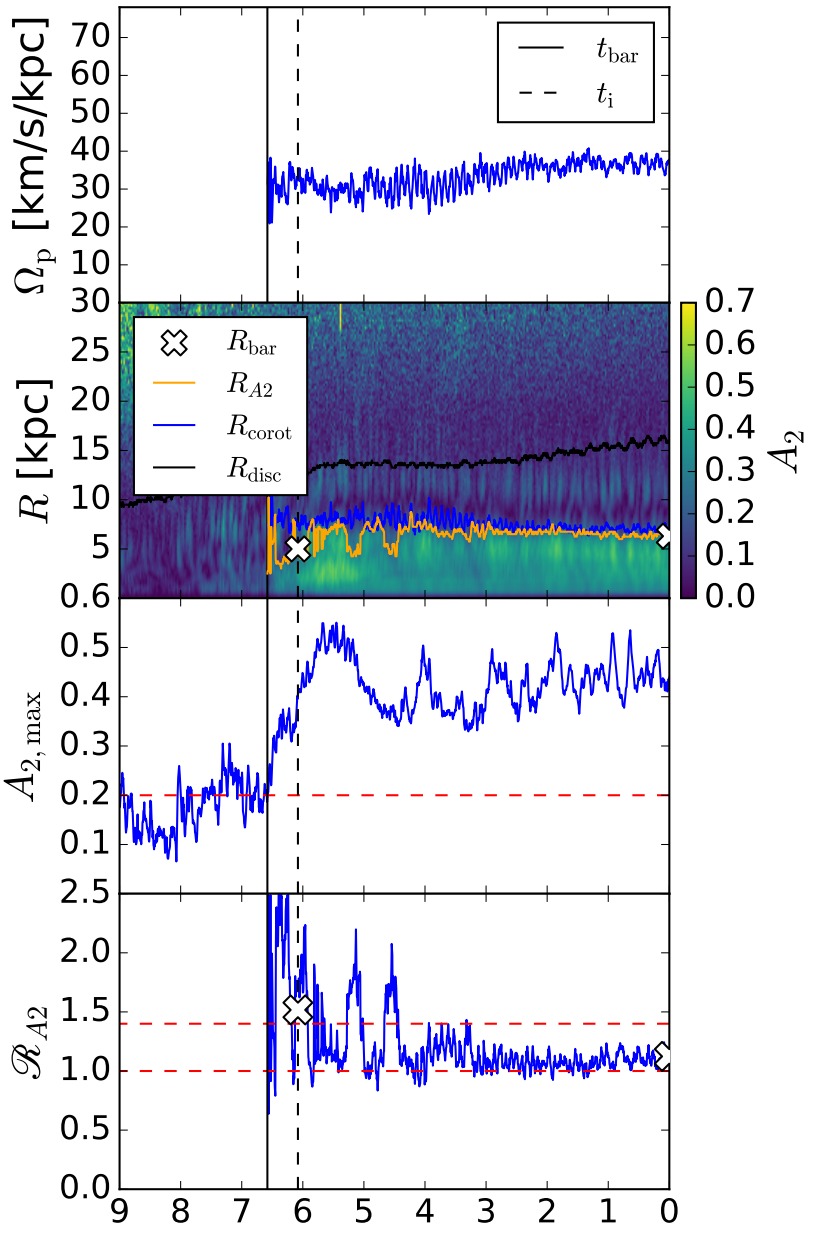


FIGURE 2.4: Summary of the main bar parameters used for halo 22 of the Auriga simulations plotted against lookback time. The top panel shows the pattern speed of the bar, from the bar formation time onwards. The second panel shows the bar length calculated from the A_2 Fourier mode (light orange) and the corotation radius (blue) from the bar formation time onwards, alongside the disc extent (black). The colour scale shows the radial profile of the A_2 Fourier mode with lighter, yellower colours indicating higher values. The white crosses give the values of bar length from ellipse fitting. The third panel shows the maximum of the A_2 Fourier mode at each time, which I also define as bar strength; the red dashed line indicates $A_{2,\rm max} = 0.2$, my cut-off for bar formation. The bottom panel shows the rotation rate as calculated from the bar length with A_2 and corotation rate (blue line), with the red dashed lines indicating rotation rates of 1 and 1.4. The white crosses give the values of rotation rate using bar lengths from ellipse fitting, as used Chapter 4. In all panels, the vertical solid black line shows the time of bar formation $t_{\rm bar}$, and the vertical black dashed line shows 0.5 Gyr later.

$$A_2 = \sqrt{\left(\sum_k m_k \cos 2\theta_k\right)^2 + \left(\sum_k m_k \sin 2\theta_k\right)^2} \tag{2.2}$$

where m_k and θ_k are the mass and angle from the positive x-axis respectively for each particle in the chosen volume. The magnitude is normalised to the A_0 Fourier mode, the total mass in the same volume. The pattern speed, Ω_p, is then the rate of change of the bar angle between adjacent snipshots. I show an example of the pattern speed evolution as calculated by this method for Auriga 22 in the top panel of Fig. 2.4, converted from rad Gyr^{-1} to km s^{-1} kpc^{-1} to match the typical units used in observations. One can see that in this case, the pattern speed is nearly constant, except for a small increase from 4 – 2 Gyr lookback time.

2.2.1.2 Bar formation time

To find the time of bar formation, I first use the maximum of the A_2 mode magnitude to measure bar strength. I calculate A_2 of stars in 250 pc-wide radial annuli within 1 kpc of the disc plane. The 2D histogram in the second panel of Fig. 2.4 shows the dependence of the normalised A_2 Fourier mode on both galaxy radius and time. Consistent higher values in the inner regions indicate the presence of a bar and this feature can be seen in the lower portion of the panel from $\sim$ 6 Gyr lookback time onwards. I therefore use, for any given time, the maximum value for any bin in the inner 6 kpc as a measure of bar strength, $A_{2,\mathrm{max}}$. I show bar strength in the third panel of Fig. 2.4, with the red dashed line indicating $A_{2,\mathrm{max}} = 0.2$. In Auriga 22, as is common for many of the halos, the bar strength exhibits some variation at early times due to transient features, before quickly increasing past 0.2 and remaining above this line for the remainder of the simulation. I set the bar formation time as the time of the snipshot for which $A_{2,\mathrm{max}}$ last surpasses this value of 0.2[2]. The vertical solid line shown across all panels of Fig. 2.4 indicates the bar formation time calculated in this way, t_{bar}. If a halo has $A_{2,\mathrm{max}} < 0.2$ at $z = 0$, I say that the halo is unbarred.

[2]I note that this is a different value of $A_{2,\mathrm{max}}$ to the 0.25 used in Fragkoudi et al. (2025) for the same suite of simulations. I make this change due to some of the halos in the rerun suite now with $0.2 < A_{2,\mathrm{max}} < 0.25$ but visible bars in face-on projection images.

Although, following the definition above, the bar formation time is known to within half a snipshot (corresponding to 2.5 Myr), the definition itself is somewhat arbitrary due to the selection of $A_{2,\mathrm{max}}$ cut-off. Therefore, I examine the sensitivity of the bar formation time by varying the limit from $A_{2,\mathrm{max}}$ by 10% to see how the change affects the resultant bar formation time. I find that the bar formation time is changed by less than 2.5% for the oldest 10 bars, with only five others (Auriga 12, Auriga 20, Auriga 28, Auriga L2, and Auriga L10) changing by more than 0.5 Gyr. Each of these five bars is younger than 3 Gyr and have bar strengths at $z = 0$ weaker than 0.31. It is reasonable to conclude that this definition of bar formation time is stable for older, stronger bars, but is sensitive to the choice of limits for weak and young bars.

Note that I make three exceptions to this definition of bar formation time: Auriga 17 which forms its bar extremely early in its evolution, Auriga 23 which periodically produces snipshots with $A_{2,\mathrm{max}} < 0.2$ due to a double barred system, and Auriga L2 which has a bar that is destroyed by $z = 0$. In the latter two cases, I choose a time when the bar is clearly present in the face-on stellar distribution, but before any subsequent dips in $A_{2,\mathrm{max}}$ below 0.2, and only use the snipshots before this time to calculate the bar formation time. For Auriga 17, I delay the bar formation time until a bar has become visually present in the face-on stellar distribution, since prominent, consistent spirals which reach to the inner 6 kpc lead to a consistently high 'bar strength' before a genuine bar has formed.

2.2.1.3 Rotation rate

In Chapter 4, I primarily use the rotation rate $\mathscr{R} = \frac{R_{\mathrm{corot}}}{R_{\mathrm{bar}}}$ as the measure of how fast or slow the bar is, since this gives a greater insight into the disc dynamics than pattern speed (see Sec. 1.3). $\mathscr{R}$ requires the bar length and corotation radius, which I calculate at two times for each halo: 0.5 Gyr after the time of bar formation, t_{i}, and at the end of the simulation, at $z = 0$.

Fig. 2.5 illustrates an example of the procedure I use for finding bar lengths for Auriga 24 at $z = 0$, in the final snapshot of its simulation. I first find the contours to the face-on stellar surface density, of which I show every 10^{th} calculated contour in the upper left

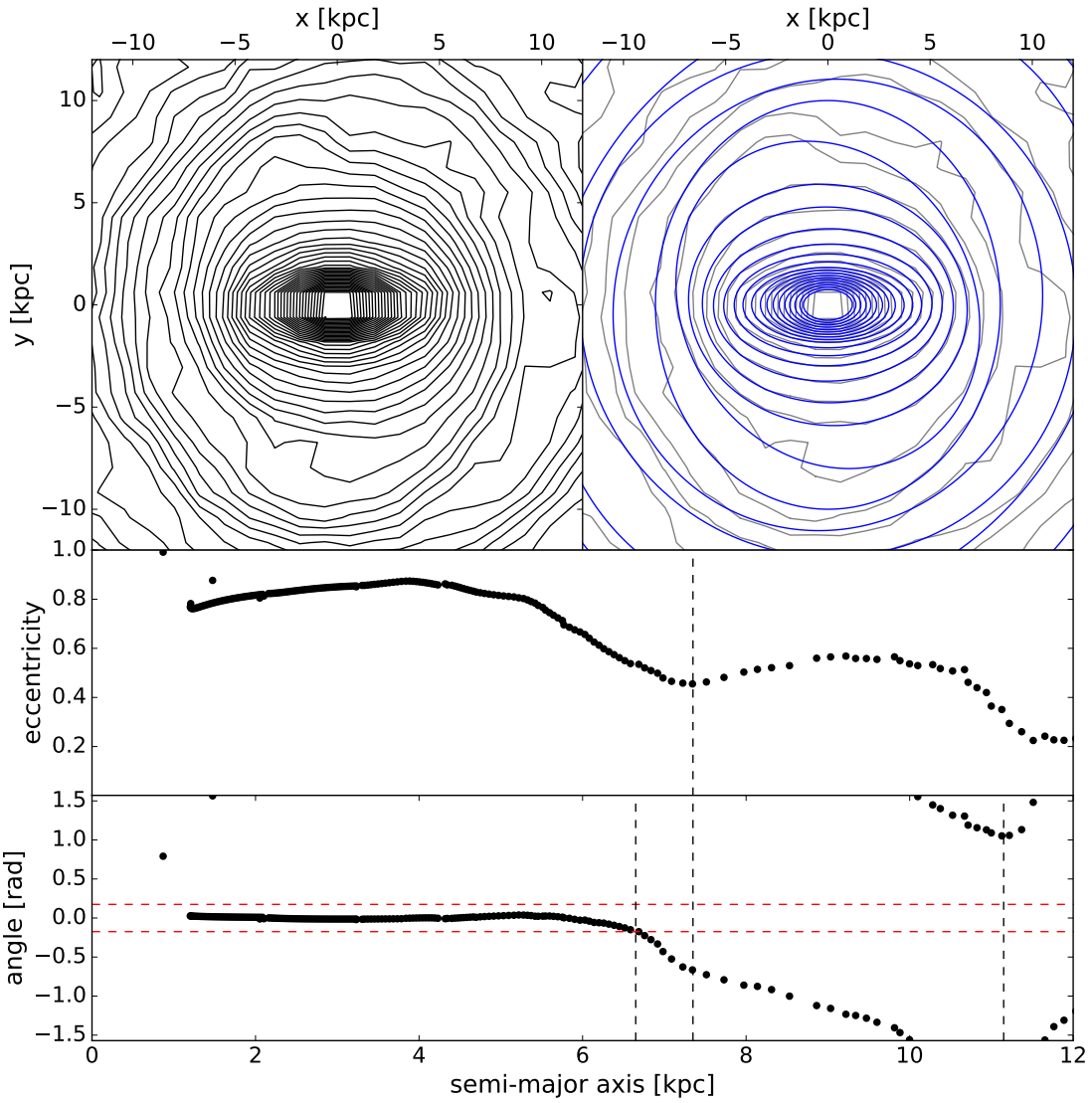


FIGURE 2.5: An illustration of the ellipse method for finding the bar length for Auriga 24 at $z = 0$. Top left: the contours of the face-on stellar surface density profile within 12 kpc. Top right: the ellipse fitting (blue) to the largest closed loop of each contour level from the previous panel (grey). Middle: the eccentricity plotted against semi-major axis of each ellipse fitted. Bottom: the angle plotted against semi-major axis of each ellipse fitted, with $\pm\frac{\pi}{12}$ rad shown by the red dashed lines. In both the lower two panels, the vertical grey dashed lines indicate the radius of the three features used to determine the bar length.

panel of Fig. 2.5. For each contour level, I fit an ellipse to the longest closed loop, centred on the origin, as shown in the upper right panel in blue.

The lower two panels show the eccentricity and angle from the aligned bar axis respectively, against the semi-major axis of each ellipse up to 12 kpc. The bar length is then the minimum of three radii: the first minimum in eccentricity outside the visually strong bar region, the first turning point in angle outside the visually strong bar region, and the first deviation in angle of more than $15°/\frac{\pi}{12}$ rad from the bar axis (excluding the inner 1 kpc which shows little bar signal). These three radii are shown in Fig. 2.5 as the middle, right, and left vertical dashed lines respectively. In this case, I find a bar length of 6.5 kpc, corresponding to the left-most dashed line.

To match observations where only one time is available, I take bar length measurements from the individual snipshot for each initial and final time. However, there are effects which can introduce inaccuracies, most notably artificial lengthening of the bar from spiral arms temporarily aligning with the ends of the bar (see Bissantz & Gerhard, 2002; Quillen et al., 2011; Hilmi et al., 2020). To acknowledge this in my results, I compute a measure of uncertainty as the range of bar lengths found for a few snipshots within 100 Myr of the quoted time. For temporary/oscillating inaccuracies in the bar length measurement, these uncertainties should reliably encompass the true bar length.

For the corotation radius, I take the pattern speed Ω_p and the circular rotation velocity curve (as calculated from the total mass inside spherical bins centred on the origin) at each snapshot, and interpolate the rotation curve across each snipshot (except for Auriga 18, where this interpolation is not necessary). I then interpolate the resulting circular rotation curve with respect to radius to match the pattern speed and find the corotation radius.

The second panel of Fig. 2.4 shows illustrative versions of these lengths at each snipshot. The blue line is the corotation radius as calculated above, and the white crosses are the bar lengths from ellipse fitting which I use throughout Chapter 4. The black line gives the radius of the disc, here defined as the first radial bin in the disc plane for which the stellar surface density drops below 1 $M_\odot$ pc^{-2}. I also show a second version of bar length in this figure, which I call R_{A2}, in the orange line. This takes the first radial bin to drop

below 0.7 $A_{2,\mathrm{max}}$ in each snipshot. This calculation is more easily automated, so helps to show the continuous evolution of parameters for Chapter 3, however R_{A2} is more susceptible to being artificially extended by galaxy interactions. Observations also tend to use ellipse fitting to find bar lengths in external galaxies, so taking a similar method improves comparison with observations. Despite bar lengths from ellipses tending to be longer than those from Fourier decomposition (Ghosh & Di Matteo, 2024), the results of Chapter 4 are qualitatively broadly similar when using R_{A2} instead of R_{bar}.

The bottom panel of Fig. 2.4 shows that the resulting rotation rate, $\mathscr{R}_{A2}$, is approximately constant, after initially decreasing for the first few Gyr signifying an early speed-up. The white crosses in the bottom panel show $\mathscr{R}$ calculated from R_{bar} instead – in this case the two versions of bar length are very similar, and so the white crosses match the blue line at both times.

2.2.1.4 Further galaxy properties

Similarly to the angle and strength of the bar, calculated in Sec. 2.2.1.1, I also calculate the angle and strength of any S shaped warp within the galaxy. I find this using the first Fourier mode, applied to the mean height from the x-y plane (i.e. $\bar{z}$) in 5° bins for each of the 250 pc-wide radial annuli used for A_2 (but extended to a height of 10 kpc from the x-y plane to capture the full behaviour of $\bar{z}$). This gives the angle of the warp axis $\Theta_{1,\mathrm{warp}}$ (perpendicular to the line of nodes) and magnitude $Z_{1,\mathrm{warp}}$ of the warp at each radius by:

$$\Theta_{1,\mathrm{warp}} = \arctan \frac{\sum_k \bar{z}\left(\theta_k\right) \sin \theta_k}{\sum_k \bar{z}\left(\theta_k\right) \cos \theta_k} \tag{2.3}$$

$$Z_{1,\mathrm{warp}} = \sqrt{\left(\sum_k \bar{z}\left(\theta_k\right) \cos \theta_k\right)^2 + \left(\sum_k \bar{z}\left(\theta_k\right) \sin \theta_k\right)^2} \tag{2.4}$$

where θ_k is the angle to the x-axis at the centre of each 5° bin and $\bar{z}\left(\theta_k\right)$ is the mean height in that bin. This magnitude $Z_{1,\mathrm{warp}}$ is not normalised, and indicates the maximum

height of the $m = 1$ warp pattern at that radius. I also calculate the angle to the x-y plane which this magnitude represents at each radius R as

$$\Phi_{1,\mathrm{warp}} = \arctan \frac{Z_{1,\mathrm{warp}}}{R} \tag{2.5}$$

In addition to the parameters above, in what follows I also use the virial mass, the stellar mass within 20 kpc, and the baryon dominance within one effective radius. The last of these is calculated as the ratio of the circular velocity at the effective radius induced by the enclosed stellar mass to the circular velocity at the effective radius from the total enclosed mass. Many of these parameters vary apparently randomly on short timescales. For most parameters, I account for their dispersion by taking the mean value across 200 Myr (40 snipshots), with the standard deviation from the same interval giving a basis for the error bars shown below – these error bars are propagated through as uncertainties for derived quantities.

2.2.2 Galaxy interaction parameters

To parametrise the accretion and interaction history of each Auriga halo, I use the masses, positions, and velocities from their merger trees. Using the merger tree, I calculate, for each snapshot output time, the Elmegreen parameter S (Elmegreen et al., 1991) for each halo within 50 kpc of the main halo[3]. This parameter gives a dimensionless measure of the tidal forces imparted during the course of an interaction. The Elmegreen parameter S is given by

$$S = \left(\frac{G m_\star M_\mathrm{p} R_\mathrm{g}}{{R_\mathrm{p}}^3} \tau_\mathrm{p}\right) \left(\frac{m_\star R_\mathrm{g}}{\tau_\mathrm{g}}\right)^{-1} = \frac{M_\mathrm{p}}{M_\mathrm{g}} \left(\frac{R_\mathrm{p}}{R_\mathrm{g}}\right)^{-3} \frac{\tau_\mathrm{p}}{\tau_\mathrm{g}} \tag{2.6}$$

where M_p is the total mass of the perturbing halo, M_g is the total mass of the central halo, R_p is the distance between the centres of the two halos, R_g is the extent of the disc in the main halo, τ_p is the time taken for the perturber to orbit 1 rad around the central

[3]The Elmegreen parameter is strictly intended for use at pericentre passage, but the quantities used to calculate it are meaningful at any time

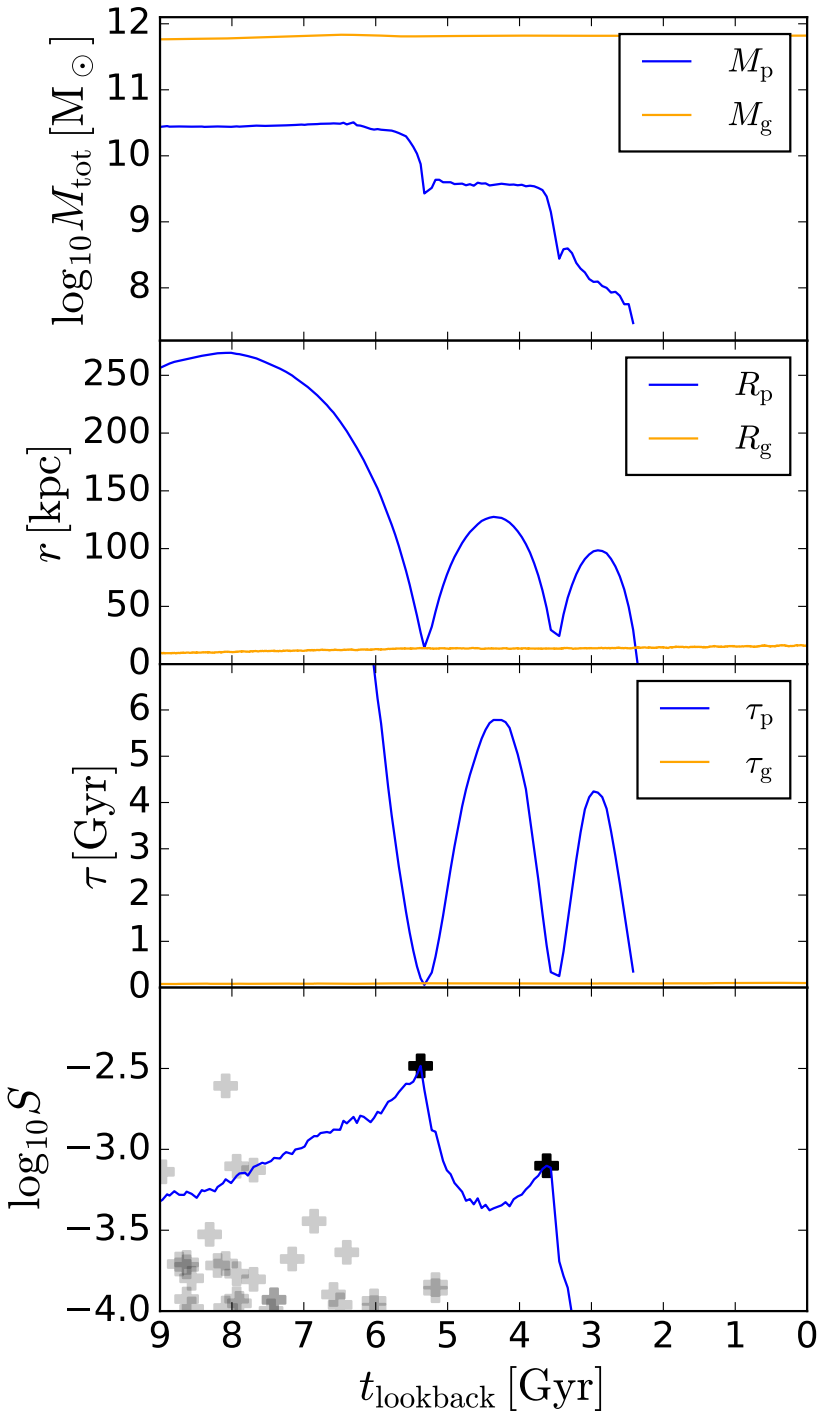


FIGURE 2.6: An illustrative example of the Elmegreen parameter calculation for one interacting halo in Auriga 22. Shown against lookback time, the panels show from top to bottom: the halo mass for the perturber (blue) and main halo (light orange); the distance between the main halo and the perturber (blue) and the extent of the disc in the main halo (light orange); the time to complete 1 rad of orbit around the centre of the main halo for the perturber (blue) and stars at the edge of the disc (light orange); the resulting Elmegreen parameter (blue line) with its local maxima (black crosses). Other interactions in Auriga 22 are shown by the grey crosses.

halo (from its angular velocity at that time), and $\tau_g = \sqrt{\frac{R_g^3}{GM_g}}$ is the time taken for a star (of mass $m_\star$) on a circular orbit at the edge of the disc to orbit 1 rad.

The first expression for S in equation 2.6 is arrived at directly from the physical motivation for the parameter: it is the ratio of the tidal impulse imparted to a star in the outer disc by the perturber (left bracket) and the momentum of such a star in its assumed circular orbit (right bracket). This, in effect, gives the relative impact of the tidal force on stars in the outer disc over the course of the interaction. While the first expression of equation 2.6 is already dimensionless, one can remove constants from the expression by substituting for τ_g, thereby arriving at the second expression for S in equation 2.6. For further details, see Elmegreen et al. (1991).

In Fig. 2.6, I illustrate S and its component parameters for one example interaction from Auriga 22. The top panel shows the mass terms, with M_p in blue and M_g in orange. The perturber is less massive than the main halo, and over the course of their extended interaction the main halo accretes matter from the perturber. The accretion concludes with a merger at ~ 2.5 Gyr lookback time, with M_p dropping significantly before being fully accreted into the main halo. The Elmegreen parameter is larger for higher mass ratios, since these have a larger impact on the main galaxy; as accretion progresses, this contributes a decreasing factor to S. The second panel shows the distance terms, with R_p in blue and R_g in orange. The disc extent R_g is calculated according to the definition given in Sec. 2.2.1.3. One can see the disc growing over time, while the perturber experiences three pericentres in a decaying orbit. Since closer interactions produce stronger forces, the Elmegreen parameter is larger when the perturber is closer to the centre of the main halo relative to the disc extent, so is increased around pericentres. The third panel shows the time terms, with τ_p in blue and τ_g in orange near the lower axis of the panel. The total force imparted by the perturber is larger when it acts over a longer time (greater τ_p) and this is included in the Elmegreen parameter, normalised to τ_g. As such, increases in S from the short separation at pericentres are somewhat reduced by the shorter times involved as the perturber speeds up near pericentre.

The final panel of Fig. 2.6 shows S at each snapshot for this example interaction, compiling the behaviours of the individual quantities described above into one value,

shown as the blue line. From the evolution of S, I take the local maxima (defined as any snapshot whose value of S is larger than any other snapshot within $\sim$ 1 Gyr) to be the strength and time of the interaction. For this example, this approach yields two interactions for the perturber from its first two pericentres – by the time of the merger, the perturber's mass is too low to produce a significant tidal effect. I show these maxima of the blue line as black crosses. I also show the maxima for other interacting halos with Auriga 22 as grey crosses. One can see there are a few other small interactions after the bar forms at $\sim$ 6 Gyr, but the example highlighted here with the blue line and black crosses dominates the external forces on the main halo.

I employ this method of local maxima rather than simply calculating S at pericentre for two reasons. Firstly, for a merging galaxy there is no well defined pericentre for its final accretion as it disappears from the merger tree, whereas the maximum S can be reliably found in all cases. Secondly, during close orbits and mergers, the halos of the two galaxies can mix, most often artificially decreasing the recorded mass of the interacting galaxy for single snapshots (see Sec 7.4 of Springel et al., 2021, for an examination of this effect) and producing an artificially lower value of S. By taking the local maximum of S, I avoid an extremely low value if this effect is significant for the snapshot at pericentre, taking the next best snapshot instead.

Chapter 3

Did the Gaia Enceladus/Sausage merger form the Milky Way's bar?

This Chapter is structured as follows. In Sec. 3.1 I describe the Auriga 18 simulation and the details of the new approach used for my rerun. I present my results in Sec. 3.2, and discuss the implications of these results on bar formation in the Milky Way and simulated analogues in Sec. 3.3.1. Additionally, in Sec. 3.3.2, I briefly examine the wider effect of the GES merger on the main Milky Way analogue including the extent and orientation of its disc. I lastly summarise and conclude my results in Sec. 3.4.

3.1 Simulations used

3.1.1 Auriga 18

In this Chapter, I focus on the Auriga 18 simulation, as this galaxy has previously been found to be a close Milky Way analogue. Fragkoudi et al. (2020) examines the chemodynamic properties of the discs and bulges of the Auriga galaxies and identifies Auriga 17 and 18 as being very similar to the Milky Way. They find that the metal-poor stars in these galaxies' bulges have a thick disc-like morphology and are rotating almost as quickly as the metal-rich population, consistent with the Milky Way (Ness et al., 2013).

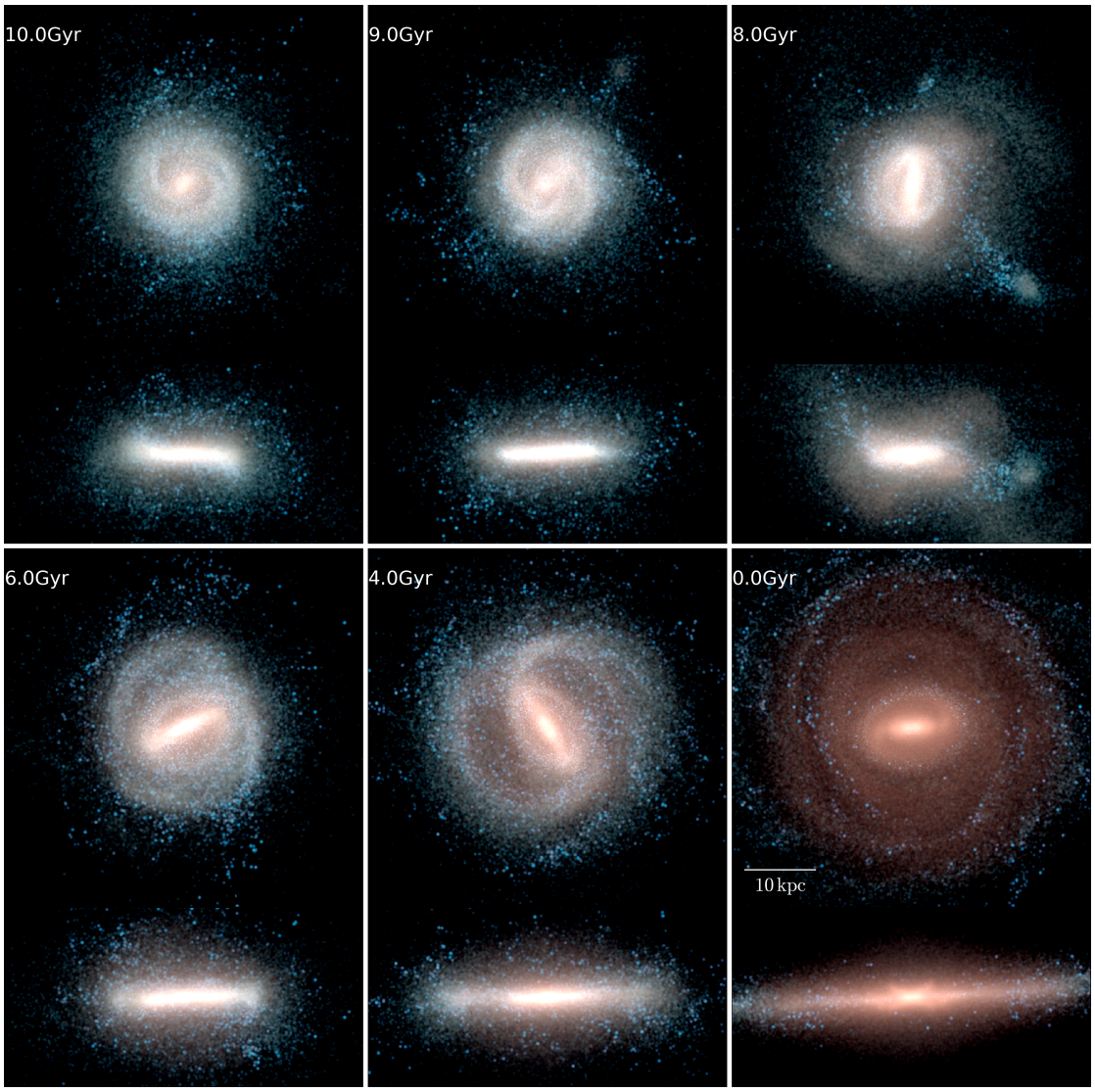


FIGURE 3.1: Six face-on and edge-on projections of Auriga 18 at various snapshots throughout the simulation. This uses the same approach as in Fig. 2.1, Fig. 2.2, and Fig. 2.3.

In addition, both galaxies have bars and their bulges show a prominent boxy/peanut shape which, for Auriga 18, can be prominently seen in the edge-on projection at 0.0 Gyr in Fig. 3.1. Fattahi et al. (2019) also identifies Auriga 17 and Auriga 18 (among others) as having a halo dominated by metal-rich, highly eccentric stars similar to the population identified as belonging to GES in Belokurov et al. (2018) and Helmi et al. (2018). Both of these simulations represent a path of evolution to create the Milky Way as seen today, including its bar, so examining the cause of their bars' formations can shed light onto the Milky Way's real evolution. Of the two, Auriga 18 existed with more frequent snapshots at the time of this research, so I chose this simulation for the study presented here.

Auriga 18's chemodynamics are a result of a merger history which is also similar to that of the Milky Way. Auriga 18 has a quiescent merger history, with no major mergers in the last 12 Gyr of its evolution (Fragkoudi et al., 2020). Its radially biased metal-rich component in the inner halo is a result of a GES-like merger which Auriga 18 experiences during this quiescent period at around 9 Gyr ago (Fattahi et al., 2019) with a lower but broadly consistent stellar mass ratio of 5% (Fragkoudi et al., 2020). The latter stages of this merger can be seen at 8.0 Gyr in Fig. 3.1. I will refer to this merging dwarf galaxy in Auriga 18 as GES-18.

3.1.2 Re-simulation

In order to explore the effects caused by the GES-18 merger itself on my Milky Way analogue, I rerun the Auriga 18 simulation without GES-18, aiming to modify only this element of the galaxy's history. To achieve this, I use the merger-tree to identify the unique identifiers of each dark matter particle belonging to the GES-18 halo at the snapshot when it is at its peak halo mass. I then remove all of the particles with these identifiers at the earlier snapshot corresponding to $z = 4$. The resultant altered version of this snapshot is then used as the initial conditions from which I run the simulation again. I use the same code and outputs as for the original 3000 snapshot Auriga 18, with the only difference being a later start-time with some particles removed as described.

While I do not remove the baryonic matter associated with GES-18's progenitors, the halo is still in the process of assembling at this time and therefore its baryonic content is too scattered (and too light without the dark matter) to form the galaxy. The removal does also result in a slight change in cosmology due to the marginally decreased dark matter content of the simulation box, as well as a more significant reduction in the final mass of the main halo. The former is a small enough change that one would not expect any significant effects by the end of the simulation, while the latter is to be expected from the removal of a merger. I use the merger tree to identify the halo corresponding to Auriga 18 in each snapshot.

Rey et al. (2023) also alter a simulation to study the impact of GES-like mergers on a Milky Way like host, producing five examples of merger histories with GES-like mergers at different mass ratios. They use genetic modification of their zoom-in simulation's initial conditions, giving a consistent background cosmology and final halo mass in each case by assigning the mass removed from their GES analogue elsewhere. However, for the purposes of this Chapter, I opt for simply removing the GES-18 halo in order to reduce the impact of changing other aspects of Auriga 18's accretion history, even if it leads to a less massive halo.

The main halo of this rerun is visually indistinguishable from the original simulation up until a lookback time of 9 Gyr, immediately before the GES-like merger event in the original run. The rerun does not experience this event, but it does experience its own later merger at a lookback time of 8 Gyr. This is the remnant of a secondary dwarf galaxy which, in the original simulation, merges with GES-18 after its first pericentre around Auriga 18. This new merger is retrograde and occurs at a lower mass ratio than in the original, so has less of an effect on the disc. The differences beyond 9 Gyr lookback time are therefore due to the GES-18's removal, rather than any changes to the cosmology or further changes to the halo's wider accretion history.

3.2 Results

3.2.1 Bar formation in Auriga 18

Fig. 3.2 shows the evolution of the bar and the GES-18 merger event throughout Auriga 18's history. The top panel shows a 2D histogram of A_2 as a function of radius and time, and the second and third panels show the bar strength (maximum A_2 within the disc) and distance between GES-18 and Auriga 18 respectively as functions of time. By examining the bottom panel, one sees that GES-18's main progenitor forms $\sim$ 200 kpc from Auriga 18 before beginning its approach at a lookback time of around 10 Gyr. This approach reaches its first pericentre at 8.9 Gyr ago, before splashing back to a distance

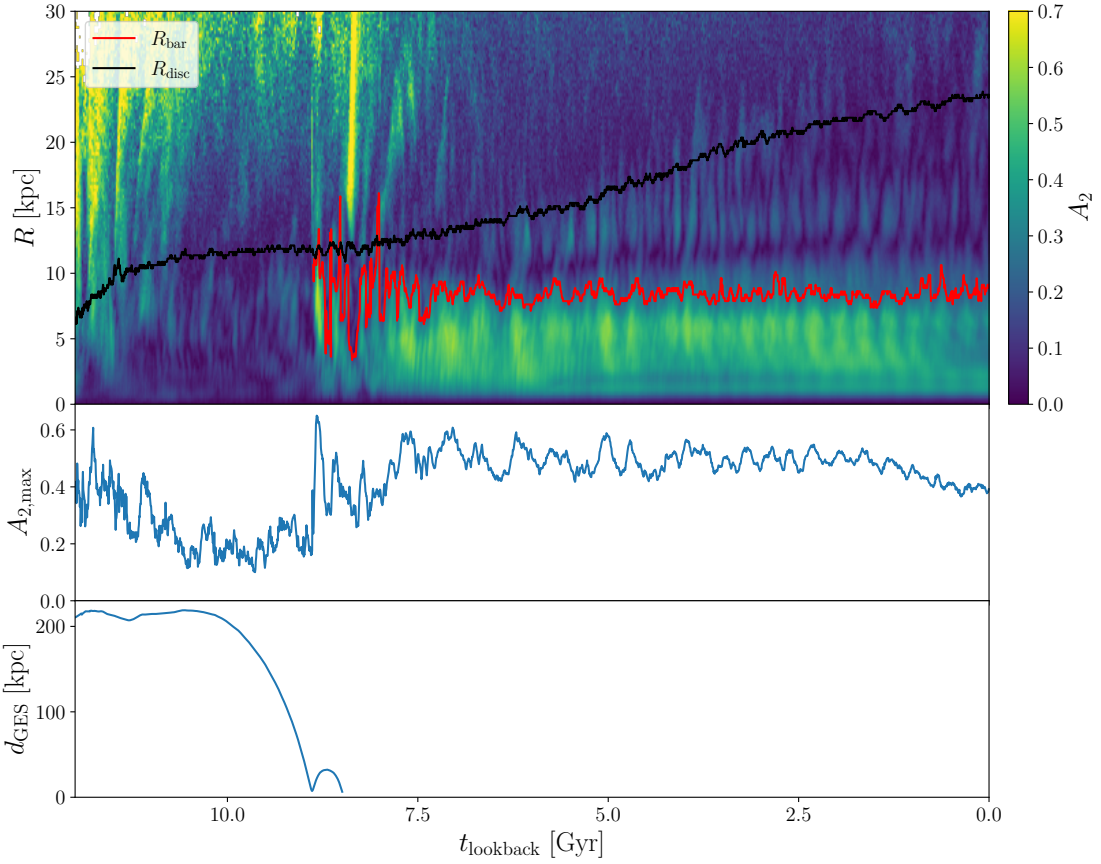


FIGURE 3.2: Evolution of the bar and the disc throughout the simulation. The colour scale in the upper panel gives the magnitude of the A_2 Fourier mode in the stellar disc as a function of lookback time and radius in the disc plane. I overlay the extent of the bar and the disc in red and black respectively, with the bar length only being shown after the bar strength has increased beyond 0.25 for the final time. The middle panel shows the stellar bar strength, as calculated in Sec. 2.2.1.2 from the maximum A_2 mode within the extent of the disc. The lower panel shows the physical distance between the centres of the main Auriga 18 halo and GES-18 until the time of their merger.

of 30 kpc and finally merging with Auriga 18 at 8.5 Gyr as defined by the merger-tree code.

The time around the first pericentric passage of GES-18, i.e. between 9 – 8.5 Gyr, appears to separate two phases of Auriga 18's evolution. During the 2 – 3 Gyr before this, the disc is relatively axisymmetric in its inner regions, as can be seen by the low A_2 values in the middle panel of Fig. 3.2 with the extra radial information of the top panel showing spiral arms and some amount of left-over turbulence from its formation maintaining $A_{2,\rm max} \approx 0.2$. The extent of the disc itself is also relatively constant during this time. After this transition, Auriga 18 forms a bar which persists until the end of the simulation at a relatively constant strength of 0.5. The length and corotation radius of

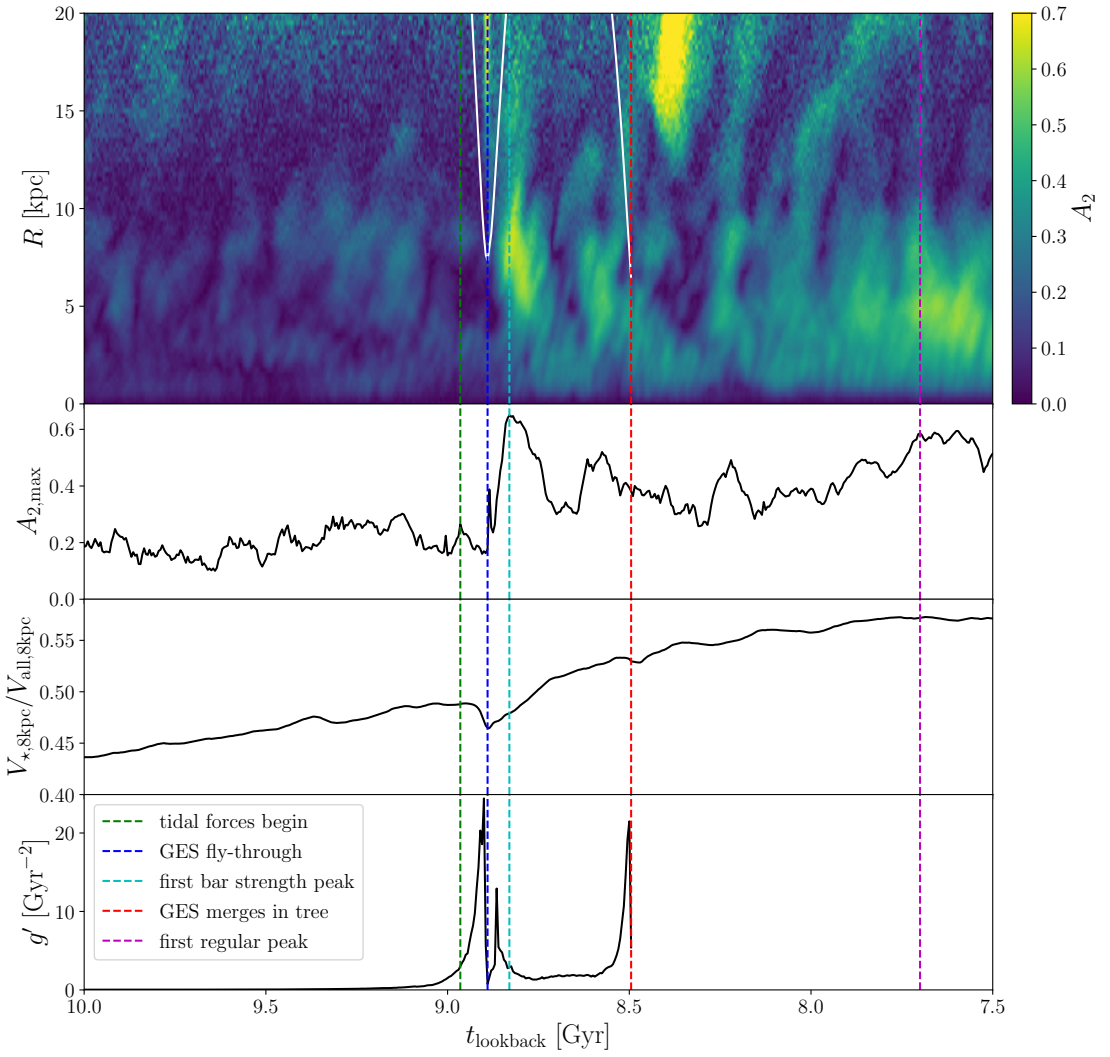


FIGURE 3.3: The evolution of a selection of galaxy properties in Auriga 18 at lookback times of 10 – 7.5 Gyr. Top panel: magnitude of the A_2 Fourier mode in the stellar disc at radii up to 20 kpc. The distance from Auriga 18 to GES-18 is overlaid in white. Second panel: bar strength. Third panel: baryon dominance within the inner 8 kpc of the disc, shown as the rotation velocity due to stars at 8 kpc divided by the total rotation velocity at the same radius. Bottom panel: The approximate tidal field induced by GES-18 at the centre of Auriga 18. The vertical lines indicate the time at which, from left to right: tidal forces first become significant in Auriga 18 (green); GES-18 experiences its first pericentre around Auriga 18 (blue); the bar strength first peaks significantly (cyan); GES-18 and Auriga 18 become one subhalo in the simulation's merger tree (red); the bar strength reaches the oscillating state in which it remains for the next 5 Gyr (magenta).

this bar are also constant from 7.5 Gyr onwards (8 kpc and 9 kpc respectively, making for a fast bar), while an increased rate of disc growth is maintained until the end of the simulation so that the bar is a similar size to the disc early on but only exists in the inner third by $z = 0$.

Fig. 3.3 provides a closer look at how Auriga 18 changes during this transitional epoch. In the upper panel I show a portion of Fig. 3.2's upper panel to zoom in on the radial dependence of A_2 for lookback times $10 - 7.5$ Gyr, with the distance between GES-18 and the centre of the main halo represented by the white curve. The other three panels show the bar strength, inner baryon dominance, and tidal field strength across the same time period. Prior to GES-18's first pericentre, the A_2 mode is most prevalent at radii of $5 - 10$ kpc although still weak. This is indicative of spiral arms in the outer disc, features which can be seen in the upper-left and upper-middle panels of Fig. 3.1. There are low amplitude perturbations in the inner disc, but these are weaker than 0.2, the value typically used to represent the formation of a bar.

Immediately after the first pericentre at 8.9 Gyr, the A_2 spikes in the outer disc. This perturbation moves inwards within 100 Myr and settles across the inner 4 kpc for 200 Myr before dissolving into axisymmetry. At the same time, a second perturbation is formed in the outer disc and similarly moves inwards so that there is again a bar in the inner 4 kpc just 100 Myr after the first bar dissolved. It is worth noting that this second perturbation does not follow GES-18's second pericentre, in fact preceding it by 200 Myr. This pattern of dissolving and being replaced by a new perturbation from the outer disc occurs a third time before the inner 6 kpc form a long-lasting bar, whose length and strength settle towards 8 kpc and 0.6 respectively by 7.7 Gyr. The pattern described matches that occurring in Lokas (2018) where, in multiple cases, a purely tidal interaction forms a bar by first perturbing the less gravitationally bound outer regions. I examine the implications of this similarity in Sec. 3.3.1.1.

Visible in Fig. 3.2, there is some oscillation continuing to $z = 0$, with the bar strength oscillating between 0.45 and 0.55 and the bar length between $7.5 - 10$ kpc, both with a period of ~ 0.25 Gyr. As Hilmi et al. (2020) shows, this can be caused by the bar interacting with the spiral arms, since as spiral arms line up with the ends of the bar they appear to lengthen the bar and increase the A_2 mode. The oscillation may also be a projection effect due to my alignment of the galaxy, since this period almost exactly matches the bar's pattern speed of ~ 28 rad Gyr^{-1}.

The second panel of Fig. 3.3 shows the more widely used, single-valued, bar strength measurement of $A_{2,\mathrm{max}}$, as described in Sec. 2.2.1.3. This provides broadly similar information of a weak/non-existent bar up until a sudden jump at 8.8 Gyr, followed by a period of wide variation at lower amplitudes, and ending with a higher, more consistent bar strength up until a buckling event from 1.5 Gyr onwards slightly reduces the bar strength. In this case though, this measure is limited in details. Auriga 18's spiral arms contribute to a higher early strength, and the outer disc perturbations are indistinguishable from a strong bar. While I continue to use this measure for a quantifiable bar strength, I use the A_2 radial profile to help identify the features which contribute to the strength.

Auriga 18's stellar profile is also changed around this time. The third panel, even accounting for the halo-mixing effects (see Sec. 7.4 of Springel et al. (2021) for a description of this effect) as GES-18 infalls, shows a sharp increase in the baryon dominance inside 8 kpc ($V_{\star,8\mathrm{kpc}}/V_{\mathrm{all},8\mathrm{kpc}}$) from 8.9 – 8.5 Gyr. This is the greatest departure from Auriga 18's normal evolution of baryon dominance across the entire simulation, and implies either a large depositing of stars directly from GES-18, a sudden increase in star formation or a transition to a more centrally concentrated stellar density profile as soon as GES-18 first interacts with Auriga 18. I examine this further using Fig. 3.4 below.

The bottom panel of Fig. 3.3 shows the tidal field placed on the main halo by GES-18. This is negligible for most of the time shown, but peaks sharply at both GES-18's first pericentre and its merger time. The first of these peaks in tidal forces is the time at which many of the previously discussed changes in Auriga 18 occur.

Fig. 3.4 shows the radial distributions of stars (top) and gas (bottom) over the same time period as in Fig. 3.3, and suggests a combination of increased star formation and a shift in stellar density profile occurring directly after GES-18's first pericentre. The lower panel shows a galaxy-wide migration of gas in Auriga 18 beginning 8.9 Gyr ago, with the mass distribution's peak shifting from a radius of 6 kpc to 4 kpc as a result. Furthered by accretion of gas from GES-18, this creates a very dense environment of gas in the inner few kpc of the disc. In the upper panel, one sees a less extreme version of this migration happen for the stellar component of Auriga 18, visible as a reduced

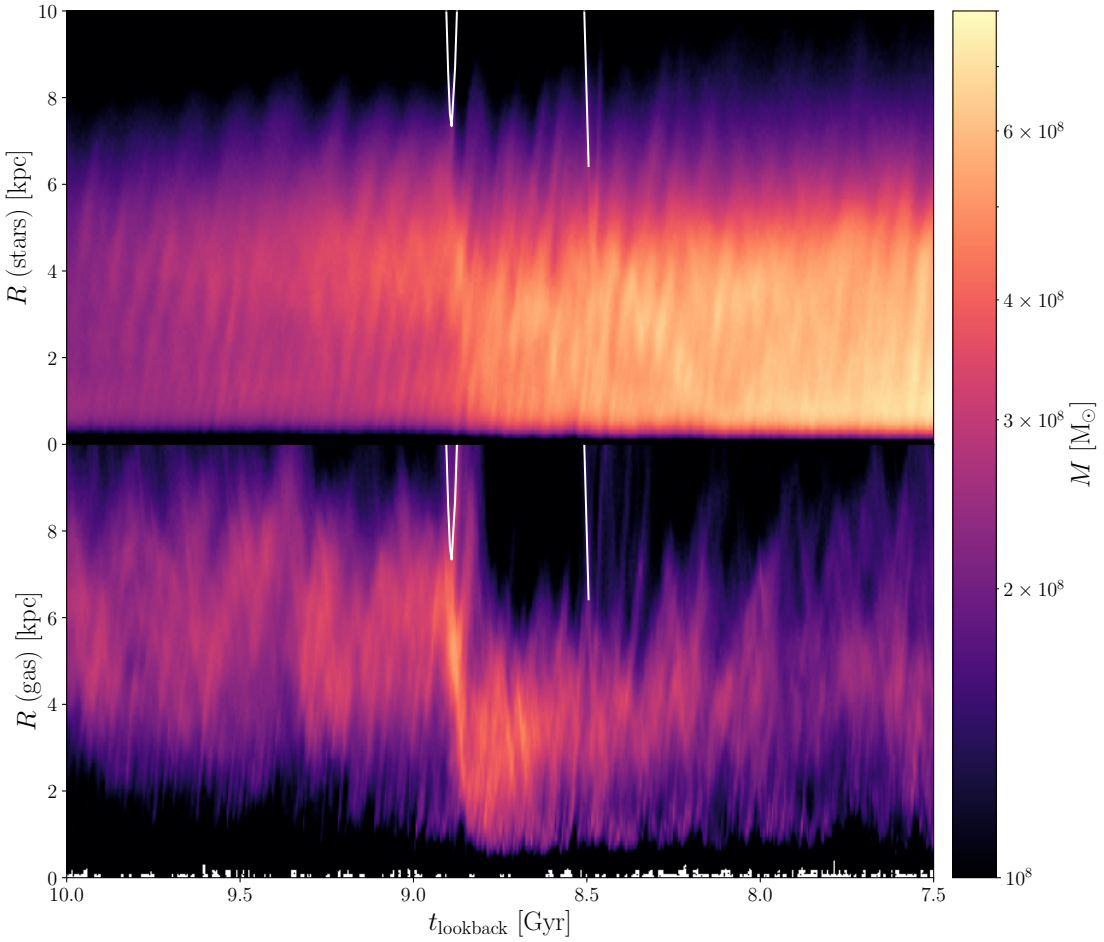


FIGURE 3.4: The total mass at each snapshot in each 0.1 kpc annulus of star particles (upper) and gas cells (lower) in Auriga 18 at lookback times of 10 – 7.5 Gyr. The colour scale showing this mass is logarithmic. In both panels, I show the distance between the centres of GES-18 and the main halo by the white line.

stellar mass in the 5 – 6 kpc region. However, the dominant change in stellar distribution at GES-18's first pericentre is a sudden increase in star formation in the inner 4 kpc of the disc. This star-burst is sustained for almost 1 Gyr, as seen by the depletion of gas in the lower panel and noted in Grand et al. (2020), and fundamentally changes the stellar distribution in Auriga 18. Therefore the migration of gas inwards following GES-18's first interaction with Auriga 18 appears to induce a dramatic rise in the dominance of stars in Auriga 18's inner disc.

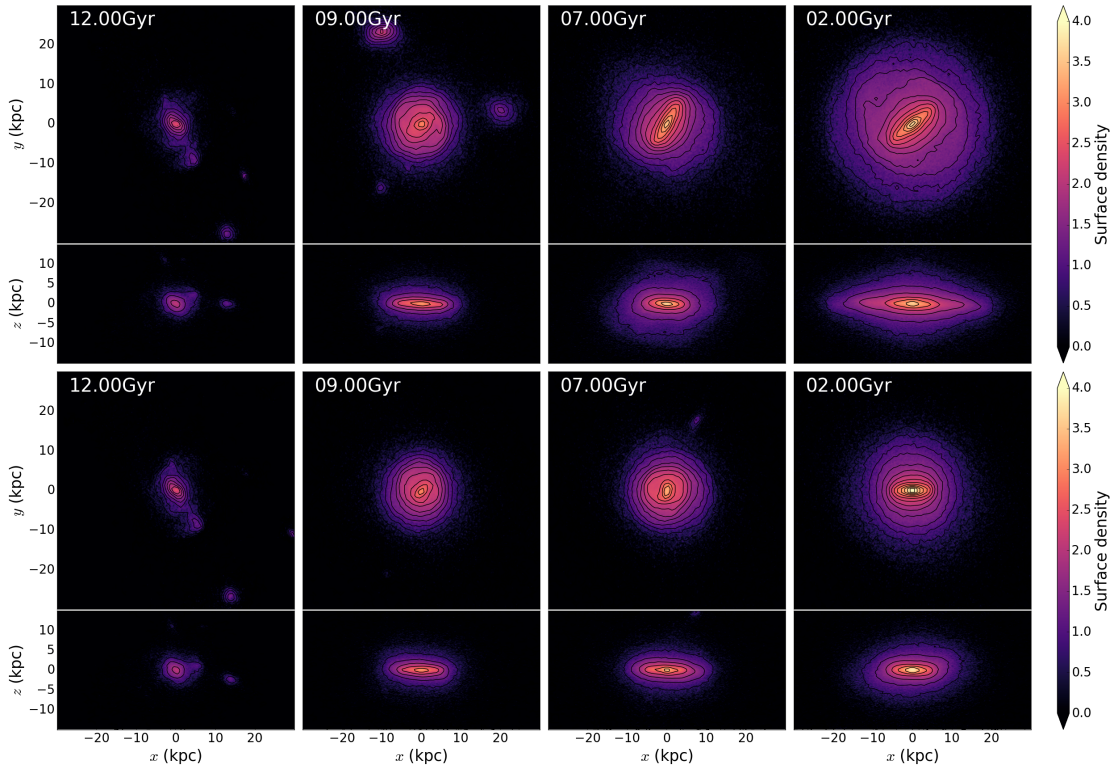


FIGURE 3.5: Face-on and edge-on stellar surface density profiles for each of Auriga 18 (top) and my rerun (bottom) at four different snapshots: 12 Gyr, shortly after the initial conditions of the rerun; 9 Gyr, as GES-18 approaches in the original; 7 Gyr, following the interaction period; 2 Gyr, once both simulations have almost fully evolved but before the rerun's polar disc (a new stellar disc almost perpendicular to the pre-existing disc) dominates the young stellar population. The surface density colour-scale is measured as the particle count per bin and is logarithmic.

3.2.2 Comparison to a controlled counterpart simulation

In this section I present results from my controlled resimulation described in Sec. 3.1.2, in which I remove the GES-like galaxy from the simulation before it enters the main halo of the Milky Way-like galaxy. In the left panels of Fig. 3.5, I confirm that the main halos of each simulation match up until GES-18's first interaction in the original simulation. However, by a lookback time of 7 Gyr, shown in the middle panels, only Auriga 18 has a bar. In addition, the rerun's disc is less extended. By close to the end of the simulations, shown at 2 Gyr in the right panels, this difference in disc extension has grown dramatically and the rerun now has a denser central stellar profile. More crucial to this Chapter's question, the rerun also has a bar by this time; the removal of GES-18 has delayed bar formation rather than stopped it.

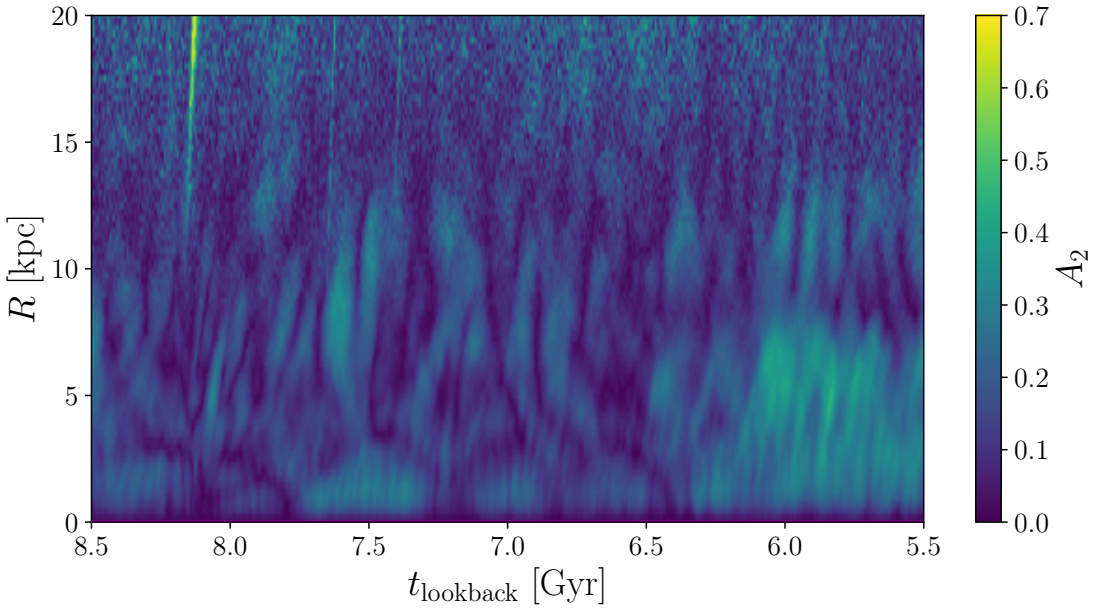


FIGURE 3.6: The magnitude of the A_2 Fourier mode in the stellar disc of my re-simulation, at radii up to 20 kpc and lookback times from 8.5 – 5.5 Gyr. The short peak in the outer regions shows the first pericentre time of the smaller merger. Note the absence of the tidal features clearly visible in Fig. 3.3.

The rerun experiences another somewhat significant merger even with the removal of GES-18. The first pericentre is visible in Fig. 3.6 as a transient peak in the A_2 mode outside of 10 kpc. This occurs at the later lookback time of 8.2 Gyr and at $\sim$ 25% of the total mass ratio and $\sim$ 40% of the stellar mass ratio of GES-18 in the original. As outlined in Sec. 3.1.2, this dwarf galaxy is involved in the original merger event, but only merges with GES-18 between GES-18's first and second pericentre, and as such was not removed. Without the influence of GES-18, this dwarf galaxy takes longer to reach the main halo, but does eventually merge in the rerun.

Despite this merger, the rerun does not form a bar at 8.2 Gyr ago either. Fig. 3.6 and Fig. 3.7 shows that while there is an excitation of the A_2 mode in the inner regions of the disc following the new merger, it only reaches a maximum amplitude of 0.3 before fading back to its state before the merger. This lasts 1.5 Gyr and at no point during this time does it form a visually distinguishable bar, instead having strong spiral arms which occasionally converge in the galaxy's centre.

The rerun's bar, which lasts until $z = 0$, in fact forms not long after the disappearance of this perturbation, growing from 6.4 – 6.0 Gyr. The bar experiences 1.5 Gyr of stability

at $A_{2,\max} = 0.4$ before growing further and buckling. During this period of stability it is therefore weaker than Auriga 18's bar. In addition, the A_2 radial profile differs from the original's during bar formation. Despite strong spiral arms producing higher A_2 in the mid-outer disc, the bar itself appears to quickly grow from the centre of the disc and outwards, rather than from perturbations moving inwards. This lengthening is not a persistent feature, since the bar which results after this growth period in the rerun does have a very similar bar length to the original despite the different radial A_2 patterns at their respective formation times. Nevertheless, these differing patterns during the bars' growth suggest a different mechanism of bar formation in the rerun in addition to the simple lack of mergers at the the time of bar formation.

Fig. 3.7 shows properties as a function of time from $12.5-0$ Gyr for both the original and rerun simulations. The top panel compares the simulations' bar strengths. The second panel shows both stellar mass and star formation rates for each, with the dark matter halos' masses in the panel below. The fourth panel shows the inner baryon dominance of each, and the final panel shows the extent of their respective discs.

In the top panel of Fig. 3.7 one clearly sees a consistent general behaviour of my bar strength measurement between the two simulations up until GES-18's first pericentre at a lookback time of 8.9 Gyr. At this time, the original's bar strength jumps up dramatically, due to the large perturbations of the outer disc found in Sec. 3.2.1, while the rerun's bar strength continues at a low value. While the original forms its bar, the rerun experiences its own merger but does not form a persistent bar following this. Instead, bar formation occurs at a lookback time of 6.1 Gyr, over 2 Gyr later than in the original with GES-18. The two galaxies can be seen to have very different evolution at late times, but the important takeaway is that both bars persist to the ends of their simulations.

In the three panels below this, I show the stellar mass, halo mass and previously defined baryon dominance respectively, for both the original and the rerun. These quantities are very similar for both up until lookback time 10 Gyr, with only the halo mass diverging at this point before the accretion of GES-18 in the original. Since inner baryon dominance is not affected by this, the dark matter accretion must occur at larger radii during this Gyr. After GES-18 causes a higher star formation rate in the original, one also sees a

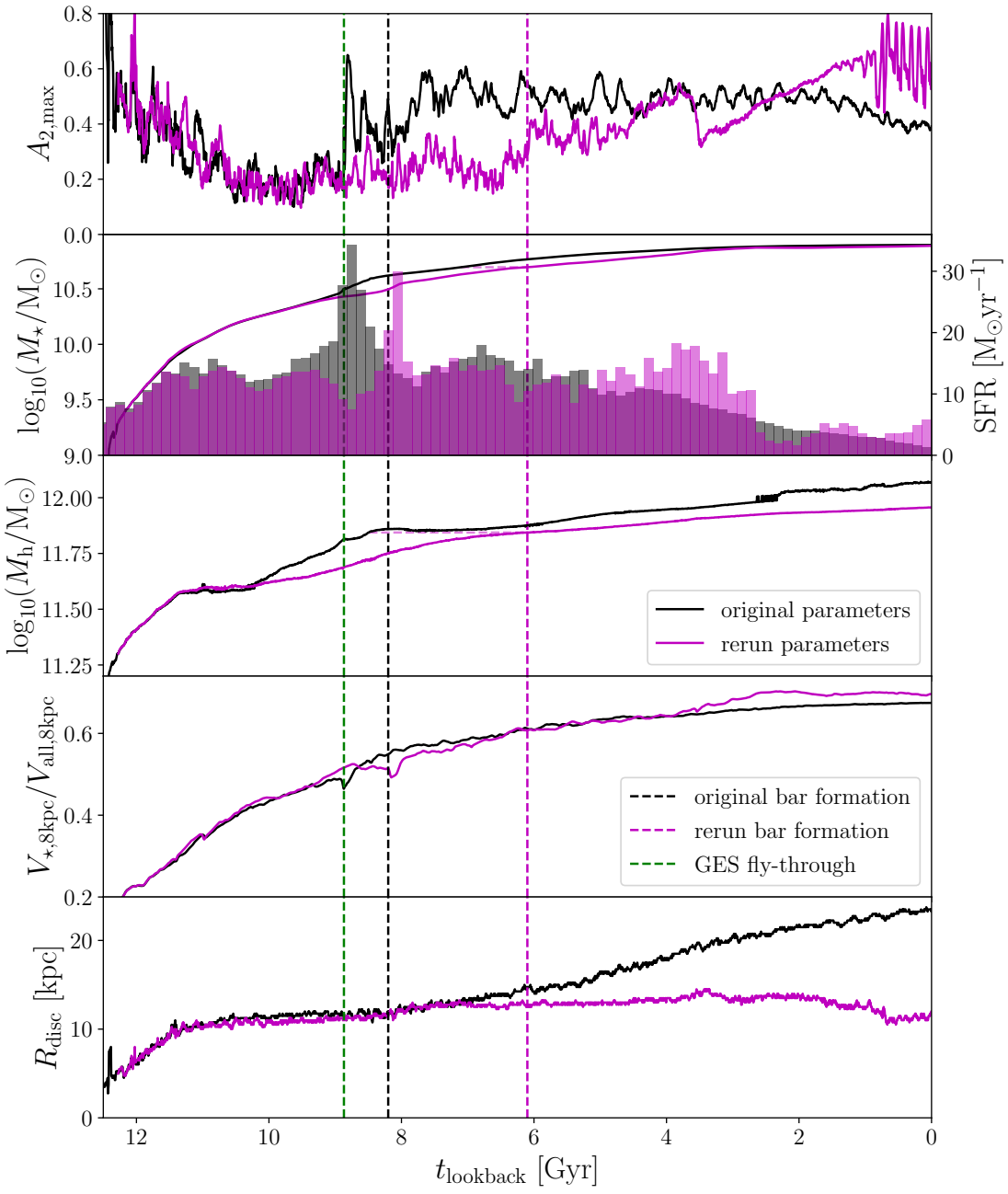


FIGURE 3.7: Comparison between Auriga 18 (black lines) and my rerun (magenta lines) of a selection of galaxy properties from the rerun's beginning until $z = 0$. Top panel: bar strength, from the A_2 Fourier mode. Second panel: total stellar mass. Third panel: total mass of the dark matter halo. Fourth panel: baryon dominance within the inner 8 kpc of the disc, shown as the rotation velocity due to stars at 8 kpc divided by the total rotation velocity at the same radius. Bottom panel: radial extent of the stellar disc. The vertical, dashed lines show, from left to right, the time of the GES-18's first pericentre in the original, Auriga 18's bar formation time (by visual inspection of the full A_2 profile), and my rerun's bar formation time. I also include horizontal lines to indicate the time at which Auriga 18 had the same properties as my rerun at the time of the rerun's bar formation.

slowing of dark matter accretion for the next 3 Gyr before both simulations continue to gain mass, both dark matter and stellar, at similar rates until at least 4 Gyr before the simulations' ends. Looking at just the times of bar formation in each, one sees that when the rerun forms its bar it has a higher stellar mass but a very similar halo mass to the original at its own time of bar formation. This further translates to baryon dominance being much higher at bar formation in the rerun than in the original. The original forms its bar when it attains a baryon dominance of 0.55, whereas the rerun forms its bar about 2 Gyr later for a higher baryon dominance of 0.6. This suggests very different internal environments in the two galaxies when they form their respective bars.

One also sees a dramatic difference between the galaxies at late times, with the most obvious change being the lack of growth in the extent of the rerun's disc from the bottom panel, when removing GES-18. The rerun also develops a polar disc (a new stellar disc almost perpendicular to the pre-existing disc) in the final 4 Gyr of the simulation, presenting as a reduced disc extent, increased inner baryon dominance, and widely varying bar strength in Fig. 3.7. I discuss these changes and their causes in Sec. 3.3.2, but these diverging properties occur well after both bars are established and do not therefore alter my main results.

3.3 Discussion

3.3.1 The link between GES and the Milky Way's bar

With the rerun not forming a bar until over 2 Gyr after the original, I can conclude that my removal of GES-18 is responsible for delaying bar formation. While there is some small difference between the two simulations before a lookback time of 9 Gyr, most notably in the total mass of the dark matter halo in the preceding 1.5 Gyr as shown in Fig. 3.7, the inner regions and the stellar component (see Fig. 3.5 also) remain practically identical until this time. In particular, my bar strength measurement shows the same behaviour in both simulations exactly until the merger time. Therefore I argue that the delay in bar formation is caused by the removal of the merger event itself, rather

than any other unintended changes to the galaxy's accretion history leading up to this point.

In addition, the temporary A_2 excitation in the rerun due to its smaller merger at 8.2 Gyr is an indication that Auriga 18 would be relatively stable against bar formation for a time without GES-18's merger. Since such an A_2 asymmetry dissipates on its own during this time, it is unlikely that internal mechanisms would have been able to form a bar before 6.5 Gyr ago as the beginnings of such a bar would dissipate in the same way as the observed A_2 feature. The removal of GES-18 not only delays bar formation but leaves a galaxy which is stable against bar formation for the next 1.5 Gyr. This in turn strongly suggests that GES-18 triggered the formation of Auriga 18's bar, particularly when considering the lack of internal bar development in both simulations prior to GES-18's first pericentre.

The mechanism of GES-18's triggering of Auriga 18's bar formation is less apparent, with the merger being a relatively chaotic time in the galaxy's history and as such many conditions changing quickly. In the following, I will focus on the tidal effects of GES-18 on Auriga 18 and the change in central baryon dominance immediately following the merger.

3.3.1.1 Tidal bar formation

The bottom panel of Fig. 3.3 shows the approximate tidal field (the spatial gradient of the gravitational field along the line connecting the two bodies' centres of mass) exerted on the centre of Auriga 18 by GES-18 around the the time of its merger. This sharply reaches its maximum of $24\,\mathrm{Gyr}^{-2}$ at its first pericentre, before just as sharply dropping while GES-18 splashes back and around Auriga 18. The tidal field peaks again to a similar magnitude at the merger time, when GES-18 experiences its second pericentre. Note that artificial halo-mixing due to overlapping dark matter halos during its closest approach is responsible for the brief decrease to almost $0\,\mathrm{Gyr}^{-2}$ at 8.9 Gyr as the majority of GES-18's halo is temporarily assigned to the main Auriga 18 halo instead in the simulation's code.

This initial peak in the tidal field at the first pericentre is also when the large A_2 perturbation begins in the outer disc. As described in Sec. 3.2.1, this perturbation soon propagates inwards before disappearing and propagating inwards from the outer regions a few more times. Lokas (2018) describes this same pattern of bar formation resulting from a purely tidal interaction. They use a set of N-body simulations to model four fly-bys of identical Milky Way-mass galaxies at varying strengths of tidal interaction. The result in each case but the weakest (as determined by the Elmegreen parameter S) is the formation of a bar in the prograde oriented galaxy, which is otherwise stable against bar formation for 3 Gyr. All of these tidal bars are formed via the process of repeated inwards-moving perturbations from the outer disc, similar to what I observe in Auriga 18, creating multiple instances of bars dissolving before a more permanent bar emerges. Since I see Auriga 18's bar forming in the same way as these tidal bars, with the bar forming 0.7 Gyr after this process begins, this suggests that Auriga 18's bar is a result of tidal forces from GES-18's first pericentre.

This is also consistent with the strength of the tidal interaction as determined by the Elmegreen parameter. One expects a permanent bar to be formed for $S > 0.04$ (Elmegreen et al., 1991). The GES-18 interaction has $S \sim 0.09$, which meets this criterion and is also similar to one of the bar-forming cases in Lokas (2018), at $S = 0.07$. This parameter encodes most of the broad information on the impact of a tidal interaction, but the angle of the perturber's approach compared to the angle of the galaxy's rotation is also important. Prograde encounters have a much stronger effect than retrograde encounters (Lokas, 2018) and intermediate angles fall on a corresponding scale (Lokas et al., 2014). GES-18 approaches at an angle of $\sim 70°$, which is slightly prograde, but highly inclined. As such, the true tidal effect of the merger is likely to be less than indicated by its Elmegreen parameter. It is worth noting, however, that GES-18 reorients the entire disc with its merger (see Sec. 3.3.2) which may reduce the weakening caused by its highly inclined approach.

It is also notable that the rerun does not form its bar in this way. This points to some difference in mechanism between the formation of the two bars, and the lack of significant mergers or fly-bys in the rerun at this time suggests that this difference can be accounted for by a lack of tidal interactions. The somewhat significant merger experienced by the

rerun $\sim$ 2 Gyr before bar formation exerts a maximum tidal field of just 4.7 Gyr^{-2}, 5 times less than GES-18 in the original. Additionally, this merger has a lower Elmegreen parameter of $S \sim 0.04$, placing it only on the threshold for bar formation and so less likely to trigger a bar than GES-18 which is well above the threshold. This suggests that only Auriga 18's bar, and not the rerun's, is formed by tidal forces and that the delay in bar formation which the rerun experiences is due to the lower magnitude of tidal interaction being insufficient to trigger bar formation.

3.3.1.2 Accelerated internal bar formation

In Sec. 3.2.1 I highlight the change in stellar distribution occurring at and after GES-18's first pericentre, which Fig. 3.4 shows is driven by the gas migrating to the inner regions and subsequently triggering an accelerated star formation rate across the next 1 Gyr. In the second panel of Fig. 3.7, I confirm that this is indeed an increase in star formation rate rather than purely accretion of stars from GES-18, since the star formation rate has its largest peak at this time, a peak which is also prolonged enough to produce such a dramatic shift in stellar density profile.

Since a high density of stars in the inner regions of a galaxy is conducive to bar formation, as is a low density of gas, this could instead be the trigger for Auriga 18's bar. However it seems more likely that this effect occurred alongside a tidal bar formation mechanism. The migration of the stars and gas occurs at the same time as the first major A_2 peak. The bulk of the migrating matter also follows the radius of the A_2 excitation as it moves inwards, suggesting that they occur as part of the same tidal event caused by GES-18. As the iterative outside-in A_2 perturbations continue, stars continue to form in the central regions as part of the star formation peak the migration triggers, while the gas density gradually decreases. At a lookback time of $\sim$ 8 Gyr, $V_{\star,8\mathrm{kpc}}/V_{\mathrm{all},8\mathrm{kpc}}$ reaches an approximately stable value and the stellar and gas density profiles appear to stabilise too. This also coincides with the time at which the bar stops oscillating with each new perturbation and becomes permanent. These observations suggest that the tidal forces from GES-18 create the initial bar-seeding perturbations in Auriga 18 and simultaneously cause the baryon migration inwards. As both processes continue,

conditions in the galaxy, specifically its inner stellar and gas densities, become able to support a bar. The continuing perturbations are therefore able to then take hold and form a long-lived and stable bar.

My rerun confirms that the tidal effects are needed to form a bar at this time in addition to the baryon density. Despite the 2 Gyr delay in bar formation, the rerun's inner baryon dominance in the third panel of Fig. 3.7 is similar to Auriga 18's at most times. This means that, as noted in Sec. 3.2.2, by the time of the rerun's bar formation its inner baryon dominance has increased to be higher than Auriga 18's was when it formed its own bar. In addition, the rerun's smaller merger, occurring just 0.5 Gyr after GES-18's in the original, does not form a stable bar despite a similar inner baryon dominance. The obvious difference between the two scenarios is the difference in the magnitude of the merger, with the rerun's being only 25% as massive, suggesting that Auriga 18 did indeed require the increased tidal forces of a more significant GES-like merger to form its bar at this earlier time.

3.3.1.3 The wider Auriga simulations

In this section, I examine the connection between GES-like mergers and bar formation in the context of the larger sample of Auriga simulations. In particular, I highlight the subsample of simulations which Fattahi et al. (2019) identified to contain a population of radially biased stars in their stellar halos at $z = 0$. These populations are found using a Gaussian decomposition of the azimuthal versus radial velocity space of the stellar halo, where halos are determined to be Milky Way-like if the largest component of this decomposition has anisotropy parameter $\beta > 0.8$. This mimics the signature of GES which is observed in the Milky Way at present times. In Fig. 3.8 I plot the bar formation times against the merger times of the 9 out of 10 such selected galaxies which form bars before $z = 0$, including Auriga 18. I also show histograms of the bar formation times of galaxies with/without GES analogues in the right panel. One sees that the galaxies selected loosely fall into two groups: half of the 10 galaxies form bars within 1 Gyr of their GES-like mergers, and the other half (including Auriga 15 which does not form a bar before $z = 0$) do not form bars until over 3 Gyr after their own mergers. No galaxies

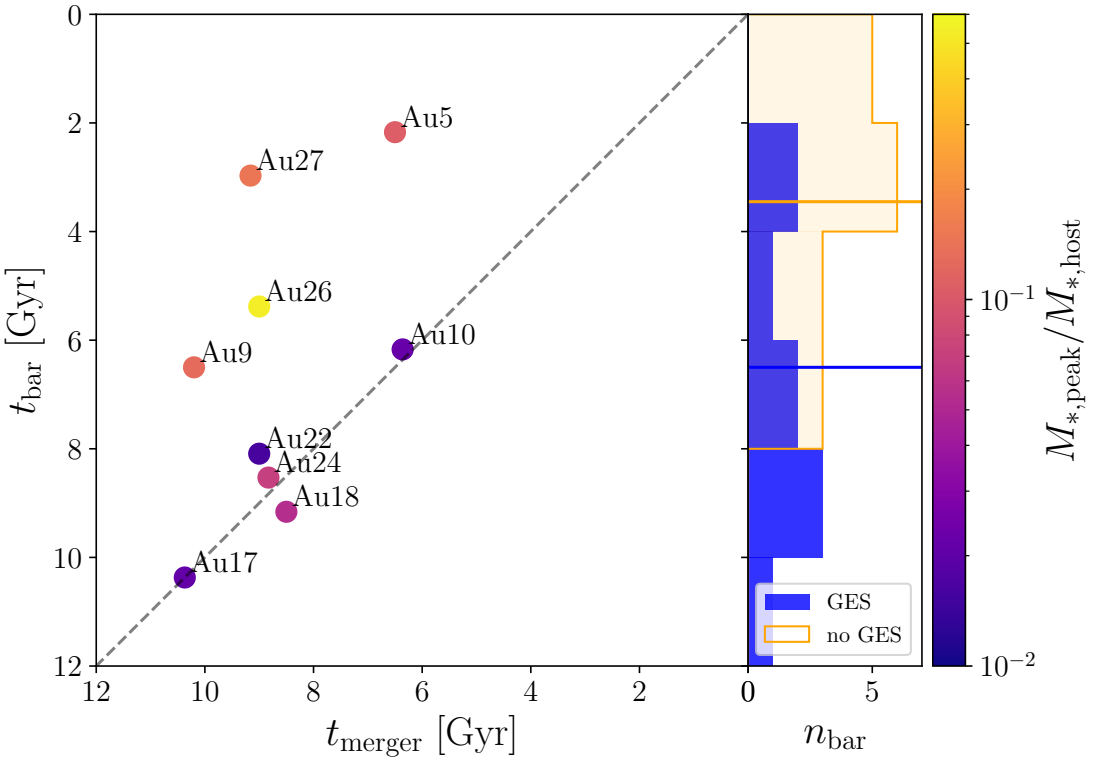


FIGURE 3.8: The relation between merger time (lookback times on the x-axis from Fattahi et al., 2019) and bar formation times (lookback times on the y-axis from Fragkoudi et al., 2025) in the Auriga simulations which experience a GES-like merger. Bar formation is defined in this work as the last time the bar strength passes $A_2 = 0.25$, a threshold at which bars typically become visually identifiable. I show equal times by the dotted grey line. Points are coloured by the peak stellar mass ratio of the merging galaxy to the main halo (Grand et al., 2020), with the most relatively massive mergers in yellow. Auriga 15 is not shown since, although it has a GES-like merger at a lookback time of 5.22 Gyr at a stellar mass ratio of ~ 0.15, it does not form a bar. In the right panel, I show histograms of the bar formation times for those Auriga halos with GES-like mergers and those without, in blue and orange respectively. For each histogram I also show the median bar formation time with a horizontal line.

with GES-like mergers in the sample form bars before the GES merger time (except for Auriga 18 which, as I have already shown, still forms its bar after GES-18's first close pericentre). In addition, the five galaxies that form bars at the same time as their mergers are the galaxies with the lowest stellar mass ratios between their GES analogue at its peak stellar mass and the main galaxy at this same time (see the colour bar of Fig. 3.8). The transition between the two cases occurs at a stellar mass ratio of 10%, leading to a requirement for GES's stellar mass ratio of less than 10% in order to create a bar at a time consistent with estimates from e.g. Grady et al. (2020), Wylie et al. (2022) and Sanders et al. (2024). This mass is consistent with a stellar mass ratio of

6% as found by Helmi et al. (2018) and matched by the $5 - 10 \times 10^8 M_\odot$ stellar mass estimate of Deason et al. (2019). Feuillet et al. (2020) find a higher stellar mass of $10^{8.85-9.85} M_\odot$ giving a ratio of 7-17%, whereas Lane et al. (2023) find a lower mass of $1.45 \times 10^8 M_\odot$, implying a 1-2% ratio (these ratios are under the same assumption for the Milky Way's mass as in Helmi et al., 2018). My restriction on the mass ratio required to form a concurrent bar is consistent with even the extremities of stellar masses found for GES. Fragkoudi et al. (2020) also gives an upper limit on GES' stellar mass ratio regardless of the bar formation time, requiring $< 5\%$ in order to reproduce the rotational velocities of metal-poor stars observed from GES in the Milky Way. This paper is likely to have similar biases to this Chapter due to using the same simulation suite, but both are supported by the relatively low masses from observations.

The Auriga suite as a whole therefore suggests a scenario of bar formation in galaxies with relatively light GES-like mergers. Prior to merging, the galaxy does not contain a bar. When the merger occurs, if the satellite is not too massive, then it induces bar formation in the main galaxy and this bar persists to $z = 0$. If the stellar mass ratio is in fact greater than ~ 0.1, then no bar forms for the next few Gyr, possibly due to the greater disruption to the disc caused by a more massive merger. Importantly, Auriga 17 and Auriga 18 fall into the category of smaller mergers which form bars almost immediately. Since these are the Auriga simulations most similar to the Milky Way in their bulge and inner halo chemokinematics, this furthers the evidence for a link between GES and the Milky Way's bar.

In the right panel of Fig. 3.8, I show histograms for the bar formation times of these nine GES-like galaxies and for the other 17 bar-forming Auriga halos that do not contain a GES analogue. Not only do the galaxies with a GES-like merger tend to form bars earlier, shown by their median bar formation time being ~ 3 Gyr earlier than those without such mergers, but the four oldest bars in the whole suite of Auriga simulations are formed immediately following a GES-like merger. This suggests that bars older than 8 Gyr in particular may be very strongly linked to mergers with similar properties to GES. If the Milky Way's bar formed consistent with the older estimates for its age, this would suggest a causal link of GES triggering its bar formation even based on trends alone. It is, however, worth noting that Rosas-Guevara et al. (2020) and Khoperskov et al. (2024)

both find in cosmological simulations that strong bars at $z = 0$ tend to be correlated with earlier disc formation. Therefore, since early GES-like mergers also require an early disc, the earliest bars in Auriga may be a result of early discs in combination with their GES-like mergers. The Milky Way itself has an early forming disc (Mackereth et al., 2019) in addition to its GES merger event, making it consistent with this scenario.

3.3.2 GES and the growth of the Milky Way's disc

Aside from their bars, Auriga 18 and my rerun produce very different galaxies by redshift 0 as a result of the presence/absence of GES-18. As such, these shed light on the possible galaxy-wide impact a GES-like merger can have on a galaxy with an otherwise quiet merger history, including our own Milky Way.

As shown in Fig. 3.7, from 8 Gyr ago to the present, Auriga 18's disc grows consistently, while the rerun's disc stagnates and stops growing in extent after a lookback time of 7 Gyr. Even though GES-18 brings in a significant amount of gas to the main halo, the figure's second panel shows that the stellar mass of both discs are almost equal by the end of the simulation. Thus, it is unlikely that a mass difference is enough to account for the difference in disc morphology.

When GES-18 merges with Auriga 18, it also imparts a large amount of angular momentum to the galaxy. Fig. 3.9 illustrates the evolution until 3 Gyr ago of angular momentum in the original simulation (left) and the rerun (right). The top panels show the angle separating the stars' spin axis and the gas' spin axis for gas within the inner 50 kpc and the wider halo. The second panel gives the magnitude of angular momentum associated with each type of matter and with GES-18 and both versions of Auriga 18 as a whole. The third panel shows the mass of gas within spheres of different radii and the final panel shows the specific angular momentum of the gas within the same spheres.

The angular momentum imparted by GES-18 is of a similar magnitude to the pre-existing angular momentum of the main halo and, as shown in the second left panel of Fig. 3.9, an order of magnitude greater than the angular momentum in the inner disc-forming regions. Rather than increasing the angular momentum of the main halo, the immediate

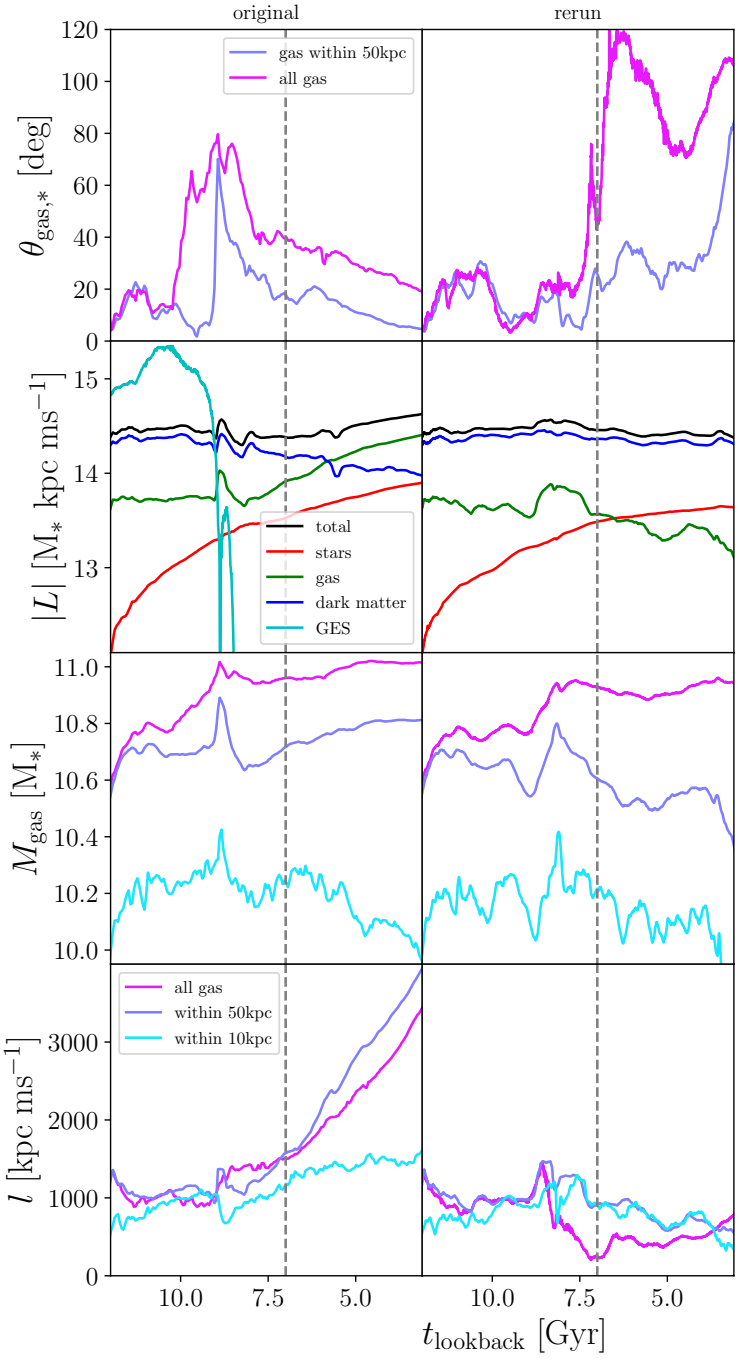


FIGURE 3.9: Details of the evolution of angular momentum in the original (left panels) and the rerun (right panels) of Auriga 18 from 12 – 3 Gyr lookback time. The grey dashed line shows the time at which the extent of the disc in the rerun diverges from that of the original. Top: The angle in degrees between the stars' and gas' angular momentum vectors within 50 kpc of the galaxy's centre (blue) and the same angle but taking all gas in the main halo (pink). Second: The magnitude of angular momentum of stars, gas, dark matter, and the total vector, all within 50kpc. For the original, I also plot in cyan the angular momentum of GES-18's bulk motion around the main halo until it merges in the tree. Third: The mass of all gas in the main halo and contained within spheres of 50 kpc and 10 kpc. Bottom: The specific angular momentum of the gas in the main halo and for the same spheres as above.

effect of this is a change in its axis due to GES-18 approaching at an angle of $\sim 70°$ to the stellar disc. The stellar disc's orientation is shifted by $\sim 65°$ between lookback times of 9 Gyr and 8 Gyr. This change in orientation is matched in the gas component too, with the angle between the stellar disc and the gas at all radii returning to near-alignment after the initial perturbation in the top-left panel. After the merger, the angular momentum of the gas increases due to accretion of gas from the outer regions of the halo and beyond. The gas' specific angular momentum sees a dramatic increase outside of 10 kpc in the lower-left panel, allowing the stellar disc to be built outwards by this gas.

Without GES-18, the inner 50 kpc of the rerun's main halo, including the stellar disc, do not experience such a change in orientation. There is, however, a change in the angular momentum of the outer regions at ~ 7 Gyr ago as the surrounding matter forces the vector to almost the same direction as GES-18 did in the original. This results in a stellar disc and inner region of gas which are completely misaligned with the outer gas' rotation as shown in the top-right panel of Fig. 3.9. In addition to star formation outpacing gas accretion during this time, the newly accreted gas cannot increase the angular momentum of the inner gas due to the misalignment, resulting in a low specific angular momentum (bottom-right panel) and a decreasing total angular momentum (second right panel). As such, the disc does not increase its extent and halts its growth.

This mechanism is responsible for the stagnating disc extent in the rerun for lookback times of $7 - 4$ Gyr. For later times than this, another effect takes over. At 4 Gyr ago, a starburst triggered by interaction with a smaller galaxy almost fully depletes the gas in the rerun. This allows the still accreting gas from the misaligned outer regions to form a new disc of gas in its own orientation. For the last 2 Gyr of the simulation, this forms a young polar disc in addition to the main older disc which has ceased star formation. The polar disc's misalignment and the older disc's quenching lead to no further growth of the galaxy's extent, continuing the trend begun at 7 Gyr.

While the development of the polar disc is a relatively indirect effect of removing GES-18, being dependent on a later interaction, the initial impact of the realignment is critical to Auriga 18's development. If the Milky Way's own GES merged in a similar way, then a similarly large impact may have been made on the Milky Way and be responsible for

the entire structure of the galaxy we live in today. We already expect GES to have had a profound impact on the Milky Way's structure. Haywood et al. (2018), Di Matteo et al. (2019), Belokurov et al. (2020) and Grand et al. (2020) find that the thick disc and non-rotating 'Splash' component are the direct result of an early merger, most likely GES, and are made of both the kinematically heated remnants of the Milky Way's original disc and the stars formed by the gas accreted with GES. Using the Auriga simulations, Grand et al. (2018) and Grand et al. (2020) then suggest that the thin disc formed from later gas accretion after the end of the merger event. This is consistent with the process described here, with the added possibility that the thin disc's formation may have been out of plane with the early disc if GES did not alter the orientation of what became the thick disc.

3.4 Conclusions

In this Chapter I aimed to explore the relation between the last significant merger of the Milky Way, the Gaia Enceladus/Sausage, and the formation of the Milky Way's bar. To this aim, I used a cosmological zoom-in simulation of a Milky Way-like analogue from the Auriga suite, halo 18 (Auriga 18), to examine in detail the time of bar formation, and the effects of the concurrent GES-like merger on the host galaxy. To further compare these effects, I ran a controlled cosmological zoom-in simulation using initial conditions of the Auriga 18 simulation at $z = 4$ but with the GES-like halo's progenitors removed. The main halos of the two simulations are near-identical up until the GES-like merger event. In the rerun, there is no GES-like merger, leaving only a more minor merger event (less massive by a factor of 4) at 8.2 Gyr rather than the original's earlier lookback time of 8.9 Gyr.

My conclusions are as follows:

- I find from the original simulation, that the GES analogue creates large tidal forces in the host galaxy on its first pericentre. These lead to a perturbation in the bar-like A_2 Fourier mode in the outer regions, which propagates inwards to form a bar.

Simultaneously, the gas already present in the host galaxy migrates inwards to induce a burst of star formation in the inner regions of the disc, adding mass to the thick disc and contributing to the baryon-dominance of the disc.

- In my controlled rerun simulation, these effects are significantly muted without the influence of the main GES-like merger. The later low-mass merger is only able to induce a fluctuating A_2 perturbation which fades after $1-2$ Gyr. In total, the rerun's bar formation is delayed by over 2 Gyr, and appears to form secularly rather than by the mechanism described for the original.

- Taken together, this leads me to conclude that the bar formation in Auriga 18 is triggered due to the tidal effects of its merger with GES-18.

- I also show that GES-18 had a profound impact on the wider disc of Auriga 18, by bringing its angular momentum into alignment with its surroundings and allowing the accretion of new gas to extend the disc. My rerun shows the potential effects of an extremely quiescent merger history like the Milky Way's without a significant final merger to connect the galaxy with its surroundings.

- I explore the connection between bar formation and GES-like mergers in other Auriga halos which experience such mergers, according to Fattahi et al. (2019). I find that the lower mass examples of the mergers which leave a GES-like imprint on the current stellar halo, including Auriga 18, tend to form bars within 1 Gyr of their mergers. These also represent the oldest bars in the full simulation suite.

Auriga 18 is a close analogue to the Milky Way in its accretion history and structure, containing both a last significant merger closely resembling GES and an old bar originating around the same time. As such, I have presented a possible path for the formation of the Milky Way's bar being caused by the GES merger, through tidal interactions and the rapid build-up of mass in the inner galaxy.

Chapter 4

What drives bar rotation? The effect of internal properties and galaxy interactions on bar pattern speeds

This Chapter is structured as follows. Firstly, in Sec. 4.1.1, I present the time evolution of bar pattern speeds in my sample, and subsequently examine how they have been impacted by baryon fraction in Sec. 4.1.2 and from external interactions in Sec. 4.1.3. I discuss the implications and context of these results in Sec. 4.2.1 and how they compare to observations in Sec. 4.2.2. Lastly, I summarise and conclude my results in Sec. 4.3.

4.1 Results

In this section, I use the methods described in Sec. 3.1 to analyse the evolution of the pattern speeds of bars. I begin with a description of the evolutions of the bars over their lifetimes in Sec. 4.1.1, followed by a discussion of how this is affected by the changing composition of the host galaxies in Sec. 4.1.2 and by interactions with external galaxies in Sec. 4.1.3.

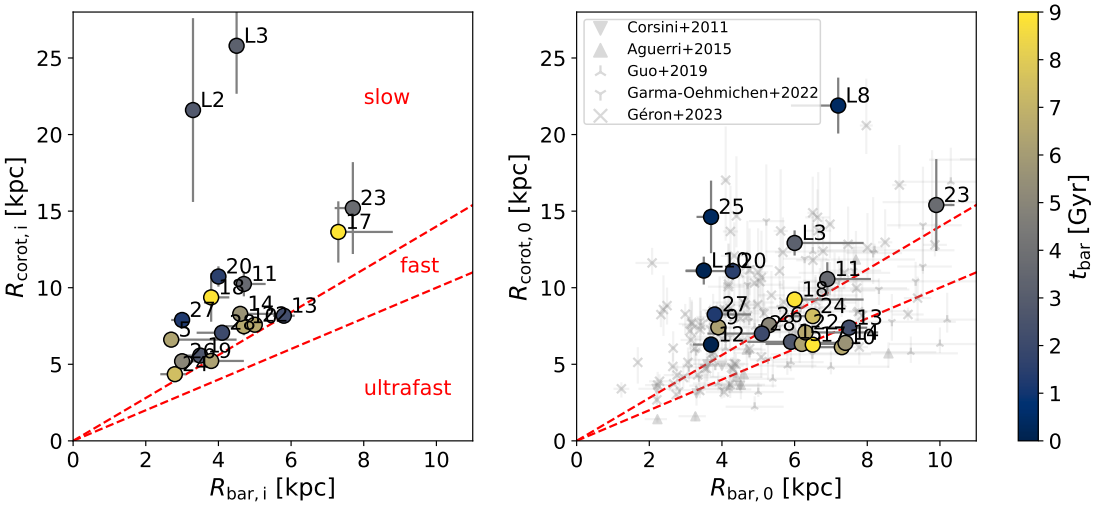


FIGURE 4.1: Bar length and corotation radius for each halo in my barred sample, with uncertainties, at t_i (left panel) and $z = 0$ (right panel). The colour scale indicates the bar formation time in each case. In the right panel, I also plot in grey with uncertainties the observational bar lengths and corotation radii from Corsini (2011) (downwards triangles), Aguerri et al. (2015) (with redshifts from Paturel et al., 2002; García-Benito et al., 2015) (upwards triangles), Guo et al. (2019) (upwards tri-points), Garma-Oehmichen et al. (2022) (downwards tri-points), and Géron et al. (2023) (crosses). For each set of observations, I only include those with uncertainties less than the maximum uncertainty in my simulations (32%) for reliability. The upper and lower dashed red lines correspond to ratios of 1.4 and 1 respectively, with the red labels in the left panel indicating the resulting slow, fast, and ultrafast regions.

4.1.1 Evolution of bar properties

Fig. 4.1 shows the bar length and corotation radius for each of the 22 bar-forming simulations from my sample, at $z = 0$ in the right panel and at the initial time t_i (0.5 Gyr after the bar forms) in the left panel, alongside $z \sim 0$ measurements from the local Universe taken from Corsini (2011), Aguerri et al. (2015), Guo et al. (2019), Garma-Oehmichen et al. (2022) and Géron et al. (2023). Of the 22 simulations, four halos form their bars less than 0.5 Gyr before the end of the simulation, so I only show these values for $z = 0$. There is also one case, Auriga L2, of a bar which is weakened beyond my bar formation threshold before the simulation ends; for this halo I only show initial values of bar properties. I show only one time for these five halos throughout the rest of the Chapter.

One can see that the bars in my sample have lengths in the range of $3.5 - 8$ kpc, with

the exception of Auriga 23 whose bar is length is almost 10 kpc by $z = 0$[1]. These lengths are consistent with measurements of bar lengths from the local Universe in Gadotti (2011), which finds a median of 4.5 kpc, a standard deviation of 1.9 kpc and some values reaching up to 13 kpc. The corotation radii found in my sample tend to be larger, ranging from $\sim$ 5 kpc up to $\sim$ 24 kpc in a handful of cases with very slowly rotating bars. By comparing with the observations in the right panel, one can can see that my sample at $z = 0$ generally overlaps well with the deprojected properties of real bars, albeit with a scarcity of short bars with similarly small corotation radii. It appears that the bars from Auriga have properties compatible with those of the bars in similar mass galaxies in the local Universe, at least in terms of the radii shown here, but may not cover the full range observed.

Using the red dashed lines to indicate $\frac{R_{\rm corot}}{R_{\rm bar}} = \mathscr{R} = 1, 1.4$, one can see that, at initial times, the majority of the bars in my sample are slow (points lying above both lines). However, most of the bars at $z = 0$ are fast or very close to fast (between the two lines) and four are ultra-fast (Auriga 10, Auriga 13, Auriga 14, and Auriga 17 lie below both lines). Since the fast bar regions of Fig. 4.1 are predominantly populated by $z = 0$ bars, the bars appear to have sped up on average. For the largest cluster of points, presumably representing the more typical population of barred galaxies, the points mostly move from left to right; this suggests that the primary driver of the bar speed-up is an increasing bar length, with corotation radius remaining almost constant.

The evolution of the bar pattern speed and rotation rate in Auriga is shown in Fig. 4.2, which shows pattern speed versus bar formation time in the top panel and $\mathscr{R}$ versus bar formation time in the bottom panel. Grey points show the initial $\mathscr{R}_{\rm i}$ and black points the final $\mathscr{R}_0$. From the top panel, one can see that while a significant number of older bars have sped up or slowed down, there is no reliable net change in speed across the population. In contrast, it is clear in the bottom panel that the majority of the bars have a higher value of $\mathscr{R}$ at $t_{\rm i}$, so are initially slower in this measure. At $z = 0$, one can also see the trend that older bars are faster on average in both panels. This trend is most obvious in $\mathscr{R}$ for the bars younger than 2 Gyr, which are almost all – except for Auriga 12 – slower than any of the older bars. The same trend is also apparent, but with a more

[1] Auriga 23 also has an unusual bar since it is the outer bar of a double-barred system.

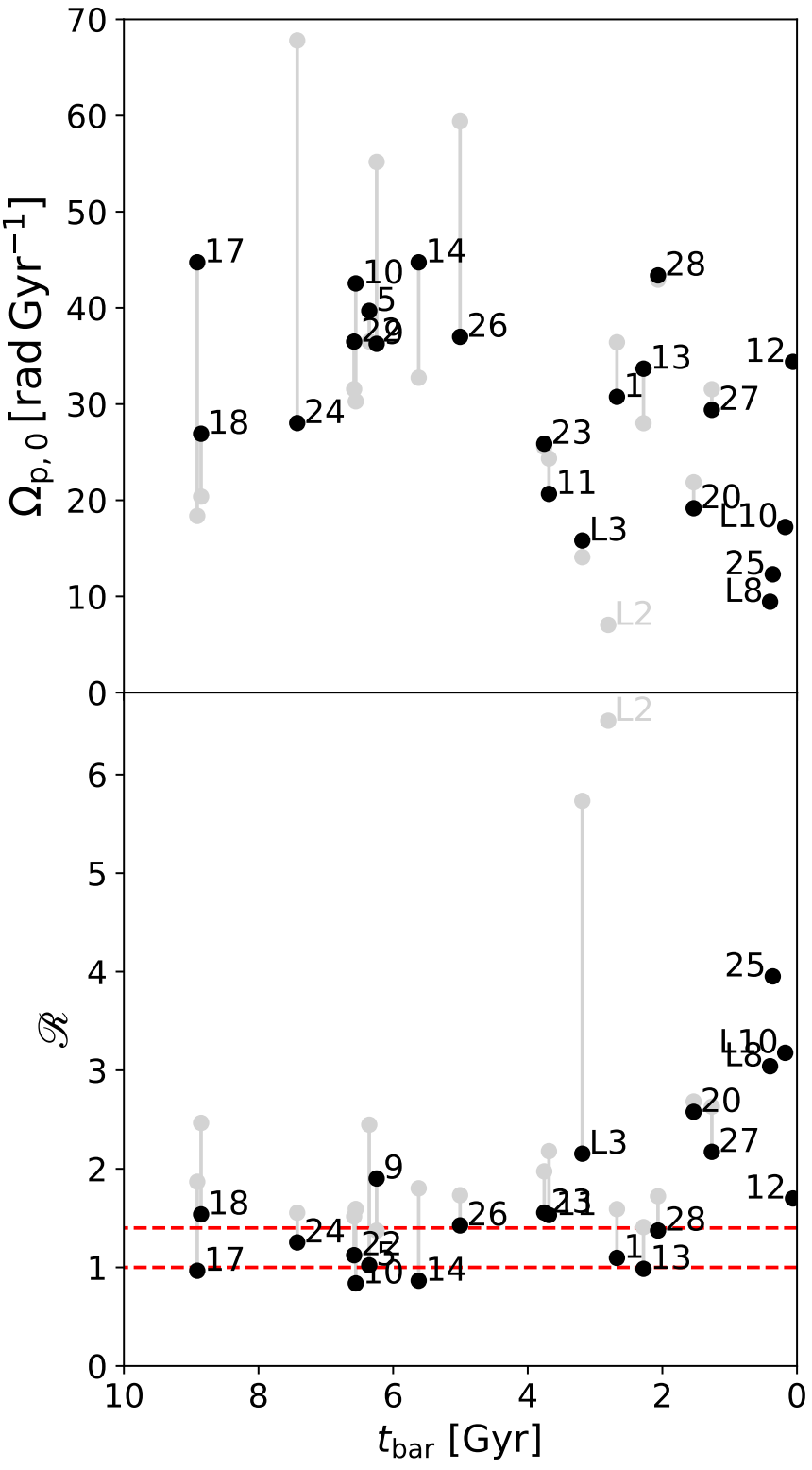


FIGURE 4.2: Top: the relation between bar formation time and pattern speed at $z = 0$, shown as the black points, and at 0.5 Gyr after bar formation, shown as the connected light grey points. Bottom: the same, but for $\mathscr{R}$ instead of pattern speed. The red dashed lines indicate $\mathscr{R} = 1, 1.4$.

gradual slope for bars older than $\gtrsim$ 2 Gyr. The speed-up in the Auriga bars does not appear to be a constant, gradual process, since the relation between change in $\mathscr{R}$ and bar age is relatively weak (see panel (f) in Fig. A.1). Additionally, many of the younger bars are also slow at t_i, which indicates an effect on rotation rate before the bar can age.

In Fig. 4.3, I show the bar pattern speed in the top panel and the normalised rotation rate $\mathscr{R}$ in the bottom panel. In the bottom panel, one can see that stronger bars tend to be faster when using $\mathscr{R}$. This mirrors the trend seen in Fig. 4.2, since age and strength are positively correlated in my sample (see panel (e) in Fig. A.1), but appears stronger here across the whole sample than the trend between $\mathscr{R}_0$ and $t_{\rm bar}$. As seen in the top panel, this relation with bar strength holds when using pattern speed instead of rotation rate, albeit with significantly greater scatter. Stronger bars still tend to be faster, but there is a wide spread especially for the weaker bars, indicating that the clearer trend with $\mathscr{R}$ relies on both pattern speed and bar length.

Put together, I find a typical picture of bar evolution in the Auriga simulations: the bar forms somewhat slow, or very slow if it forms late, but as it evolves over time it becomes stronger and longer, and lowers its rotation rate to become faster. This is perhaps rather surprising, given that we tend to expect bars to slow with time (Weinberg, 1985; Little & Carlberg, 1991; Debattista & Sellwood, 2000; Athanassoula, 2003). In the following sections, I explore the causes of this trend, examining how the internal and external properties affect the rotation rate.

4.1.2 The effect of changes in the host galaxy

Bars do not exist in static systems, instead belonging to host galaxies that have a wide variety of evolving properties. This section examines how the wider galaxy affects the rotation rate, focusing on the mass and radial distributions of the stellar and dark matter components of the galaxies. Sec. 4.1.2.1 explores this at the whole galaxy and halo scales, while Sec. 4.1.2.2 restricts this to the inner few kpc.

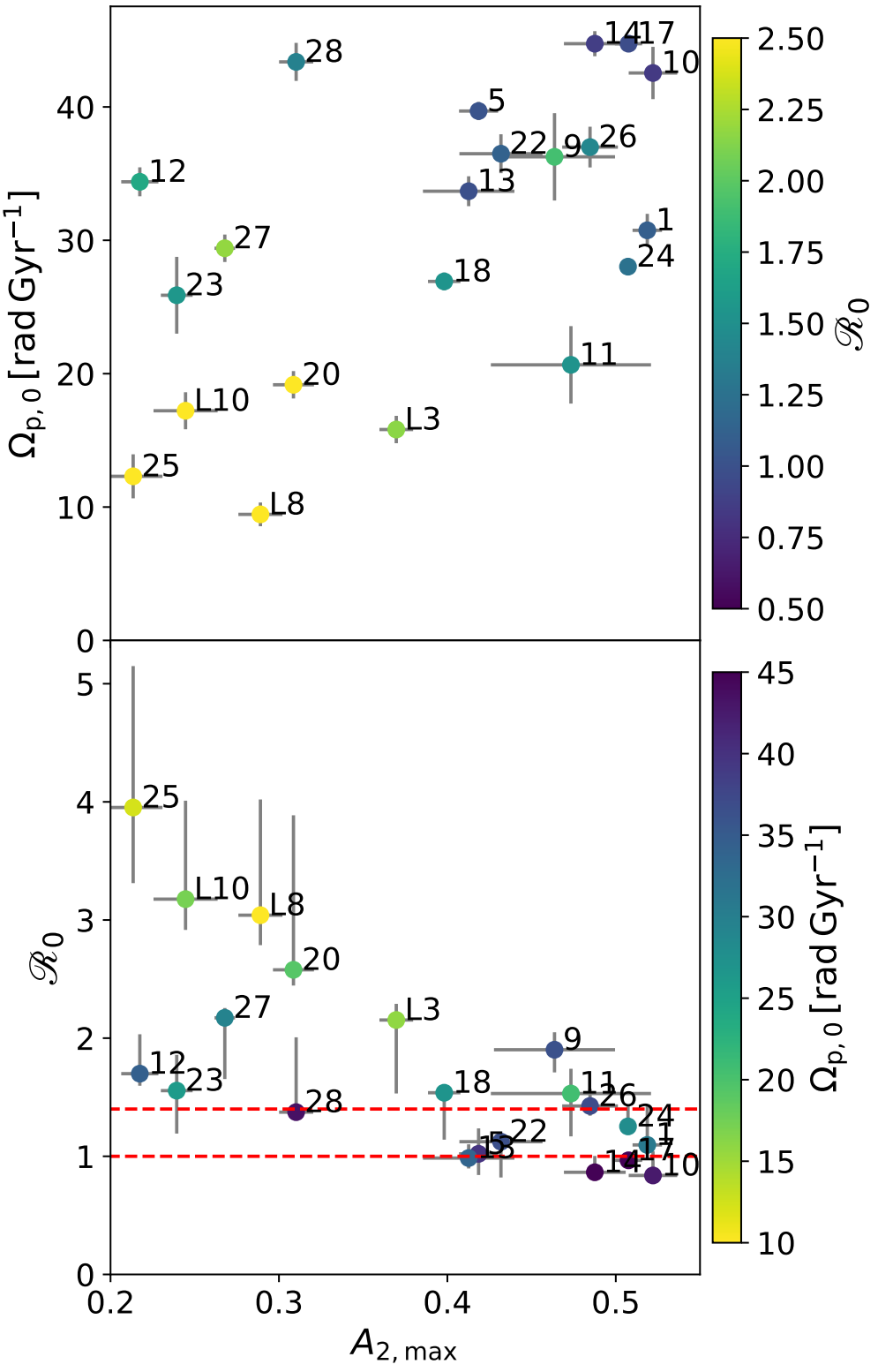


FIGURE 4.3: The dependence at $z = 0$ of bar pattern speed and rotation rate on bar strength. The top panel shows the pattern speed at $z = 0$, $\Omega_{p,0}$, coloured by the rotation rate at $z = 0$, $\mathscr{R}_0$, while the bottom panel shows $\mathscr{R}_0$ on the axis and $\Omega_{p,0}$ in the colour scale. Both have error bars shown. The bottom panel shows red dashed lines indicating $\mathscr{R} = 1, 1.4$.

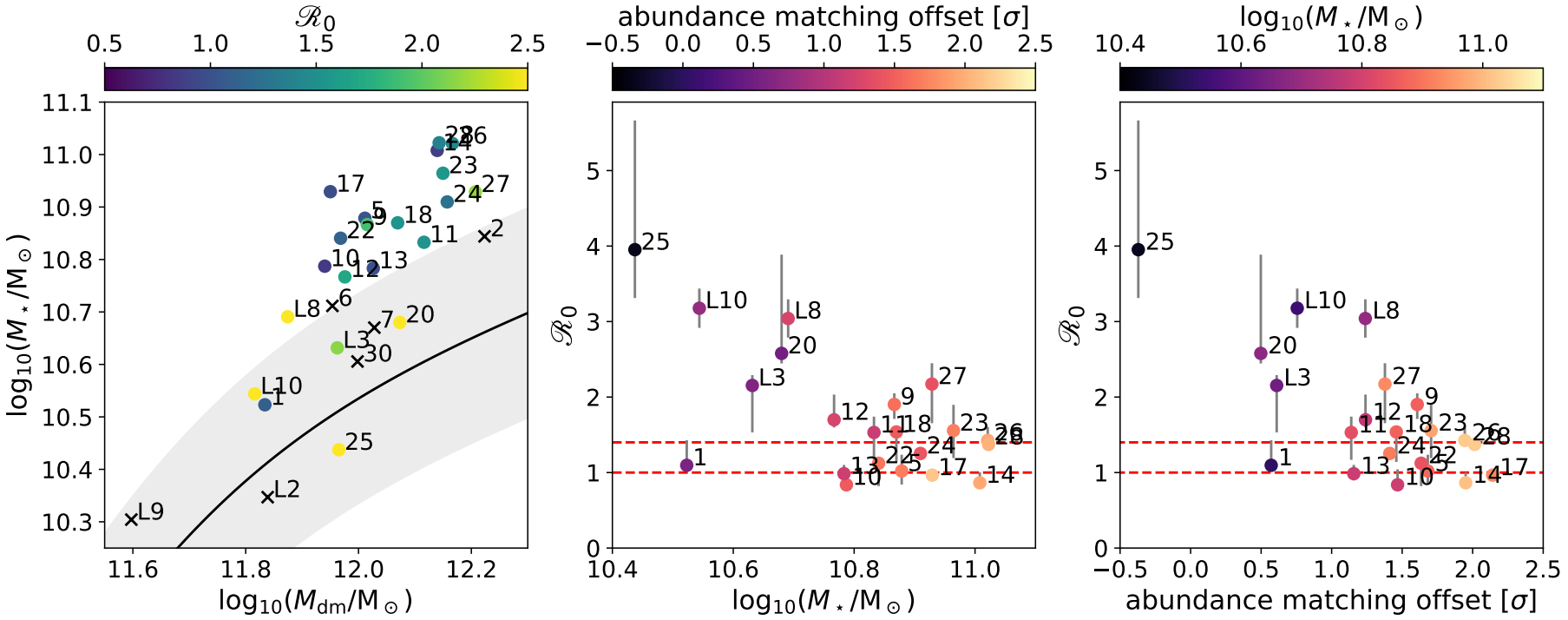


FIGURE 4.4: Left: Final dark matter halo mass compared with final stellar mass for each halo in my sample. The colour scale shows the final value of $\mathscr{R}$ for each bar. Halos which are unbarred at $z = 0$ are marked as black crosses. The black line shows the abundance matching relation from Moster et al. (2013), with the grey shaded region showing the 1σ dispersion at each halo mass. Middle: final $\mathscr{R}$ plotted against final stellar mass, for those halos which are barred at $z = 0$. The colour scale shows the vertical offset of the halo from the abundance matching relation in the left panel, given in units of the σ dispersion at the relevant dark matter mass. Right: final $\mathscr{R}$ plotted against the vertical offset from the abundance matching relation, for those halos which are barred at $z = 0$. The colour scale shows the final stellar masses of the halos. In the two rightmost panels, error bars are shown for $\mathscr{R}_0$ and the red dashed lines, as before, indicate $\mathscr{R} = 1, 1.4$.

4.1.2.1 Global galaxy composition

The left panel of Fig. 4.4 shows the stellar mass-halo mass relation, comparing the masses of the halos in my sample to the semi-empirical abundance matching relation from Moster et al. (2013). I first note that my sample sees a steeper slope than the observational relation, with the barred galaxies in particular lying significantly above the relation at higher masses, in keeping with previous results from the Auriga simulations (see Fragkoudi et al., 2025, for more details). One can also see from the colour scale that the halos in the upper right portion of the figure, with higher stellar masses and a greater offset from the abundance matching relation, tend to host faster bars.

I show $\mathscr{R}$ as a function of stellar mass in the middle panel of Fig. 4.4, where one can see that the lower mass galaxies in my sample tend to host slower bars, with just one fast bar for galaxies with stellar masses below $6 \times 10^{10}\,\mathrm{M}_{\odot}$. This relation may link to the trend in the left panel of more massive galaxies lying further above the abundance matching relation. The right panel explores this, showing the vertical offset from the abundance matching relation (the difference in $\log_{10}(M_{\star}/M_{\odot})$ between a galaxy's stellar mass and the stellar mass predicted by the abundance matching relation at the same halo mass), normalised to the observed 1σ dispersion of the relation. It confirms that, at $z = 0$, faster bars are indeed hosted by halos lying at higher abundance matching offsets. Although there is a large scatter in $\mathscr{R}_0$, this trend appears across the full range of the sample, suggesting it may be a stronger trend compared to the relation between $\mathscr{R}_0$ and stellar mass, which only appears to affect rotation rates in galaxies below $6 \times 10^{10}\,\mathrm{M}_{\odot}$. Indeed, I find Spearman correlation coefficients with $\mathscr{R}_0$ of -0.57 for the abundance matching offset and -0.45 for the stellar mass. As such, the rotation rate appears to be more directly dependent on the relative masses of the galaxy and its dark matter halo than the stellar mass alone.

The trend of increasing bar rotation rate with decreasing stellar mass is an observable prediction of the Auriga physics model within a ΛCDM cosmogony, in particular: how baryons interact with dark matter for different galaxy masses. However, Habibi et al. (2024) find the opposite trend of higher rotation rates with higher stellar mass in the TNG50 simulation (Nelson et al., 2019; Pillepich et al., 2019). This indicates

that while a ΛCDM cosmology does lead to a dependence of rotation rate on stellar mass, it does not necessarily specify the direction of such a relation. Since baryon fraction is not meaningful in cosmology models without dark matter – e.g. Modified Newtonian Dynamics (MOND Milgrom, 1983), Modified Gravity (MOG Moffat, 2006), or Non-Local Gravity (NLG Hehl & Mashhoon, 2009) – we would not expect to see a dependence of rotation rate on galaxy mass in such models. Indeed, Nagesh et al. (2023) employ MOND to simulate three barred galaxies with masses $10^9 - 10^{11}$ $M_\odot$ and find that the bar in each case is similarly fast ($\mathscr{R} \sim 1.6$)[2], confirming the lack of mass dependence for bar rotation speed within these frameworks without dark matter.

4.1.2.2 Baryon dominance in the inner regions

Bars are structures of the inner few kpc of the stellar disc, and as such their formation and evolution is especially closely tied to the properties of the host galaxy in its inner region, in particular the relative properties of the stars and the dark matter. I quantify the relative contributions of stars and dark matter to the mass of the inner galaxy using the ratio of the circular velocity due to the stellar component within 1 effective radius of the centre of the halo, to the circular velocity from the total mass within the same region. I refer to this as the baryon dominance. The effective radius for the simulated galaxies in my sample is in the region of $2 - 10$ kpc, matching the range of bar lengths as shown in Fig. 4.1. This definition of baryon dominance therefore describes the prevalence of stars compared to dark matter in the inner bar-forming regions.

Fig. 4.5 shows the dependence of $\mathscr{R}$ at initial (left panel) and final (right panel) times on the baryon dominance of the host galaxy at the same time. One can clearly see, at both bar formation and the end of the simulation, that rotation rate is strongly dependent on the baryon dominance of its host galaxy at the corresponding times. Focusing on the left panel, one can see that all but one bar are slow initially, although the faster bars at t_i reside in the more baryon dominated hosts, with a gradual increase in $\mathscr{R}$ as baryon dominance decreases. The colour scale shows that this trend is largely independent of

[2] Roshan (2018), Roshan & Rahvar (2019), and Ghafourian et al. (2020) show that simulations using MOG and NLG also produce bars with lower rotation rates than those using dark matter, however, these studies do not investigate any mass dependence.

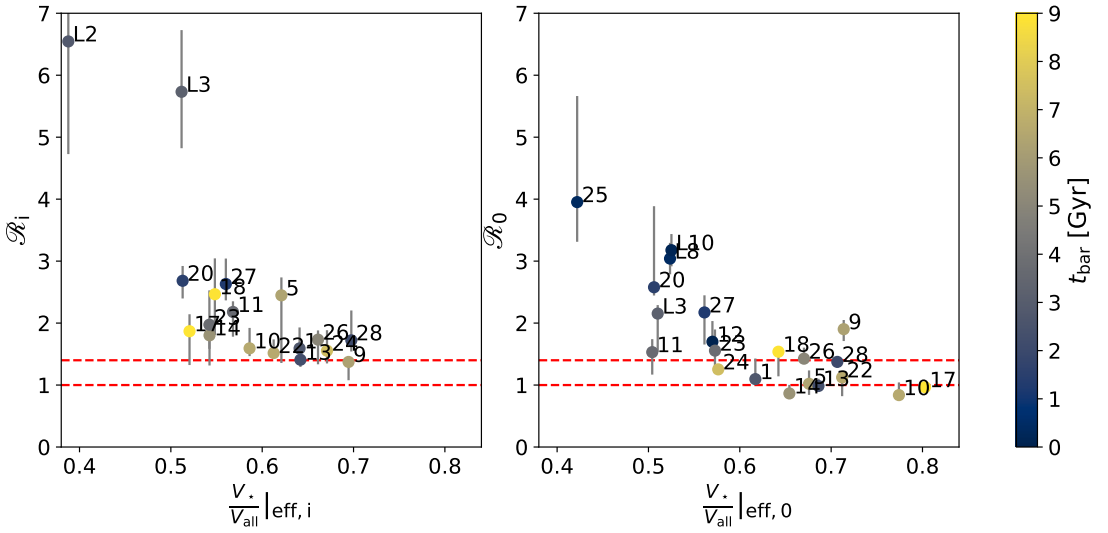


FIGURE 4.5: The relation between baryon dominance (quantified as the ratio of circular velocities for stars and for all matter, evaluated at the effective radius) and $\mathscr{R}$. Both axes are shown for $z = 0$ on the right and for 0.5 Gyr after bar formation on the left, coloured by the bar formation time. Error bars are shown for $\mathscr{R}$ in both panels. The red dashed lines indicate $\mathscr{R} = 1, 1.4$ in both panels.

the bar formation time. In the right panel, at $z = 0$, one can see the same trend of faster bars tending to be hosted by more baryon dominated galaxies, but now with a high proportion of fast bars for $\frac{V_\star}{V_{all}}|_{eff,0} > 0.6$. The change is largely due to the older bars, whose galaxies become more baryon dominated after their bars form and whose bars correspondingly decrease their rotation rates to occupy the fast regime. For example, Auriga 17, the oldest bar in the sample, begins as a slow bar in the fourth least baryon dominated halo in the left panel of Fig. 4.5, but by $z = 0$ is the most baryon dominated galaxy in the right panel, and hosts an ultra-fast bar.

In Fig. 4.6 I show how each halo changes from t_i to $z = 0$, with fractional changes in $\mathscr{R}$ and baryon dominance. There appears to be a trend present, with significant scatter: galaxies that have experienced the largest increase in baryon dominance generally host bars that have sped up more. Additionally, the single bar that has instead slowed down experienced just a 5% increase in baryon dominance over its 6 Gyr lifetime, far less than many of the other halos. The colour scale indicates some weak correlation with the bar formation time – here the time over which the change is measured – with the oldest bars seeing some of the largest changes, speeding up while their host galaxies become more baryon dominated.

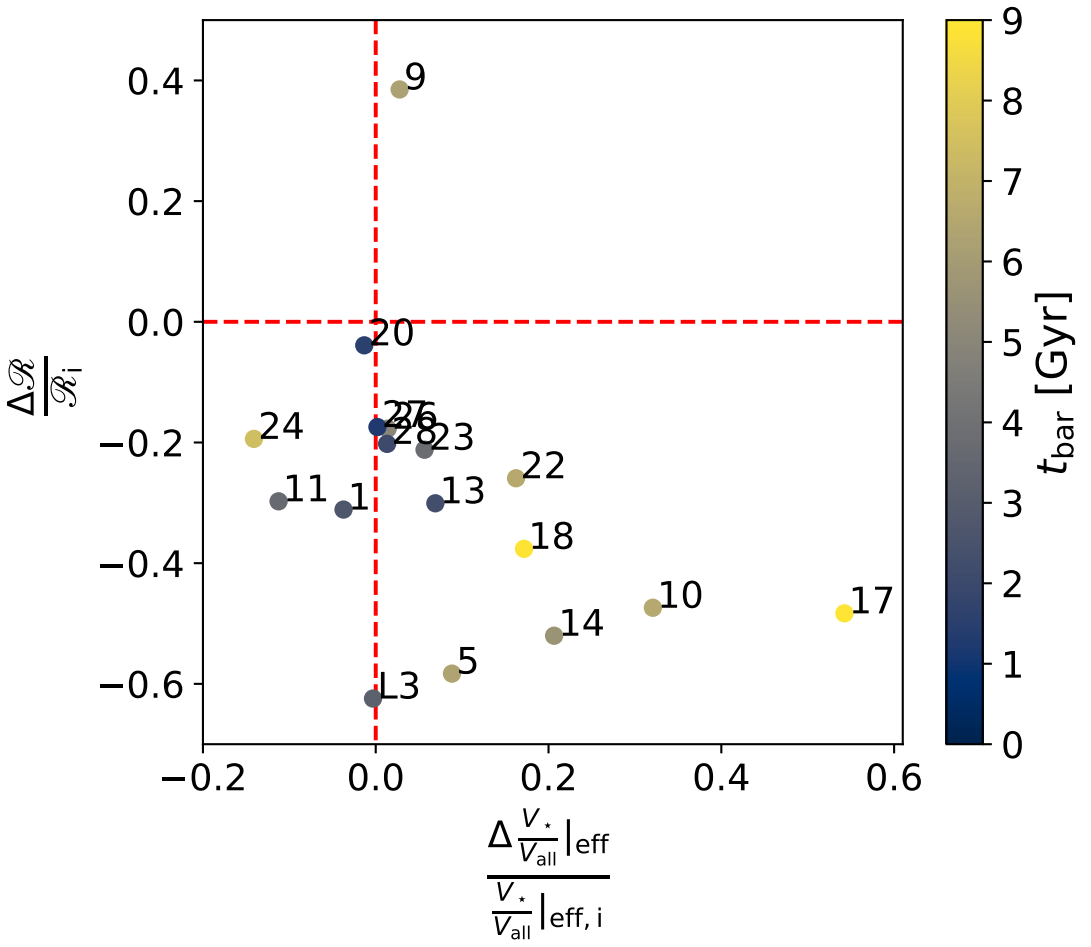


FIGURE 4.6: The fractional change in $\mathscr{R}$ from bar formation to $z = 0$ shown against the fractional change in baryon dominance (quantified as in Fig. 4.5) over the same time period. The colour scale shows the lookback time to bar formation. The red dashed lines indicate no change in $\mathscr{R}$ (horizontal) and baryon dominance (vertical). Bars below the horiztonal line have sped up and halos to the right of the vertical line have increased their baryon dominance.

4.1.3 The effect of galaxy interactions

Within a cosmological setting, galaxies evolve not just by secular processes, but also by interactions with other galaxies. These interactions can induce torques, and thus change the angular momentum of discs and their internal structures, such as bars, and therefore may affect their properties. I parametrise here the strength of such interactions by the Elmegreen parameter as outlined in Sec. 2.2.2, and focus on the strongest interactions in two time intervals to describe their potential impact on the rotation rates of bars. I am firstly interested in the time around bar formation, since this affects the conditions under which the bar first appears and has the potential to set its behaviour early in its

evolution. Following this, I investigate the continued effect of interactions on the rotation rate during the lifetime of the bar, which may alter the bar as it evolves up to the end of the simulation.

Fig. 4.7 shows the dependence of rotation rate on the logarithm of the maximum interaction strength around the time of bar formation (the 1.5 Gyr immediately preceding my $t_{\rm i}$). I denote this as $\log_{10} S_{\rm form}$. The top panel of Fig. 4.7 shows the initial $\mathscr{R}_{\rm i}$ and final $\mathscr{R}_0$ in grey and black points, respectively. Despite a wide spread, there is a weak trend in $\mathscr{R}_0$ where the fastest bars by $z = 0$ formed alongside some of the strongest interactions. I note that the bars in Auriga 20, Auriga 25, and Auriga L10, while contradicting this trend, are each younger than 2 Gyr – this may be the reason for their high rotation rates given the trend in Fig. 4.2. There is, however, no discernable trend in their initial rotation rates. This is unexpected, since interactions around the bar formation time would intuitively be more likely to affect bar properties around the same time. Instead, there is little to no effect at the initial time itself, with a weak trend only arising at later times. I note that there is a bias present: stronger interactions are more likely to occur at earlier times in the simulation. This results in earlier forming bars being more likely to form amid strong interactions, thereby having larger values of $\log_{10} S_{\rm form}$, and, as I showed in Sec. 4.1.1, earlier forming bars are also faster on average. The interdependence of $\log_{10} S_{\rm form}$ and $t_{\rm bar}$ can be seen in the thick-bordered panel (c) in Fig. A.1.

My finding that older bars experience stronger interactions at their time of formation relative to younger bars contrasts with results from the TNG50 simulation, presented in Frosst et al. (2026). These authors argue that secularly formed bars are older, because they find: i) that older bars form with higher baryon dominance and; ii) a weak anti-correlation between baryon dominance and interaction strength around the bar formation time (note that they use different formulations of these quantities than those used here). My results are consistent with the former (see panel (d) in Fig. A.1), but not with the latter: there is no relation between baryon dominance and $S_{\rm form}$ (see panel (b) in Fig. A.1), which accounts for the differing results between simulations.

The bottom panel of Fig. 4.7 shows the fractional change in rotation rate across the lifetime of the bar, $\frac{\Delta\mathscr{R}}{\mathscr{R}_{\rm i}}$. One can see a somewhat stronger trend with $\log_{10} S_{\rm form}$ when

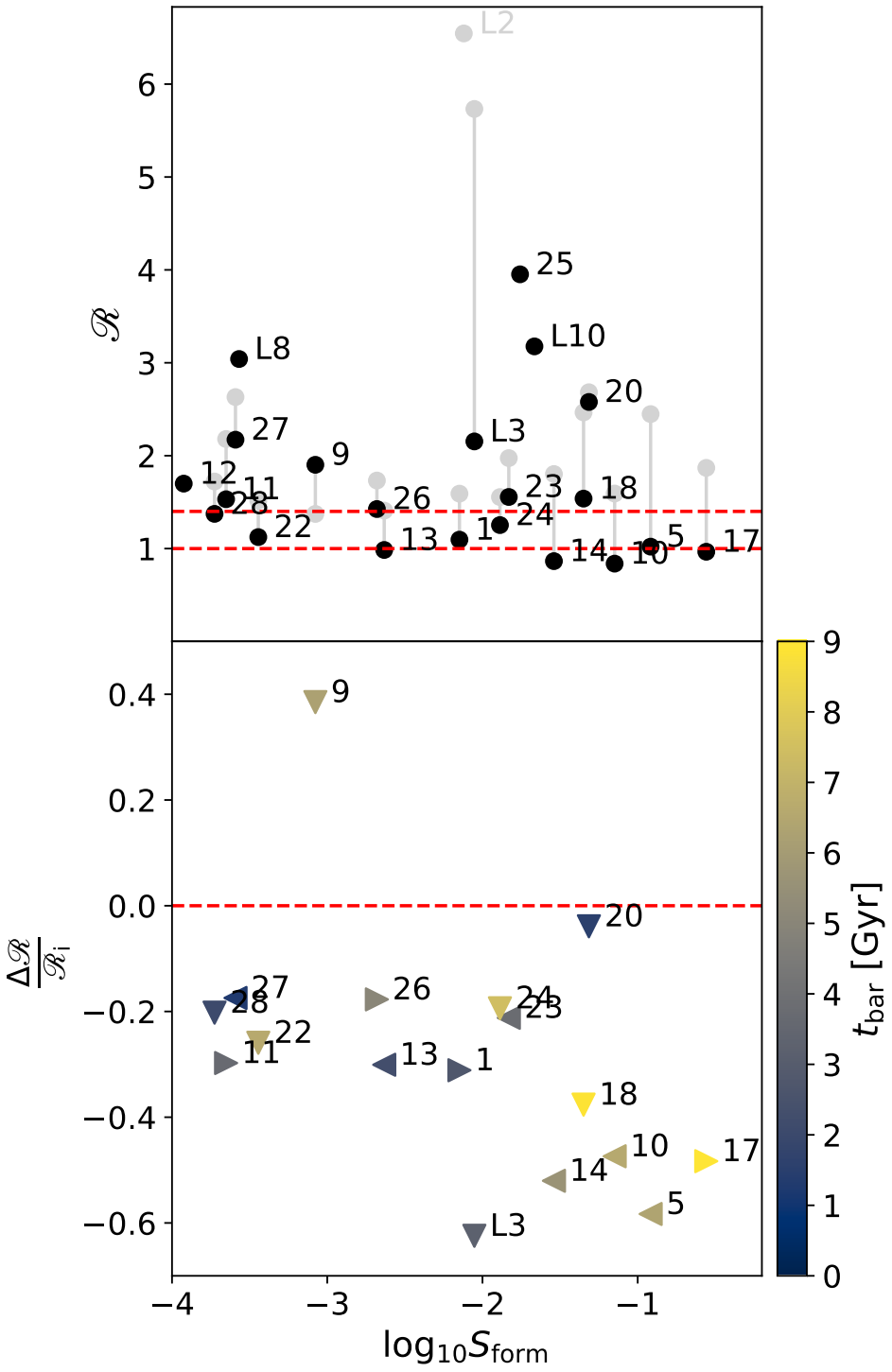


FIGURE 4.7: The relation between $\mathscr{R}$ and the maximum Elmegreen parameter (S) for any interaction from 1 Gyr before to 0.5 Gyr after bar formation. The top panel shows $\mathscr{R}$ at $z = 0$ (black points) and at 0.5 Gyr after bar formation (grey points connected by the grey lines). The red dashed lines indicate $\mathscr{R} = 1, 1.4$. The bottom panel shows the fractional change in $\mathscr{R}$ between these two times. The colour scale shows the bar formation time for each halo, and the left/down/right pointing triangles indicate retrograde/polar/prograde oriented interactions respectively. The red dashed line in the lower panel indicates no change in $\mathscr{R}$; bars below this line have sped up.

looking at change rather than instantaneous $\mathscr{R}$, although the scatter is still significant: bars forming alongside stronger interactions tend to have sped up more by $z = 0$ than those which were formed in relatively isolated galaxies. This is not entirely explained by the aforementioned bias from bar formation times, as can be seen by the colour scale (e.g. Auriga 9 and Auriga 22 which have not sped up by more than 25% and have not had strong interactions, but are relatively old bars). In this panel, I also show the orientation of the interaction relative to the spin of the disc by the shape of the points: right-pointing triangles indicate prograde interactions where the orbit of the perturber is aligned with the rotation of the disc to within 60°; left-pointing triangles indicate retrograde interactions where the orbit of the perturber is aligned opposite to the rotation of the disc to within 60°; upwards-pointing triangles indicate polar interactions where the orbit of the perturber is intermediate to these two cases, i.e. approaching at or close to perpendicular to the disc plane. There seems to be little coherent effect from the orientation of the interactions, despite expectations that prograde fly-by interactions should have greater effects on the galaxy (Toomre & Toomre, 1972; D'Onghia et al., 2010; Lang et al., 2014; Lokas, 2018).

There is also a strong relation between $\log_{10} S_{\rm form}$ and the fractional change in baryon dominance (see panel (a) in Fig. A.1) which suggests some interdependency between these parameters since both show a similar trend with $\frac{\Delta\mathscr{R}}{\mathscr{R}_{\rm i}}$. It is possible that a strong interaction around the time of bar formation produces an inflow of baryonic material, increasing the baryon dominance of the inner regions of the galaxy over a timescale of a few Gyr. It is unclear which relation is the genuine causation – whether increase in baryon dominance and maximum interaction strength around bar formation are mechanically linked, or they simply both produce a similar speeding up of the rotation rate.

Fig. 4.8 shows the highest Elmegreen parameter for any interaction since 0.5 Gyr after bar formation, covering the lifetime of the bar up to the end of the simulation. I denote this maximum as $\log_{10} S_{\rm bl}$, using 'bl' to denote the bar lifetime rather than 'form' which denoted the bar formation time. From the top panel one can see little correlation between $\mathscr{R}$ and $\log_{10} S_{\rm bl}$ at either of these times. However, in the bottom panel one can see that the bars that have experienced stronger galaxy interactions speed up more. This correlation is quite weak, but does notably account for the significant decreases in rotation rates of

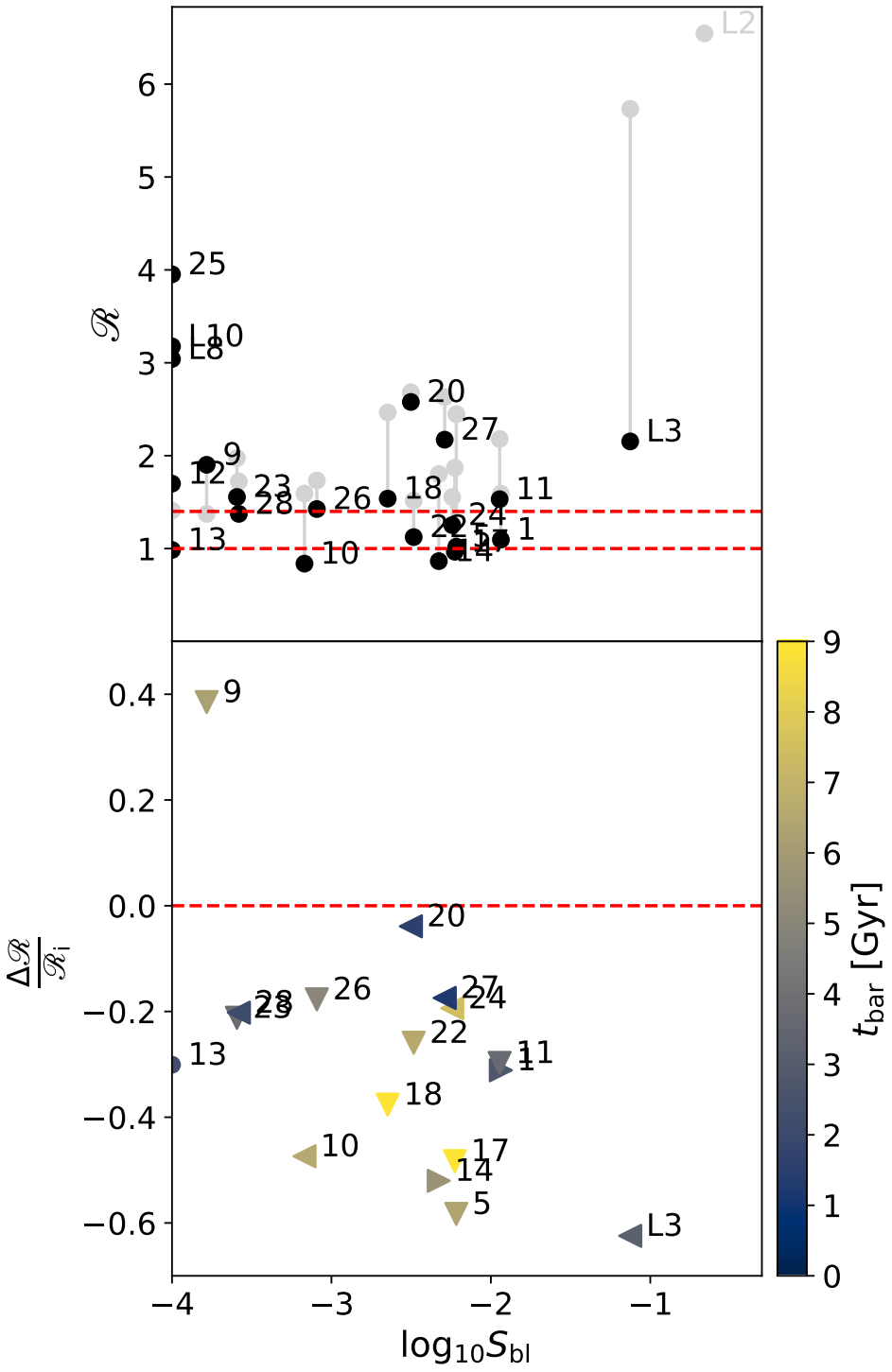


FIGURE 4.8: The relation between $\mathscr{R}$ and the maximum Elmegreen parameter (S) for any interaction following 0.5 Gyr after bar formation. The top panel shows $\mathscr{R}$ at $z = 0$ (black points) and at t_i (grey points connected by the grey lines). The red dashed lines indicate $\mathscr{R} = 1, 1.4$. The bottom panel shows the fractional change in $\mathscr{R}$ between these two times. The colour scale shows the bar formation time for each halo, and the left/down/right pointing triangles indicate retrograde/polar/prograde oriented interactions, respectively. The red dashed line in the lower panel indicates no change in $\mathscr{R}$; bars below this line have sped up.

Auriga L3, which is unusual in Fig. 4.6, having not increased in baryon dominance, but here can be seen to have experienced the strongest interaction since bar formation of the entire sample with surviving bars at $z = 0$. The pattern speed in Auriga L3 increases steadily following its interaction until the end of the simulation, dramatically decreasing its large corotation radius and thus decreasing $\mathscr{R}$.

Together with the results shown in Sec. 4.1.1 and Sec. 4.1.2, interactions with external galaxies seem to have only a secondary effect on the rotation rates of their bars, with weaker correlations than those seen with bar strength and with baryon dominance.

4.2 Discussion

I first discuss the physical processes that may lie behind the low, decreasing bar rotation rates in Auriga, given the correlations with baryon dominance and interaction strength presented above, and how these compare to the literature. I then discuss the extent to which the trends with bar rotation rate above are supported by observational studies, in particular those found with both bar strength and galaxy stellar mass.

4.2.1 Decreasing rotation rates

The prevalent mode of evolution for the bars in the Auriga suite appears to be lengthening without significant slowing of pattern speed (most speed up and only three slow by more than 20%), resulting in bars which speed up in rotation rate through their lifetimes (see Fig. 4.2). While an increasing bar length is expected for bars evolving secularly, the expectation from theory and tailored simulations is that their pattern speeds, and therefore rotation rates, will slow down, primarily due to dynamical friction from the dark matter halo (Weinberg, 1985; Little & Carlberg, 1991; Debattista & Sellwood, 2000; Athanassoula, 2003). In some cases, the increase in corotation radius from a slowing pattern speed is not sufficient to outpace the increase in bar length, resulting in the bar maintaining a fast rotation rate, i.e., low $\mathscr{R}$ (e.g. O'Neill & Dubinski, 2003; Martinez-Valpuesta et al., 2006). Additionally, Sellwood & Debattista (2006) find that the presence

of a gravitational perturbation which increases the pattern speed briefly – such as an interaction with an external galaxy – can halt the slow-down from dynamical friction for a few Gyr. However, they also show that this state of 'metastability' is sensitive to further perturbations, which are frequent in a cosmological setting. Therefore, the metastable state is unlikely to last long in reality, allowing slow-down from dynamical friction to resume.

In this study, I do not seem to find dynamical friction acting as a persistent, gradual mechanism, which would slow down bars on long timescales. In contrast, I find that dynamical friction is likely acting on much shorter timescales, since Fig. 4.4 and Fig. 4.5 show that bar rotation rates are mainly dependent on the ratio of the stellar to dark matter (with more baryon dominated galaxies hosting faster bars) at formation time, as well as at subsequent times. This trend is established by $t_{\rm i}$ (just 0.5 Gyr after the bar forms), which is a much shorter timescale than the 5 – 10 Gyr found in Little & Carlberg (1991), Debattista & Sellwood (2000), Athanassoula (2003), O'Neill & Dubinski (2003) and Sellwood & Debattista (2006) for dynamical friction, potentially on the same timescale as bar formation. Instead, the correlation of rotation rate and baryon dominance which one sees in my sample may suggest the fast-acting dynamical friction originally described in Weinberg (1985) which acts over a few bar rotation times (roughly 0.1 – 1 Gyr here) for bars that form fast.

In addition to acting over a short timescale, dynamical friction is relatively weak in the baryon-dominated systems I explore since bars remain fast and even decrease in rotation rate as they evolve. As mentioned in Sec. 1.3, some studies suggest that there could be mechanisms arising from channelling gas towards the centre of the galaxy that can speed the bar up (Bournaud et al., 2005; Berentzen et al., 2007; Romano-Díaz et al., 2008; Villa-Vargas et al., 2010; Athanassoula, 2014; Beane et al., 2023). Even if this effect is not enough to counter dynamical friction on its own, Sellwood & Debattista (2006) finds that gas inflows may be able to reliably produce the perturbation in pattern speed required to trigger a metastable state.

Interactions with other galaxies are an unlikely main candidate for speeding up bars in Auriga, since the associated trends in Sec. 4.1.3 are relatively weak, and there is

no evidence for tidal forces during an interaction reliably increasing the pattern speed of a bar, instead showing a mixture of speeding and slowing the bar as in e.g. Gerin et al. (1990), Lokas et al. (2014) and Semczuk et al. (2024). Panel (a) in Fig. A.1 does, however, indicate a correlation between stronger interactions around the time of bar formation and greater changes in baryon dominance between $t_{\rm i}$ and $z = 0$. This correlation may be linked to inflows of gas which could increase the bar rotation rate, or higher rates of gas accretion onto the galaxy which could add angular momentum to the disc and the bar. Both mechanisms require a lasting effect on the radial motion of gas in order to cause a speed-up of the bar over its lifetime, consistently maintaining the influence of the interaction for at least 1 Gyr after its pericentre.

Further clues may come from comparison with other cosmological simulations in which the speeding up of bars seen here are not present. As mentioned in Sec. 1.5.1, most cosmological simulations which form bars tend to produce bars which are too slow, particularly in rotation rate (Algorry et al., 2017; Peschken & Lokas, 2019; Roshan et al., 2021; Habibi et al., 2024; Ansar et al., 2025), potentially as a result of excessive slow-down from dynamical friction (significant slow-down is seen in Algorry et al., 2017; Habibi et al., 2024) or a lack of lengthening through their evolution (Frankel et al., 2022). These studies examine bar rotation rate in five different simulations, which I compare with Auriga in turn.

In Illustris (Vogelsberger et al., 2014), Peschken & Lokas (2019) find a mean bar rotation rate of 5.6 ± 3.8. In EAGLE (Crain et al., 2015; Schaye et al., 2015), Algorry et al. (2017) find rotation rates of $1.4 - 10$ for the strong bars in EAGLE Ref-L100N1504 (the 100 cMpc box run). Additionally, Roshan et al. (2021) find mean rotation rates of $2.4^{+1.1}_{-0.8}$ in EAGLE Ref-L100N1504 and $1.9^{+1.7}_{-0.9}$ in EAGLE Ref-L050N0752 (the 50 cMpc box run). For these two simulation suites, Fragkoudi et al. (2021) find that the higher values of baryon dominance found in Auriga galaxies are the likely reason for its faster bars. Increased baryon dominance in the inner regions of galaxies can significantly reduce the effects of dynamical friction (Debattista & Sellwood, 1998) and allow the bar to lengthen without significantly decreasing pattern speed.

Fragkoudi et al. (2021) note that this higher baryon dominance is likely due to the models of stellar and AGN feedback used in Auriga being 'smoother' than those in EAGLE and Illustris. This is confirmed for EAGLE in Kelly et al. (2022), which explores the effects of rerunning a pair of zoom-in cosmological simulations from Apostle (Fattahi et al., 2016; Sawala et al., 2016) with the Auriga baryon physics model from the same initial conditions. Apostle uses the same model as EAGLE but with effectively weaker AGN feedback and a higher resolution. They find that increased stellar feedback in Apostle is responsible for suppressing the accretion of gas, thus lowering the baryon dominance of their halos.

In the IllustrisTNG simulations, Roshan et al. (2021) find mean rotation rates of $2.8^{+1.6}_{-1.0}$ in TNG100 (Marinacci et al., 2018; Naiman et al., 2018; Nelson et al., 2018; Pillepich et al., 2018; Springel et al., 2018) and $3.0^{+1.8}_{-1.1}$ in TNG50 (Nelson et al., 2019; Pillepich et al., 2019). Also, Habibi et al. (2024) find most bars have rotation rates of $1.4 - 5$ in TNG50. Using the stellar mass fractions for discs in TNG100 (from Marasco et al., 2020) and for barred galaxies in TNG50 (from Rosas-Guevara et al., 2022) one can see that both simulation runs also have lower baryon dominance than in Auriga, with TNG100 being comparable with the original Illustris and TNG50 being slightly more baryon dominated but still less so than Auriga. Therefore, following the conclusions of Fragkoudi et al. (2021), this likely accounts for the most of the difference in bar rotation rates.

What, then, is the cause of the difference in baryon dominance between Auriga and TNG50? Semczuk et al. (2024) and Frosst et al. (2025) find that kinetic mode AGN feedback in galaxies in TNG50 with stellar masses $10^{10} - 10^{11.2}\,\mathrm{M}_{\odot}$ is effective at removing cold gas from the inner disc, creating 'gas holes' up to 15 kpc in radius, most often in barred discs. Semczuk et al. (2024) show that these gas holes are linked to increased bar slow-down in TNG50. While AGN feedback can be effective in reducing star formation in barred Auriga galaxies (e.g. Irodotou et al., 2022), I find no such gas holes present in my sample. This is likely because the Auriga AGN feedback model uses a relatively gentle thermal radio mode to heat *halo gas* (Grand et al., 2017, 2024), whereas TNG instead includes a jet-driven kinetic AGN feedback mode that directly kicks out gas from the *central disc* (Weinberger et al., 2017, 2018). These differences in

AGN feedback between Auriga and TNG likely account for the higher baryon dominance and lower bar rotation rates in Auriga.

I also consider the spin of the dark matter halos. Li et al. (2023) find from tailored N-body simulations that a high value of dark matter halo spin can halt slowdown from dynamical friction. Milky Way-mass halos in TNG50 have spin parameters in the range 0.02 – 0.07, skewing towards lower values for barred galaxies (Rosas-Guevara et al., 2022), whereas all original Auriga halos have spin parameters above 0.08 (Grand et al., 2017) – this is in the regime where Li et al. (2023) find spin to halt bar slowdown for up to 5 Gyr. It is also notable that Habibi et al. (2024) find that two of the three bars in TNG50 which have sped up significantly are also in the minority that experience major mergers after $z = 1$, pointing towards galaxy interactions playing a key role in speeding up bars. There is a similar, albeit very weak, trend in Sec. 4.1.3.

Lastly, in the FIRE-2 simulations (Hopkins et al., 2018; Wetzel et al., 2023), Ansar et al. (2025) find bar rotation rates of 1.6 – 6.5. Examining the stellar masses and halos masses from Hopkins et al. (2018), one can see that FIRE-2 also has lower baryon dominance than Auriga, providing an explanation for its slower bars. I also note that the bars in FIRE-2 are very weak, with none stronger than $A_{2,\mathrm{max}} = 0.21$ (only this strongest bar would be considered a barred galaxy in this thesis). Since I find that rotation rate is negatively correlated with bar strength, I would expect such weak bars to also be slow in Auriga. Indeed, the strongest bar in FIRE-2 also has the lowest rotation rate. Ansar et al. (2025) find that the weak bars in FIRE-2 may result from repeating cycles of star formation and strong stellar feedback, disrupting the bar-forming resonances by perturbing the potential as in Weinberg (2025).

One can see that the disc galaxy population in Auriga has a higher baryon dominance than each of these five other cosmological simulations (EAGLE, Illustris, TNG50, TNG100, and FIRE-2), in addition to significantly lower average bar rotation rates. This indicates that having a high baryon dominance, likely achieved through smoother, less aggressive feedback models, is the most important factor in forming fast bars within cosmological simulations. Other ingredients, potentially including properties of merger histories and dark matter halo spin, may contribute to increasing the fraction of fast bars formed.

The higher baryon dominance found in Auriga is consistent with the SPARC (Spitzer Photometry and Accurate Rotation Curves) sample of spiral galaxies (Lelli et al., 2016), as found in Fragkoudi et al. (2021), which also lies above the expected abundance matching relation (Posti et al., 2019). Grand et al. (2017) and Grand et al. (2024) show further observational comparisons of the full Auriga suite, indicating that the relatively high baryon dominance in Auriga is consistent with, e.g., the Tully-Fisher relation, $z = 0$ star formation rates, and half-light radii.

4.2.2 Comparison with observations

While there are significant challenges to observationally measuring bar pattern speeds (e.g. Debattista, 2003; Zou et al., 2019; Garma-Oehmichen et al., 2020), here I discuss some of the studies that have explored bar pattern speeds and compared these to different parameters. In particular, I compare my results of trends with bar strength and with stellar mass, since these are measured more easily in observations than the other quantities used in this Chapter.

I first address the correlation between bar strength and rotation rate. Rautiainen et al. (2008) used models of the rotating bar potential, fitted based on the response features produced by numerical simulations of the disc, to find bar pattern speeds for 38 $z \sim 0$ bright spiral galaxies from the Ohio State University Bright Spiral Galaxy Survey (Eskridge et al., 2002). Although using a different measure of bar strength than that used in this thesis – the ratio of tangential and radial forces exerted by the bar potential in their best fit model – they find that all but one of the slow ($\mathscr{R} > 1.4$) bars in their sample have a bar strength less than 0.3. This matches the tendency for slow bars to be weaker in Fig. 4.3. It is, however, worth noting that their sample only contains six other galaxies stronger than this limit, meaning the majority of their fast bars are also weaker than 0.3. Géron et al. (2023), use the Tremaine-Weinberg method (Tremaine & Weinberg, 1984b) to find the pattern speeds of 255 bars from the MaNGA survey (Bundy et al., 2015); they also find that strong bars have lower rotation rates in agreement with Auriga. The bars in this work are classified by Galaxy Zoo (Lintott et al., 2008; Walmsley et al., 2022)

into strong and weak categories which have rotation rates of $1.53^{+0.74}_{-0.53}$ and $1.88^{+1.08}_{-0.75}$ respectively.

Other works find no such relation between rotation rate and bar strength in observations. Guo et al. (2019) also use the Tremaine-Weinberg method to find pattern speeds in a smaller sample (53) from the MaNGA survey and find no correlation with bar strength. Cuomo et al. (2020) adds 18 bars from the literature and 31 bars from the CALIFA survey (Calar Alto Legacy Integral Field spectroscopy Area survey; Sánchez et al., 2012; Walcher et al., 2014) to this sample, making 77 bars once additional quality cuts are imposed, and finds the same lack of correlation. It is unsurprising that these studies agree with each other, given the large overlap in galaxy sample. Another similarity which may affect their results, is that they find corotation radii by assuming that the rotation curve of the disc very quickly flattens to a constant circular velocity. Rautiainen et al. (2008) and Géron et al. (2023), the two studies which do see a correlation between bar strength and rotation rate, instead model the rotation curve for a (potentially) more accurate corotation radius. In summary, although not all observations support a correlation between bar strength and rotation rate, the relatively large sample and accurate method for measuring the corotation radius of Géron et al. (2023) is compelling evidence for a correlation.

The correlation between stellar mass and bar rotation rate is of particular interest since, as mentioned in Sec. 4.1.2.1, it provides a test of ΛCDM cosmology. The correlation could be caused by the underlying trend of higher stellar mass galaxies having higher baryon dominance. Due to the lack of dark matter in a Modified Newtonian Dynamics framework (Milgrom, 1983), we would not expect to see a dependence of rotation rate on galaxy mass in such scenarios (since there is no trend or change in 'baryon-dominance'). Indeed, the study of Nagesh et al. (2023) explored bars in a MOND framework, showing that galaxies with masses $10^9 - 10^{11}\,\mathrm{M}_\odot$ all have similar rotation rates of $\mathscr{R} \sim 1.6$.

In observations, Géron et al. (2023) show a weak negative correlation between bar rotation rate and stellar mass in their Fig. 13. This figure shows that weak bars tend to have higher rotation rates in lower mass galaxies for $M_\star \lesssim 3 \times 10^{10}\,\mathrm{M}_\odot$. Above this mass, bars have rotation rates which are lower, but approximately constant with stellar mass. There is a similar shape in the rotation rate-stellar mass relation for Auriga in

Fig. 4.4, but with a slightly higher transitional mass of $6 \times 10^{10}\,M_\odot$: five of the six galaxies with stellar masses below $6 \times 10^{10}\,M_\odot$ in my sample have slow bars, all of which have weaker bars than the median.

Two other works examine the relation between bar rotation rate and stellar mass: Garma-Oehmichen et al. (2020) which investigates 18 galaxies from the MaNGA and CALIFA surveys, and Garma-Oehmichen et al. (2022) which applies the Tremaine-Weinberg method to 97 galaxies from the MaNGA survey with masses and morphology similar to the Milky Way. Both studies find no correlation between rotation rate and stellar mass. I note, however, that both studies have a smaller sample size than Géron et al. (2023), especially Garma-Oehmichen et al. (2020) which only finds a convergent pattern speed for 13 galaxies due to its focus on galaxies which present challenges to the Tremaine-Weinberg method. Garma-Oehmichen et al. (2022) also has a lower stellar mass limit of $2 \times 10^{10}\,M_\odot$ – this would likely hide a trend like in Géron et al. (2023) which only appears below $3 \times 10^{10}\,M_\odot$, especially since the relation is presented as a correlation coefficient only.

Guo et al. (2019) additionally investigates the dark matter fraction within an effective radius, the inverse of baryon dominance. In their Fig. 11, there is a weak negative correlation between rotation rate and dark matter fraction (more slow bars have higher dark matter fractions, corresponding to lower baryon dominance) in the discs with the most reliable position angles. This is in agreement with my results in Fig. 4.5, although the observations show a much weaker correlation.

The relationships between bar rotation rate and bar strength, stellar mass, and baryon dominance found in some observations are consistent with my findings. While not all observational studies agree with my results, those that do have either have larger sample sizes or fewer assumptions in calculating their rotation rates, which lends tentative support to the bar evolution in the Auriga simulations, the baryon physics involved, and the ΛCDM cosmology producing it. Future observations may clarify the picture currently presented, allowing the trends I have presented here to give a more robust test of bar evolution in Auriga. In particular, studies of bars in lower mass disc galaxies may provide a crucial test for the relations that I find.

4.3 Conclusions

In this Chapter, I investigated the internal and external physical processes that set the bar pattern speed and drive its evolution in simulated Milky Way-mass galaxies. I used 27 high temporal resolution reruns from the Auriga suite of magneto-hydrodynamic cosmological zoom-in simulations to compare bar rotation rates, $\mathscr{R}$ (the ratio of corotation radius to bar length), with bar formation times and strengths, as well as with the baryon/dark matter composition and interaction histories of their host galaxies.

I summarise my conclusions as follows:

- All but one of the bars in the Auriga suite of simulations decrease in rotation rate from their formation to the present day, largely due to an increase in bar length and approximately constant corotation radius (e.g. Fig. 4.1 and Fig. 4.2). This speed-up in $\mathscr{R}$ is unexpected when compared to the literature, and implies that any dynamical friction acts on short timescales, having little effect following 0.5 Gyr after the bar forms.

- Younger (older) bars tend to have a slower (faster) rotation rate (ratio of corotation radius to bar length) by the end of the simulation (Fig. 4.2). Younger bars are also slower than older bars shortly after the bar formation time, suggesting that the mechanism responsible for the difference acts mostly within the first 0.5 Gyr of bar evolution.

- Bars that are stronger at $z = 0$ tend to be faster (Fig. 4.3). This is a relation that can be tested in the nearby Universe and is confirmed in some, but not all, observational studies.

- Galaxies with higher stellar masses tend to host faster bars (Fig. 4.4). This relation acts as a test of the ΛCDM model of cosmology and baryon physics in Auriga, since it seems to be driven by the higher fractions of stellar to dark matter in high mass galaxies. This relation has so far been observed in weak bars at stellar masses below $3 \times 10^{10}\,\mathrm{M}_{\odot}$.

- The ratio of stellar to dark matter (or baryon dominance) within galaxies appears to be the strongest factor in setting the rotation rate at both the start and end of the lifetime of their bars up to $z = 0$. Regardless of epoch, bars in more baryon dominated environments are faster (Fig. 4.4 and Fig. 4.5); additionally, bars tend to speed up when their host galaxies increase in baryon dominance (Fig. 4.6).

- Galaxy interactions at the time of bar formation have little immediate effect on pattern speed, however bars formed alongside stronger interactions tend to speed up more through their life and become slightly faster by $z = 0$ (Fig. 4.7). The mechanisms behind this are unclear, but may relate to the trends with baryon dominance – possibly due to interactions driving in-situ baryons towards the galactic centre or by adding gas to the system directly. Regardless of mechanism, this contradicts the expectation from literature that tidally formed bars are slower on average.

- There is a weak trend between stronger galaxy interactions after the bar has formed and a greater decrease in bar rotation rate (Fig. 4.8). This effect is, however, minimal when compared to the other correlations presented here.

The Auriga simulations give an insight into how fast bars in Milky Way-mass halos can arise in cosmological simulations. A high baryon dominance in the inner regions appears to be crucial, as do relatively early-forming bars. Comparison with bars in other cosmological simulations supports the need for high baryon dominance in order to produce fast bars in Milky Way-mass discs. Having this baryon dominance likely counters dynamical friction in Auriga to stop these bars slowing down excessively by present day and even allowing the majority to speed up. This Chapter highlights the potential constraining power of bar rotation rates on the nature of dark matter and baryonic physics.

Chapter 5

The reliability of the Tremaine-Weinberg method in a fast-barred cosmological simulation

This Chapter is structured as follows. In Sec. 5.1 I outline the motivation, use, and typical errors of the Tremaine-Weinberg method for finding pattern speeds in disc galaxies. I describe how I apply the method to my simulation sample in Sec. 5.2. In Sec. 5.3 I present my results, examining in detail the effect of warps in Sec 5.3.1 and an alternative interpretation as position angle errors in Sec. 5.3.2. Lastly, I summarise and conclude my results in Sec. 5.4, including future work which I plan to carry out.

5.1 Introduction to the Tremaine-Weinberg method

Bar pattern speed is an important quantity to measure in order to understand the dynamical evolution of a barred galaxy, as outlined in Sec. 1.3. However, as mentioned in Sec. 1.5, observations of external galaxies are limited by only having one snapshot of their evolution available. This means that pattern speeds of bars in external galaxies cannot be measured by the change in angle of the bar (as I use in Chapter 4) since a rotation occurs on the order of 10^8 yr. Additionally, full six-dimensional kinematic

data for individual stars is unavailable outside the Milky Way. Instead, any method for measuring bar pattern speed must rely on observations of the bulk motion of material in the galaxy, using only position in the sky and line-of-sight velocity.

It is possible to use models of the galaxy to bridge this gap, by testing the response of gas in simulations with different pattern speeds to see which speed produces the closest match to the gas in the observed galaxy. Hunter et al. (1988), Salo et al. (1999) and Weiner et al. (2001) use this method with 2D simulations to find pattern speeds in one galaxy each and Kranz et al. (2003) find pattern speeds of spirals in five galaxies. Rautiainen et al. (2008) add the response of star particles to the method to find the pattern speeds of 38 bars. However, Sormani et al. (2015) note that it can be difficult to fit all the features of a barred galaxy with one model. This method is also computationally demanding, requiring multiple simulations to match each observation. Structures expected to result from bar or spiral arm rotation can also indicate pattern speed: Elmegreen et al. (1989) match gaps in the spiral arms of a galaxy to rotation resonances, Sempere et al. (1995) match a change of sign in the radial streaming motions along spirals to the corotation radius as predicted by Canzian (1993), and Kuno et al. (2000) put an upper limit on a bar's pattern speed by the velocity of molecular gas at the leading edge of the bar (this assumes that the bar is not ultrafast, so that corotation lies outside the bar and this gas will rotate faster than corotation). Additionally, recently developed methods from Vasiliev & Valluri (2020), Tahmasebzadeh et al. (2022) and Jin et al. (2025) find the pattern speed by orbit superposition. This works by reconstructing the light from the observed galaxy as an overlay of stellar orbits taken from a modelled orbital library, itself constructed by fitting to the gravitational potential of the galaxy. However, all the methods in the paragraph suffer from reliance on a model, leading to a dependence on assumed parameters and physics choices. The behaviour of resonances is also still not fully understood, leading to at least degeneracies in these methods.

Tremaine & Weinberg (1984b) formulated a way to obtain model-independent pattern speed measurements, known as the Tremaine-Weinberg (TW) method. As laid out in this paper, the method requires just three assumptions: a flat disc, a constant pattern speed across the whole disc, and a tracer whose surface brightness obeys the continuity equation. The continuity equation requires that the tracer (and its luminosity) simply

move through the galaxy rather than be created, destroyed, dimmed, or brightened. Applying the first assumption, for motion in the plane of a disc (with the disc in the x-z plane) the continuity equation becomes:

$$\frac{\partial \Sigma\left(x,z,t\right)}{\partial t} + \frac{\partial \Sigma\left(x,z,t\right) v_x\left(x,z,t\right)}{\partial x} + \frac{\partial \Sigma\left(x,z,t\right) v_z\left(x,z,t\right)}{\partial z} = 0 \tag{5.1}$$

where $\Sigma\left(x,z,t\right)$ is the surface density of the tracer at position (x,z) and time t. v_x and v_z are the net velocities of the tracer in the x and z directions at the same position and time. Adding the second assumption, that patterns in the disc rotate with a single speed across the whole disc, the continuity equation can be manipulated (see Tremaine & Weinberg, 1984b, for further details) to give:

$$\Omega_{\mathrm{p}} = \frac{1}{\sin i}\frac{\langle V_{\mathrm{LOS}}\rangle}{\langle X\rangle} \tag{5.2}$$

where i is the inclination angle of the disc. $\langle V_{\mathrm{LOS}}\rangle$ and $\langle X\rangle$ are the mean surface-density weighted line of sight velocity and x-position respectively, given by:

$$\langle V_{\mathrm{LOS}}\rangle = \int_{-\infty}^{\infty}\int_{-\infty}^{\infty} h\left(z\right) v_{\mathrm{LOS}}\left(x,z\right) \Sigma\left(x,z\right) dx\, dz \tag{5.3}$$

$$\langle X\rangle = \int_{-\infty}^{\infty}\int_{-\infty}^{\infty} h\left(z\right) x\, \Sigma\left(x,z\right) dx\, dz \tag{5.4}$$

where $v_{\mathrm{LOS}}\left(x,z\right)$ is the mean line of sight velocity at position (x,z) and $\Sigma\left(x,z\right)$ is the surface density at that position, all for some tracer within the disc. $h\left(z\right)$ is free to be chosen, but practical application will choose a step function such that $h\left(z\right) = 1$ within a small range of z and $h\left(z\right) = 0$ outside of this. This gives a thin aperture along which to calculate $\langle V_{\mathrm{LOS}}\rangle$ and $\langle X\rangle$. To avoid systematic errors, it is common practice to use multiple apertures and calculate the gradient rather than individual ratios to obtain Ω_{p}.

The TW method has been applied to find the pattern speeds of many bars in external galaxies, including those in Corsini (2011), Aguerri et al. (2015), Guo et al. (2019),

Garma-Oehmichen et al. (2020), Cuomo et al. (2020), Garma-Oehmichen et al. (2022) and Géron et al. (2023) which I compared my simulation sample to in Chapter 4. It is even applicable out to $z = 1.2$ (Roshan et al., 2025). The method does require an inclined viewing angle for both the disc and the bar, with Zou et al. (2019) finding accurate results for disc inclinations of $15 - 70°$ and angles of the bar to the disc major axis of $\pm 10 - 75°$. This places both the bar and the disc at an angle which ensures both that $\langle V_{\rm LOS} \rangle$ captures the behaviour of velocities within the disc, and that $\langle X \rangle$ captures the shape of the bar. From isotropy, i.e. assuming that disc galaxy orientations are randomly and uniformly distributed, this indicates the TW method can be successfully applied to 45% of bars in the Universe within observational limits (since a random disc orientation has a $\cos 15° - \cos 70° = 62\%$ chance of lying in the range $15 - 70°$ to a fixed observer and bars within these have a $\frac{65}{90} = 72\%$ chance to lie in a $\pm 10 - 75°$ range to the major axis).

Despite its advantages, the TW method does have significant sources of error. Firstly, no observable tracer exactly satisfies the continuity equation, since hydrodynamic processes will constantly lead to baryon states exchanging mass with each other, as gas cools, cold gas forms stars, stars die and feedback heats gas. In practice, however, star and gas tracers are both usable due to the long timescale over which these processes produce significant differences in mass and light surface density across a galaxy. Stellar surface density in particular is known to be a relatively reliable tracer. Fathi et al. (2009) find that Hα is also an accurate tracer (if Hα is present in the bar) and CO measurements have also been used in, for example, Zimmer et al. (2004). However, Rand & Wallin (2004) find, using a simulation, that a clumpy distribution of gas can lead to a false finding of a pattern speed with the TW method. In comparison to stellar tracers, Williams et al. (2021) find that Hα and CO overestimate the bar pattern speed by 20% and 40% respectively, tracing instead the angular frequency of the disk. Borodina et al. (2023) find similar errors from simulations, where the true pattern speed is known, with HI giving a 20% underestimate and CO giving a 30% overestimate. They also found that tracing the gas directly does in fact recover the true pattern speed, but since this cannot be applied to observation, stellar light remains the most reliable tracer.

Secondly, discs often contain more than one structure with differing speeds, breaking the second assumption for the TW method above. These are mostly caused by spirals or double-barred systems and often lead to a radial separation of the two conflicting pattern speeds. In these cases, a modification to the TW method in Merrifield et al. (2006) can identify the pattern speed of each component (Meidt et al., 2008). However, if the multiple pattern speeds have an overlap in radius, then radial separation such as in this modified TW method may be insufficient.

The first assumption for the TW method above, that the disc is flat, can be sensitive to errors in finding the plane of the disc. Application to simulations in Debattista (2003) show that an error in position angle (the angle of the major axis of the disc on the sky) of $2-3^{\circ}$ can lead to an error in the TW method of up to 30%, with a similar magnitude of error found in Zou et al. (2019). In observations, Garma-Oehmichen et al. (2020) find that uncertainty in the disc position angle is the dominant source of error for 13 of their 18 galaxy sample, producing $\sim$ 15% uncertainties due to differences in the position angle when calculated from photometry versus kinematics. This indicates that uncertainties in the position angle of the disc is the predominant source of error when using the TW method.

There are discs where the disc plane varies with radius – those affected by warps. Around 70% of disc galaxies have a detectable warp, most of which are S shaped (Ann & Park, 2006). These can arise from galaxy interactions (Huang & Carlberg, 1997; Schwarzkopf & Dettmar, 2001; Kim et al., 2014), misaligned gas accretion (Quinn & Binney, 1992; Shen & Sellwood, 2006; Roškar et al., 2010), or a number of other possibilities (e.g. Sparke & Casertano, 1988; Sellwood, 1996). In the (original) Auriga suite of simulations, Gómez et al. (2017) also find 70% with a warp, formed through galaxy interactions and misaligned gas accretion.

Since a warp acts to make a constant plane for the disc impossible to find, it would be expected that it should lead to a large uncertainty in the pattern speed from the TW method. The TW method is derived from the continuity equation for planar motion, so that the line of sight velocity should originate from planar kinematics alone. Warps, though, imply a vertical component to the motion, which can contaminate $\langle V_{\rm LOS} \rangle$ and is

not taken into account by the method. Warps tend to only become pronounced at a larger radius than the bar (Briggs, 1990; van der Kruit, 2007; Reshetnikov et al., 2016), leading to them having been ignored in prior studies, such as Debattista (2003). However, the warps in Auriga extend further towards the centre of the disc (Gómez et al., 2017), potentially leading to significant errors in the TW method.

A realistic cosmic environment, with ongoing star formation, gas accretion and galaxy interactions, as well as significant disc warps, makes Auriga a very suitable simulation suite to study the effects of warps on observations of pattern speeds. Additionally, as shown in Fragkoudi et al. (2021) and Chapter 4 of this thesis, the bars in Auriga are faster than those in other cosmological simulations, therefore being potentially more realistic. Evaluating the application of the TW method to a simulation suite which matches both bar properties and cosmological interaction histories may offer novel insight into the cases where the TW method can be reliably used in observations.

5.2 Applying the Tremaine-Weinberg method

Since stellar light is the most reliable tracer in external galaxies (see Sec. 5.1), I use the star particles in the Auriga simulations as my tracer for applying the TW method to measure their bar pattern speeds. Having rotated the disc into the x-y plane as in Sec. 2.2.1.1, I rotate the bar into the x direction from its angle as found in the same section. I then rotate the bar to be at an angle of 45° from the x-axis, and rotate the disc around the x-axis by 45°. I treat the observer as viewing in the y-direction. This gives a viewing angle which lies firmly in the ranges found in Zou et al. (2019) (again see Sec. 5.1).

Since Auriga has discrete star particles with known masses, I replace the integrals with sums and weight by mass rather than surface density. The formulation of the TW method then becomes:

$$\Omega_{\rm p} = \frac{1}{\sin 45^\circ} \frac{\langle V_{\rm LOS} \rangle}{\langle X \rangle} = \sqrt{2} \frac{\sum_n m_n v_{{\rm LOS},n}}{\sum_n m_n x_n} \tag{5.5}$$

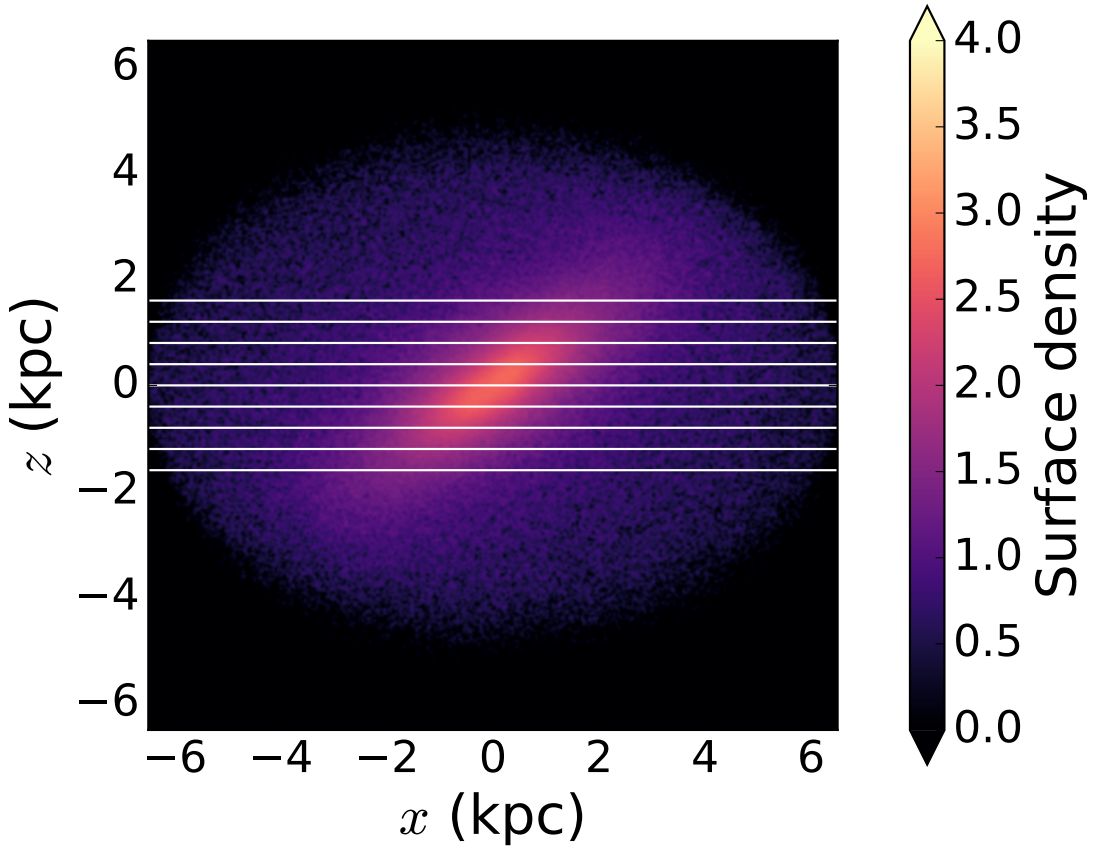


FIGURE 5.1: An illustration of the apertures used for calculating $\langle V_{\rm LOS} \rangle$ and $\langle X \rangle$ for the final snapshot of Auriga 24. The colour scale shows the surface density of stars after filtering. The horizontal, white lines indicate the bounds of every fourth aperture used. Note that the overdensity of the bar is at a negative x position for lower slits and a positive x position for higher slits.

for n stellar particles within the z aperture with masses m_n, line of sight velocities $v_{{\rm LOS},n}$[1], and positions x_n.

In practice, summing for all of $-\infty < x < \infty$ and $-\infty < y < \infty$ will include other galaxies, so I only consider star particles within 1 kpc of the disc plane and out to the disc extent $R_{\rm disc}$. I also limit the stellar particles to a radius of twice the bar length in the disc plane, since the information needed for the TW method is contained within the bar radius. The surface density of the remaining stars after this filtering and the 45° rotations is shown in Fig. 5.1 for Auriga 24. The horizontal white lines show apertures across which to measure $\langle V_{\rm LOS} \rangle$ and $\langle X \rangle$. I choose apertures of width 0.1 kpc out to the extent of the bar (Zou et al. (2019) find that the choice of slit width is relatively

[1]Note that I treat velocities towards the viewer as positive. This choice gives positive pattern speeds for the viewing angle I set my discs to.

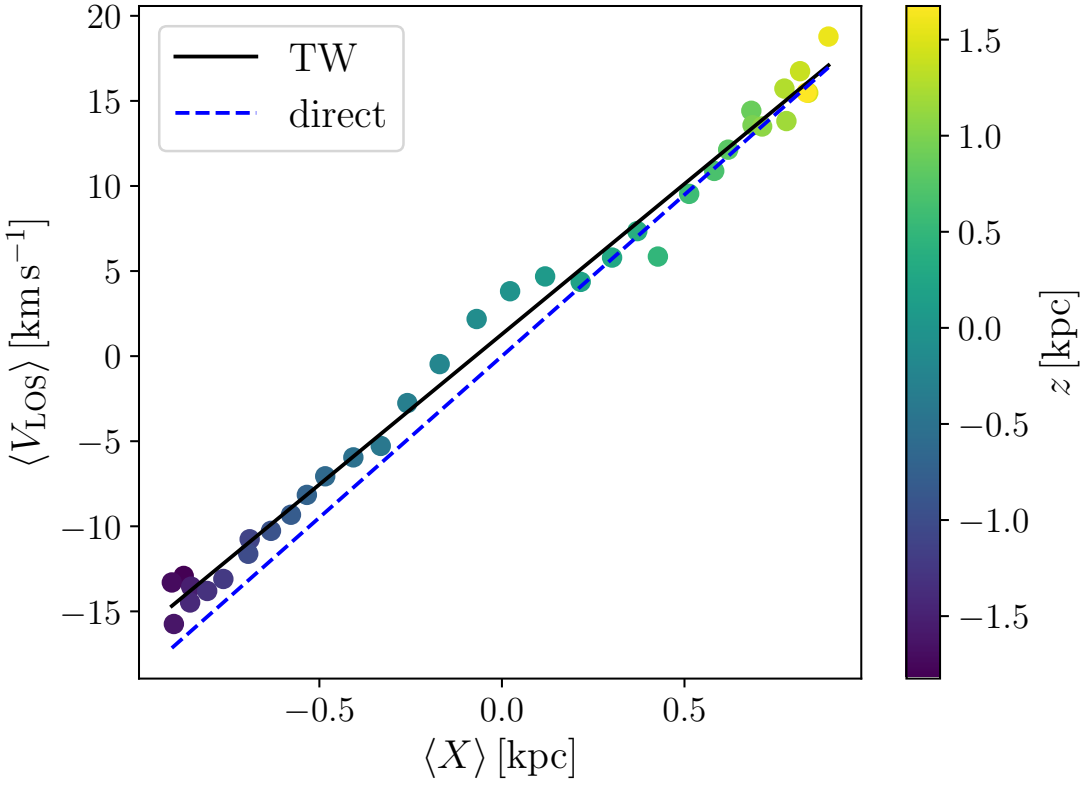


FIGURE 5.2: Mean horizontal position and mean line of sight velocity for 0.1 kpc apertures from the example in Fig. 5.1. The resulting gradient is shown by the solid black line, with the dotted blue line indicating the gradient which would correspond to the true pattern speed. The colour scale of the points shows the z position of each aperture.

unimportant to accuracy, so I make this choice to balance the number of slits with the number of particles in each slit), corresponding to $\frac{1}{2}r_{A_2}$, the range shown in Fig. 5.1 – note that the factor of $\frac{1}{2}$ is due to the rotated projection (a factor of $\frac{1}{\sqrt{2}}$ from both the 45° rotation of the bar and the 45° inclination of the disc).

Fig. 5.2 shows the calculations from each aperture in this example. The black line gives the least squares linear fit of $\langle V_{\rm LOS}\rangle$ and $\langle X\rangle$, which indeed can be seen to fit the points well, and the gradient of which is $\Omega_{\rm p}/\sqrt{2}$. In the following, I will refer to the estimated bar pattern speed obtained from this gradient as $\Omega_{\rm TW}$, and the true pattern speed calculated from the change in bar angle between snapshots as $\Omega_{\rm p}$. In this case, $\Omega_{\rm TW}$ finds a pattern speed of $25.0\,{\rm km\,s^{-1}\,kpc^{-1}} = 25.6\,{\rm rad\,Gyr^{-1}}$, an underestimate of $\Omega_{\rm p} = 27.4\,{\rm rad\,Gyr^{-1}}$ by 7%. This can be seen by the slightly shallower gradient in Fig. 5.2 when compared to the dotted blue line, which represents the direct pattern

speed.

5.3 Results and discussion

Fig. 5.3 shows the how the estimate of the bar pattern speed compares to the true pattern speed for each bar at $z = 0$. One can see in the top panel that the TW estimate is generally in good agreement with the actual value, with 15 of the 18 bars having lower than 10% errors on average. The bottom panel shows this as an absolute relative error on the TW method (this is calculated at each snipshot before finding the median and uncertainties, hence the differences in e.g. Auriga 9). Most bars still have less than 10% errors from the TW method in this measure, particularly those with pattern speeds above 25 rad Gyr^{-1}; the five bars below this speed mostly have larger relative errors (and larger errors in the top panel). The key question then comes to be: what causes the higher errors in some cases?

In Auriga 23, a double-barred system is responsible for the highest absolute relative error in the TW method. These bars have slightly different pattern speeds, which the TW method does not account for [2]. Similarly, Auriga 9 has a strong secondary pattern at $z = 0$. This pattern overlaps with the bar at a lower pattern speed, leading to large inaccuracies in the TW method. The pattern even causes large oscillations in the change in bar angle, used to find the 'true' pattern speed. From visual examination of the face-on surface density profile, or the RGB image in Fig. 2.1, this pattern appears more spiral-like than bar-like, but is strong enough to affect measurements.

5.3.1 The effects of warped discs

Since the position angle of the disc can have large effects on the accuracy of the TW method, it is reasonable to assume that warps in the disc, which can be viewed as spatially varying changes to the plane of the disc, would introduce some errors to the

[2] See Sec. 5.1 for a variation on the TW method which can account for this (Merrifield et al., 2006). I only consider the original version of the TW method for simplicity and its generality of usage.

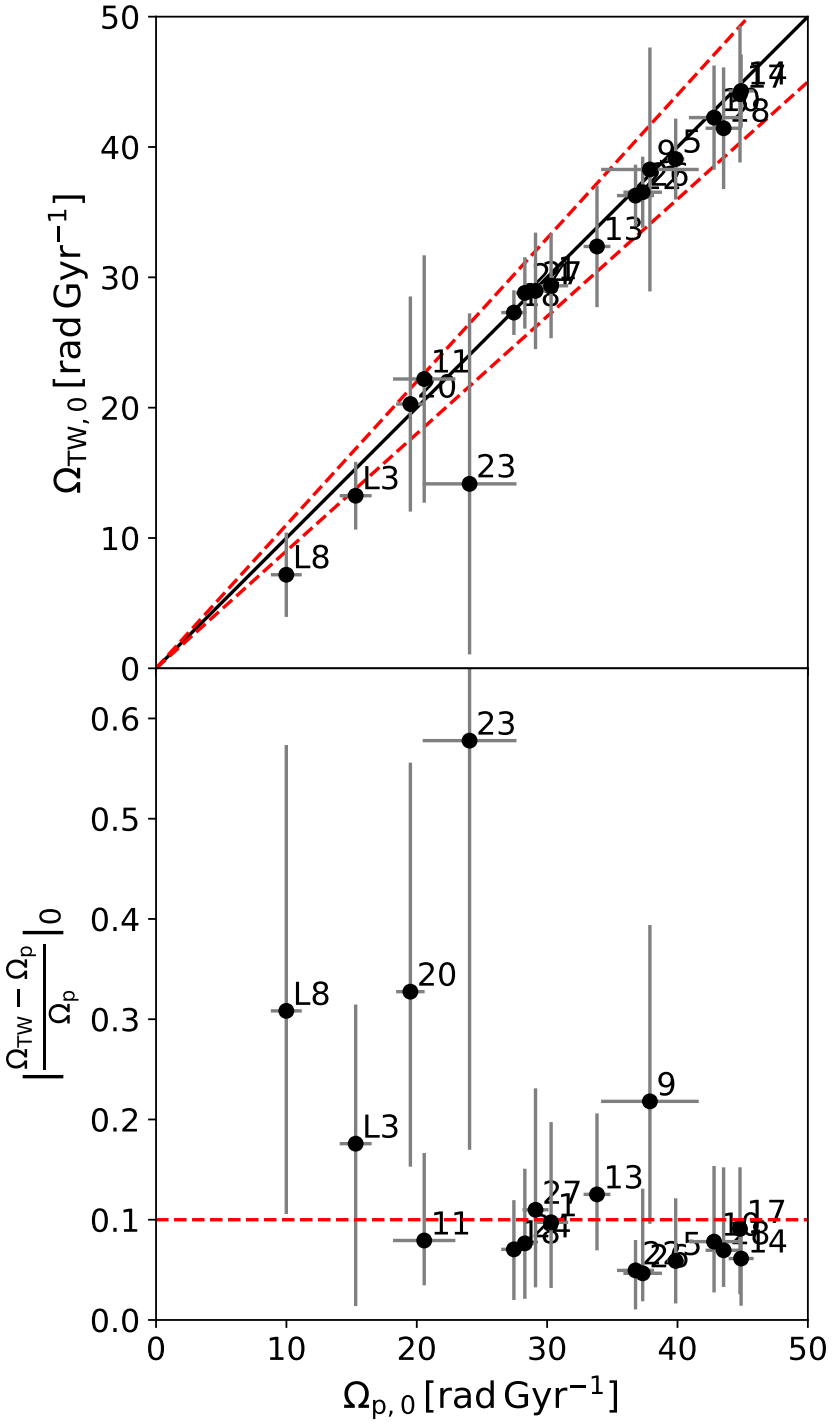


FIGURE 5.3: The TW method estimate of pattern speed (top) and the absolute relative error in the TW method (bottom) plotted against the true pattern speed. For each bar at $z = 0$, the points and error bars show the median and $16^{\mathrm{th}}/84^{\mathrm{th}}$ percentiles across the last 60 snipshots (roughly 300 Myr) of the simulation. This time corresponds to a full rotation for a bar with $\Omega_{\mathrm{p}} \simeq 20\,\mathrm{rad\,Gyr^{-1}}$, so captures at least one rotation of all but the slowest few bars. A point lying on the black dotted line in the top panel indicates the TW method recovering the true bar pattern speed, and the red dotted lines in both panels indicate 10% errors.

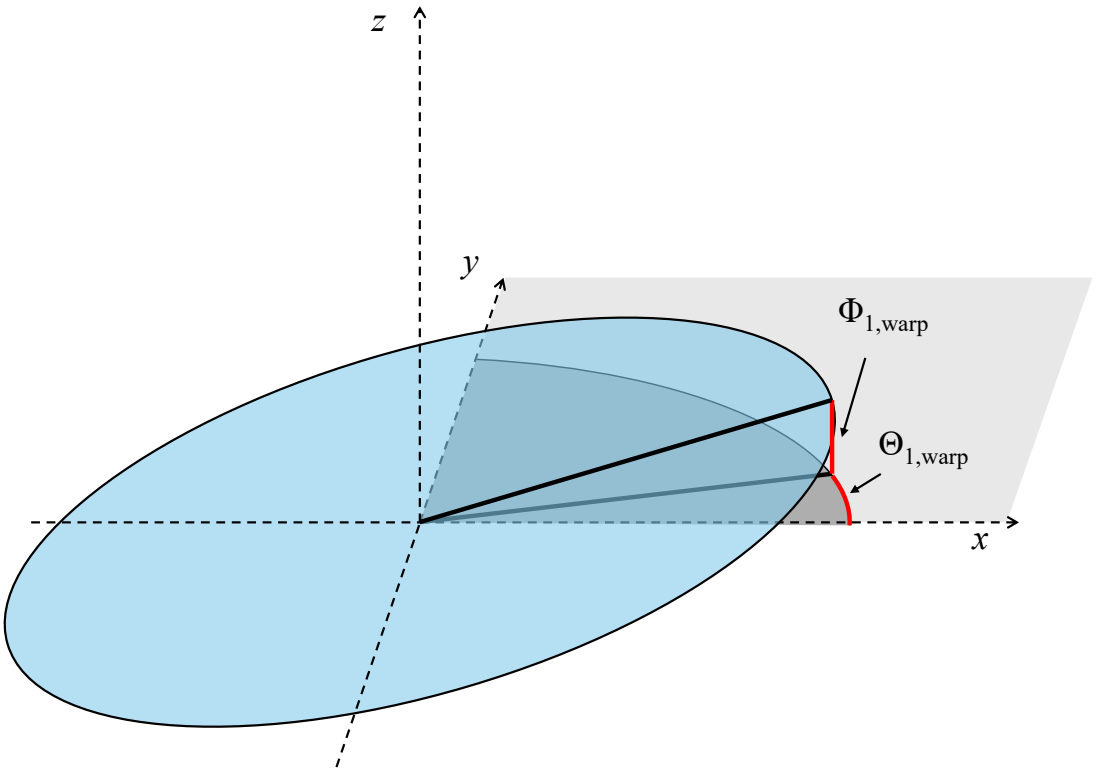


FIGURE 5.4: An illustration of the angles which I use to describe the warp of a disc, as calculated in Sec. 2.2.1.4. The bar lies in the x-direction. The angle from the highest point of the disc to the $x-y$ plane (at a set radius) is $\Phi_{1,warp}$ and is shown by the vertical red line. The angle from where this meets the $x-y$ plane to the x axis (along which the bar lies) is $\Theta_{1,warp}$ and is shown by the red curve – I define the angle as positive in this example. Note that the illustration assumes constant angles throughout the disc for clarity – this does not reflect the actual warps seen.

method (see Sec. 5.1 for further discussion of this). Fig. 5.5 shows the absolute relative error in the TW method against the angle of the disc warp to the x-y plane, $\Phi_{1,warp}$, as calculated from the magnitude of the first Fourier mode of the mean disc height at 2.5 kpc. This acts as the magnitude of the warp – see Sec. 2.2.1.4 and the illustration of this angle in Fig. 5.4. The error bars indicate the variation of the parameters over the final 60 snipshots of the simulation. Below $\Phi_{1,warp} = 1°$, the application of the TW method here generally achieves better than 10% accuracy. However, around and above $\Phi_{1,warp} = 1°$ one sees an almost linear increase in the error, clearly shown by Aurigas 13, L3, 9, 20, and L8. These are the five single-barred galaxies with the highest error in the TW method, and all have the most significant warps in their inner disc. Auriga 11, shown in blue, appears to have relatively low errors, despite the largest warp in some of its snipshots (seen in the extended horizontal error bar in the lower right of the figure),

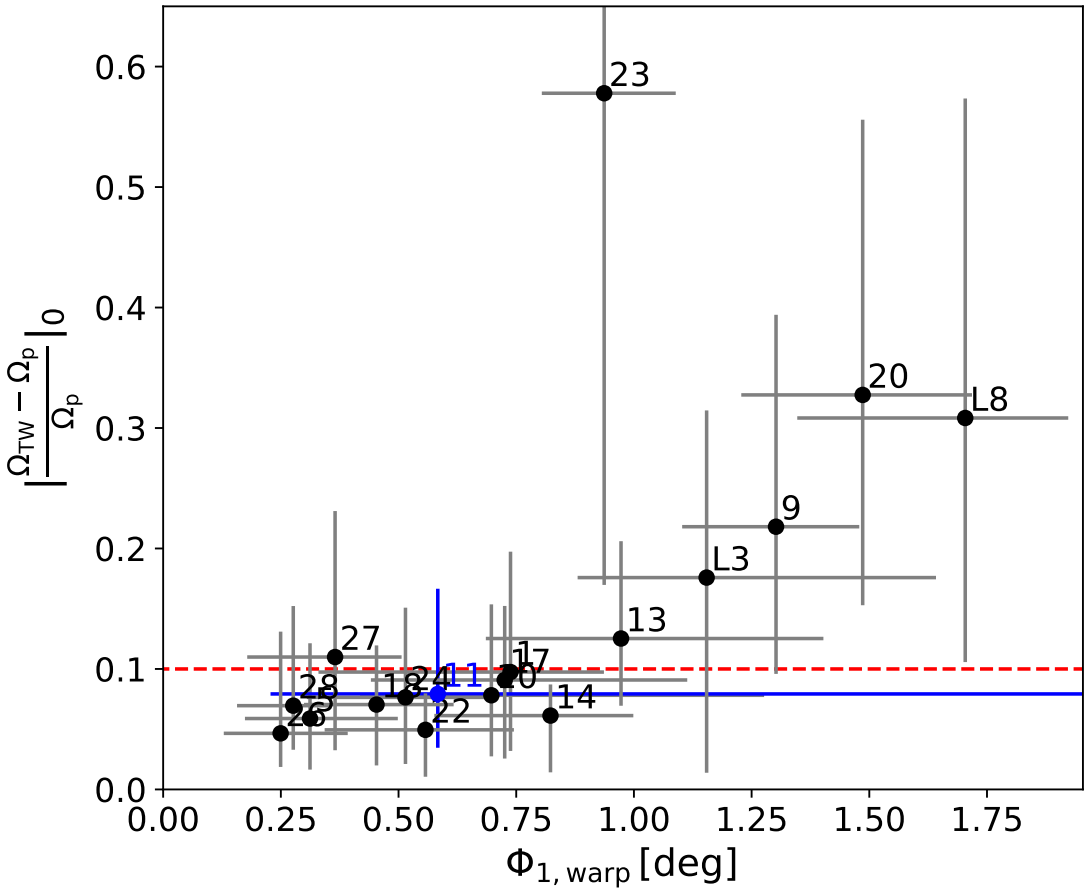


FIGURE 5.5: The absolute relative error in the TW method plotted against the angle of the warp from the disc plane at 2.5 kpc. For each bar at $z = 0$, the points and error bars show the median and 16^{th}/84^{th} percentiles across the last 60 snipshots of the simulation. The red dotted line indicates 10% errors.

but this is due to being in the early stages of a merger, as seen in Fig. 2.1. This merger causes an increase in the warp signature over the duration of the final 30 snipshots, contributing to a large 84^{th} percentile warp amplitude. On the other hand, the errors in the TW method only increase in the last 10 snipshots, which all lie above the error bars shown. The 20 snipshots in which there is a large warp with little effect on the TW method requires information on the angle of the warp to explain. A similar phenomenon appears in the other heavily warped galaxies, where some snipshots with large warps do not produce errors in the TW method, and I investigate this below.

I take a closer look at the effect of the angle of the warp axis $\Theta_{1,warp}$ (the angle relative to the bar of the line of greatest absolute vertical height – see Sec. 2.2.1.4 and the illustration of this angle in Fig. 5.4) on the TW method in Fig. 5.6, showing the dependence of relative

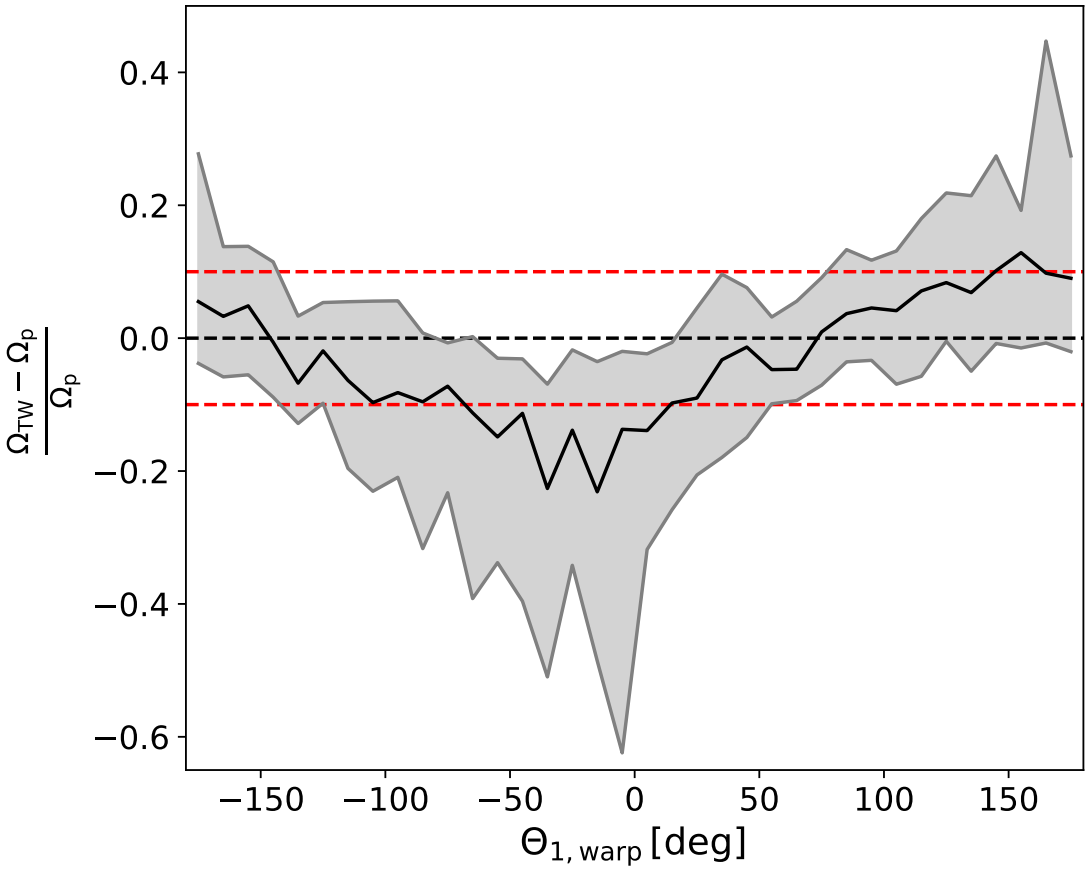


FIGURE 5.6: The variation in median relative error in the TW method with the angle of the warp axis at 5 kpc relative to the bar, for the last 60 snipshots of each barred galaxy. The median (black line) and 16th and 84th percentiles (grey lines) are calculated in 10° bins. The black dotted line indicates the TW method recovering the true bar pattern speed, and the red dotted lines indicate 10% errors.

error in the TW method (signed rather than absolute) on the angle of the warp's main axis relative to the bar, $\Theta_{1,\mathrm{warp}}$. The black line with grey confidence interval gives the average errors at each warp axis angle, over all $z = 0$ barred galaxies and the last 60 snipshots. Since I rotate the galaxy by 45° before applying the TW method, it is useful to note that $\Theta_{1,\mathrm{warp}} = -45°$ corresponds to a warp which is along the x-direction and raised to the right. Similarly, $\Theta_{1,\mathrm{warp}} = 135°$ corresponds to a warp which is along the x-direction and raised to the left, $\Theta_{1,\mathrm{warp}} = 45°$ corresponds to a warp which is along the line of sight and raised in the background, and $\Theta_{1,\mathrm{warp}} = -135°$ corresponds to a warp which is along the line of sight and raised in the foreground.

A strong dependence on angle is evident. The TW method is reasonably accurate for warps around −180° to −90° and around 30° to 120°, but overestimates the true pattern

speed for angles of 120° to 180° and severely underestimates it for angles of −90° to 30°. From the 45° viewing angle mentioned above, this means that the TW method is mostly unaffected for warps along the line of sight, but inaccurate for warps close to along the x-direction. This is useful for observation, since only a warp at least partially along the x-direction is visible from light density alone, meaning that the greatest errors from warps in the TW method come from the most easily detectable warps.

This also explains the 20 snipshots in Auriga 11 in which there is a large warp but the TW method remains accurate. Immediately before the warp begins to strengthen, it is at an angle of −50° to the bar, in the region which would produce an underestimate given a significant warp. However, as the warp grows, its angle to the bar immediately decreases, moving through the −180° to −90° region of Fig. 5.6 where there is little effect on the TW method. It is only 10 snipshots before the end of the simulation that the warp moves into the 120° to 180° region of Fig. 5.6, leading to the overestimate of the pattern speed seen in the upper panel of Fig. 5.3. Since I am plotting percentiles, this then explains the large warp but accurate TW method shown in the extended error bar of Fig. 5.5.

Fig. 5.7 shows the vertical height and velocity of stars in Auriga L8 (the greatest genuine disc warp in Fig. 5.5) 20 snipshots before the end of the simulation. I show a face-on view of the galaxy, after filtering and rotating the bar, but before inclining the disc by 45°. The bar itself corresponds to the length and angle of the black line in both panels. From the top panel one can see that the warp in this snipshot is at an angle of $\sim$ 135° to the bar, and will appear as the disc being raised on the left and lowered on the right after the disc is inclined (since I rotate the top of the disc away from the viewer to take the TW method).

It is not, however, the visual profile of the warp that leads to inaccuracies in the TW method, but rather the vertical velocity induced to maintain the warp. This velocity is shown in the lower panel of Fig. 5.7 for the same snipshot. The pattern from the top panel is rotated by 90°, since stars must move up (down) when travelling from a lowered (raised) portion of the disc to a raised (lowered) portion. In this example, one

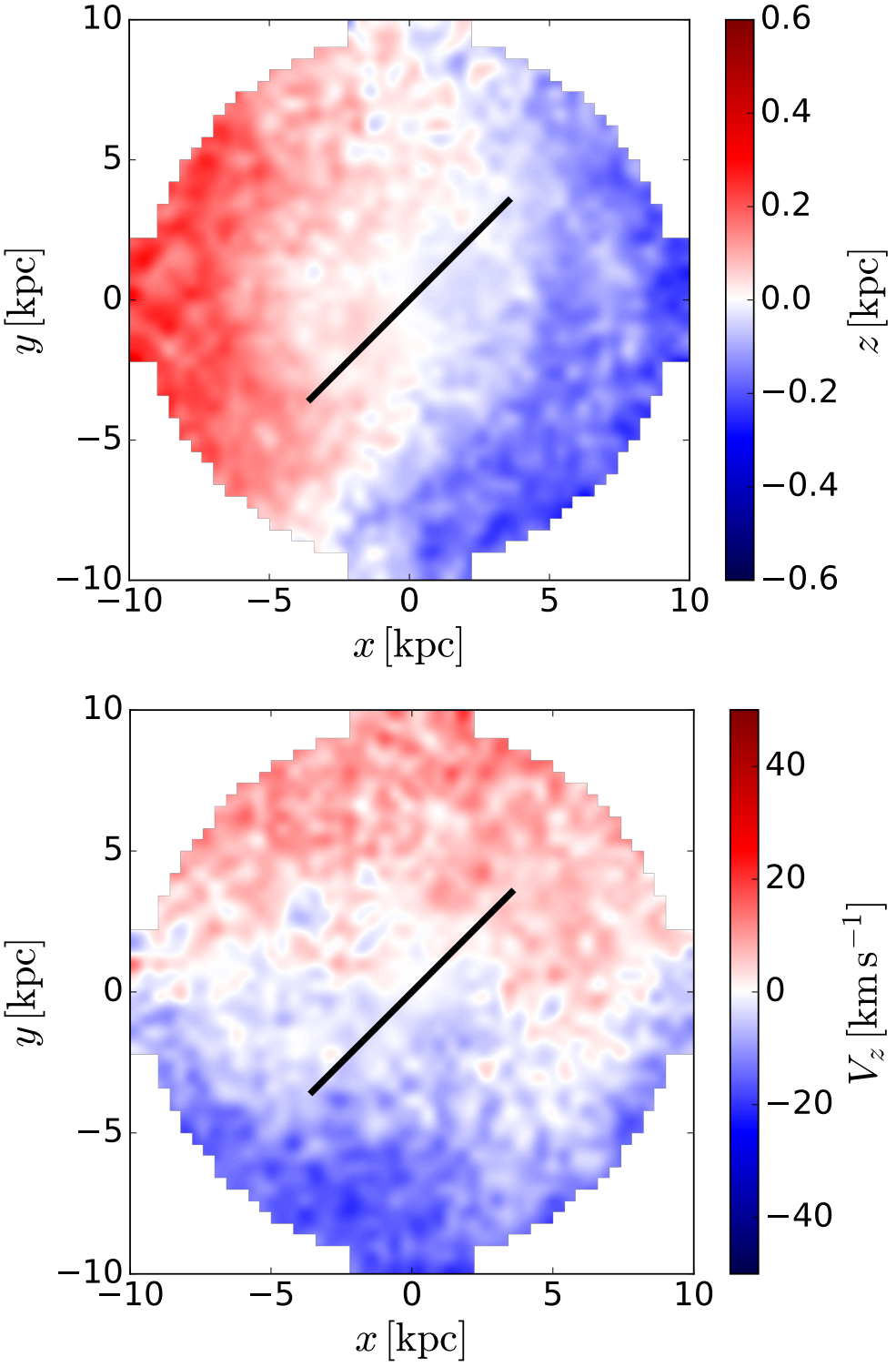


FIGURE 5.7: Mean vertical z position (top) and V_z velocity (bottom) of stars across the face-on projection of Auriga L8 for a snipshot near $z = 0$. In the top (bottom) panel, red indicates above the plane (towards the viewer) and blue indicates below the plane (away from the viewer). This is calculated for 50 bins in x and y and displayed with bicubic interpolation. In both panels, the black line corresponds to the length r_{A_2} and angle of the bar.

can see that this produces a net upwards velocity in the upper half of the disc and a net downwards velocity in the lower half.

After inclining the disc, a component of this vertical velocity is present in the LOS velocity. For slits below the x-axis in this example, this is away from the viewer, which leads to lower values of $\langle V_{\rm LOS} \rangle$; for slits above the x-axis, this is towards the viewer, which leads to higher values of $\langle V_{\rm LOS} \rangle$. As a result, the gradient of $\langle V_{\rm LOS} \rangle$ against $\langle X \rangle$ is increased, leading to an overestimate of the true pattern speed. Fig. 5.6 confirms that I overestimate the pattern speed at this 135° angle of the warp to the bar. A similar argument explains the overestimates when the warp is raised to the right instead. At intermediate angles, the vertical velocity contribution cancels out in $\langle V_{\rm LOS} \rangle$, hence the lower errors in $\Omega_{\rm TW}$.

Other parameters, such as those used in Chapter 4, show some correlation with absolute error in the TW method. However, this seems to be entirely driven by the discs with the highest warps (Aurigas 13, L3, 9, 20 and L8 from Fig. 5.5). Removing these five galaxies, in addition to Auriga 23 where the error in the TW method is known to be due to a double bar, leaves no significant remaining correlation between the errors in the TW method and other parameters.

5.3.2 Disc position angle

A warp in the disc of a galaxy typically begins at some radius within which the galaxy is relatively flat. However, one may notice in the upper panel of Fig. 5.7 that the red/blue colour gradient which indicates the disc not lying within the x-y plane extends to almost the centre. While this is certainly less pronounced within $3-4$ kpc, where the angle of the warp axis also changes orientation, this raises concerns for the measurement of this warp. In fact, each of the galaxies with the highest warps show a similar feature of the disc being misaligned almost all the way to the centre of the galaxy.

It is possible that this signifies a misalignment of the whole disc, rather than a genuine warp feature. If this is the case, then the results of Sec. 5.3.1 should be recontextualised as an investigation into the effect of position angle (PA) errors and inclination errors on

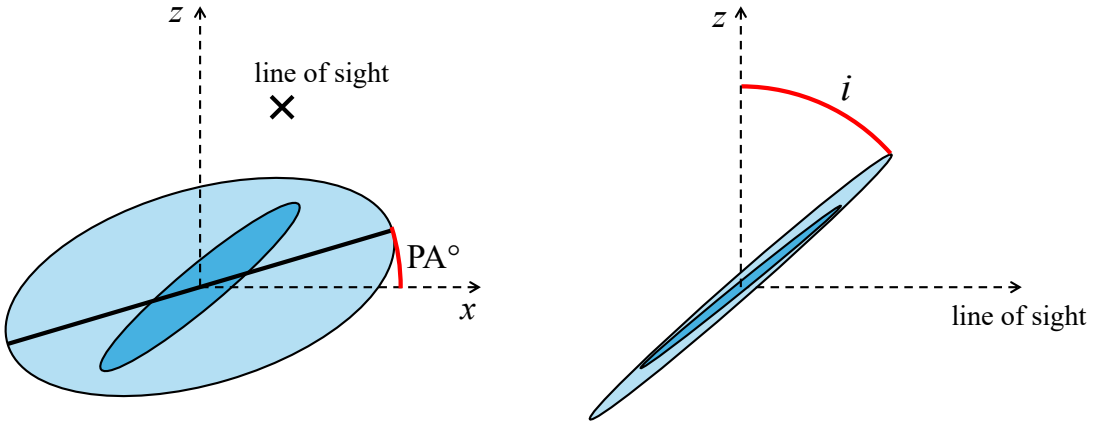


FIGURE 5.8: An illustration of the angles used when describing the view for the Tremaine-Weinberg method. In the left panel, the line of sight points into the page. The angle between the x-axis and the major axis of the ellipse formed on the plane of the sky by projection of the disc is the position angle (PA) and is shown by the red line. In the right panel, the line of sight points to the right. The angle of the disc plane to the z-axis is the inclination angle and is shown by the red curve.

the TW method, placing the studies of idealised simulations within Debattista (2003) and Zou et al. (2019) into a cosmological context.

To compare as directly as possible to these studies, I first note that my errors in disc alignment do not align with a pure PA error. The 'warps' that I measure are rotations from the disc plane prior to reorienting for the TW method, as shown in Fig. 5.4. In contrast, a PA error is confined to a rotation in the plane of the sky, illustrated in the left panel Fig. 5.8, and an inclination angle error is a miscalculation in the remaining rotation around the x-axis, shown in the right panel of the same figure. This means that an error in disc alignment represented as 'warp' angles can be effectively split into two components after rotation to a 45° inclination, depending on its angle to the viewer: an error in inclination angle and an error in PA. Note that any deviation in PA from the x-axis is an error, whereas I expect the inclination angle to be 45° (so errors in inclination manifest as a difference from 45°).

For a 'warp' axis angle $\Theta_{1,\mathrm{warp}}$ at 45° or −135° to the bar (i.e. in the line of sight), the misalignment is entirely confined to the inclination angle, with no error in the PA. This is since the disc is only misaligned by a rotation around the x-axis. These are also the 'warp' axis angles at which the TW method is relatively unaffected. The error being confined to the inclination angle also gives a second way to consider why these 'warp'

axis angles produce low errors in the TW method: since the TW method is valid at any inclination (except near 0° or 90°), it is only the $\frac{1}{\sin i}$ term which is affected by a change in inclination. At my chosen inclination of 45°, an error of 2° (the maximum 'warp' magnitude $\Phi_{1,\mathrm{warp}}$ in Fig. 5.5) produces less than 4% difference in this term, which is not sufficient to reach even the lowest errors in the TW method in the same figure. Using this as justification, I ignore the error in inclination angle in the following.

At 'warp' axis angles $\Theta_{1,\mathrm{warp}}$ of 135° or −45°, where I see the greatest TW method errors and the warp is most visible in the plane of the sky, the misalignment produces errors split across inclination and PA. For the small angle approximation $\sin\theta \simeq \theta$ (which is valid since I am considering angles less than 2°), this gives $\Delta i = \Delta\mathrm{PA} \simeq \frac{1}{\sqrt{2}}\Phi_{1,\mathrm{warp}}$. Thus I can convert my warp magnitude angles into maximum PA errors with a simple factor of $\sqrt{2}$.

Both Debattista (2003) and Zou et al. (2019) vary the PA error for an idealised simulation in increments and create a plot of the error in the TW method with respect to the error in disc PA. This is shown in Fig. 9 for Debattista (2003) and Fig. 13 for Zou et al. (2019). My Fig. 5.5 can be roughly interpreted as an equivalent figure, with the x-axis shrunk by a factor of $\sqrt{2}$ as calculated above to obtain PA. After this transformation, my PA errors thus range from $0° - 1.4°$, producing TW method errors above 30%. In these two previous studies, a similar range in PA errors, with a bar angle of 45°, leads to errors in the TW method of less than 20% in Debattista (2003) and less than 12% in Zou et al. (2019), significantly less than those I observe here.

This suggests two possible scenarios. It may be that PA errors in a cosmological context produce more of an effect on the TW method than in idealised simulations. However, the more likely scenario may be that the errors I find in this Chapter are the result of a combination of PA errors and genuine warps (or other effects like multiple disc populations) which arise due to the inherent chaos that a cosmological environment leads to.

5.4 Conclusions

In this Chapter, I applied the Tremaine-Weinberg (TW) method to 18 high temporal resolution reruns from the Auriga suite of magneto-hydrodynamical cosmological zoom-in simulations to compare the method to known pattern speeds of fast bars in a cosmological environment. In particular, I compared the error in the TW pattern speed estimates to the signature of S shaped warps (or possible position angle errors) in the disc.

I summarise my conclusions as follows:

- The TW method can be applied well to most bars in the simulation suite, achieving less than 10% errors in the majority of cases. This implies that the TW method is generally reliable in relatively isolated, single-barred, suitably inclined systems such as most of those simulated by Auriga.
- Applied to bars with true pattern speeds less than $25\,\mathrm{rad\,Gyr^{-1}}$, the TW method typically encounters much larger errors, up to 60% at some snipshots (excluding double-barred systems).
- Galaxies with a significant warp (at an angle of over 1° to the disc plane) produce increasing errors in the TW method. This acts as my largest source of error for five of the six bars with the largest total errors in the TW method.
- The errors in the TW method are highly dependent on the angle of the warp axis relative to the observer. For warps with their main axis along the line of sight there is little effect, but for warps with their main axis along the x axis, errors in the TW estimate are pronounced. This has the effect that the most noticeable warps, those visible in the plane of the sky, will impact observation the most.
- The warps may instead represent errors in the alignment of the galaxy disc. If so, this represents a mixture of inclination and position angle errors. For those warp angles which lead to a position angle error (again those visible in the plane of the sky), this leads to even greater errors in the TW method than previously found in the literature for isolated, idealised simulations.

The results of this study confirm that applying the TW method in a cosmological environment can carry greater errors than in idealised experiments. This is likely due to the complexity of discs which have been built and continuously altered by mergers, interactions, and accretion. Within the Auriga model, this may present as either warps which do significantly affect the applicability of the TW method, or as position angle errors being even more crucial than previously thought.

5.4.1 Future work

This Chapter has a natural follow-up of clarifying whether the warps found are genuine or represent an error in disc alignment. Since I intend for the research presented in this Chapter to form the basis of an upcoming published paper, this is work which I will carry out in my own future research.

I plan to thoroughly test the method by which I align my galaxies, using the median angular momentum vector for stars within an effective radius (as outlined in Sec. 2.2.1.1). This will involve comparing results when using the mean vector instead, when using different populations of stars (young versus old), when using different radii, when using gas instead of stars, and possibly when using the position of material rather than its angular momentum. If these variations to the method are mostly consistent, then the warp interpretation will be more likely. On the other hand, if these methods produce different results, or if one of the methods leads to a significant reduction in the calculated warp magnitude, then a disc misalignment will explain the results presented here.

In the latter case, I would subsequently be able to more precisely compare any remaining warp, in addition to the parameters used in Chapter 4, to the errors in the TW method. This may produce further results, leading to more information on when the TW method is best applicable in cosmologically motivated discs.

Chapter 6

Summary and Conclusions

Galactic bars drive secular evolution in disc galaxies (e.g. Sanders & Huntley, 1976; Matsuda & Nelson, 1977; Sellwood, 1980; Dehnen, 2000; Athanassoula et al., 2013; Cole et al., 2014), making them important structures to understand. However, this understanding is complicated by the variety of factors which can affect their formation and evolution: the dark matter halo (Tremaine & Weinberg, 1984a; Debattista & Sellwood, 2000) and its kinematics (Li et al., 2023), the dominance of baryons in the galaxy (Debattista & Sellwood, 1998; Athanassoula, 2003), the disc height (Klypin et al., 2009), the central matter concentration (Berentzen et al., 2007; Kataria & Das, 2019), the behaviour of gas in the disc (Villa-Vargas et al., 2010; Beane et al., 2023), and interactions with other galaxies (Athanassoula, 1996; Lang et al., 2014; Lokas et al., 2014; Kannan et al., 2015; Moetazedian et al., 2017). Additionally, cosmological simulations (where all of these factors can be considered at once) tend to produce bars slower than those observed (Algorry et al., 2017; Peschken & Lokas, 2019; Roshan et al., 2021; Habibi et al., 2024; Ansar et al., 2025). Therefore, a cosmological simulation suite which offers realistically fast bars provides the ideal environment for testing bar formation and evolution.

This is the focus of this thesis: I investigated the causes of bar formation, the factors affecting bar evolution, and the limitations of certain bar observations within the Auriga suite of cosmological magnetohydrodynamical zoom-in simulations (Grand et al., 2017,

2019), to better understand realistically fast bars (Fragkoudi et al., 2021) in Milky Way-mass disc galaxies. Below, I summarise the conclusions of Chapters 3, 4 and 5 in turn, and give an overview of the analysis which produced them.

6.1 Did GES form the Milky Way's bar?

In Chapter 3, I investigated a potential route to the formation of the Milky Way's bar through a case study of Auriga 18. This simulation has chemodynamic properties in the disc and bulge similar to the Milky Way (Fragkoudi et al., 2020) and a merger which leaves a radially biased and metal-rich stellar signature similar to that of the Gaia-Enceladus/Sausage (GES) as found in Belokurov et al. (2018) and Helmi et al. (2018) (Fattahi et al., 2019) and which occurs at a similar time (Belokurov et al., 2018; Helmi et al., 2018; Di Matteo et al., 2019; Gallart et al., 2019; Chaplin et al., 2020; Naidu et al., 2021). A bar also forms in this simulation at $9 - 8$ Gyr lookback time, matching estimates for the Milky Way bar from Bovy et al. (2019), Grady et al. (2020), Wylie et al. (2022), Sanders et al. (2024) and Schödel et al. (2023) as well as the time of the GES merger event; after this event, both the simulation and the real Milky Way have a quiescent merger history (Ruchti et al., 2015; Fragkoudi et al., 2020). These similarities mean that uncovering the cause of bar formation in Auriga 18 offers insight into bar formation in the Milky Way.

In Auriga 18, I concluded that tidal forces from the GES analogue form the bar through an inward-propagating perturbation starting in the outer disc. This bar is reinforced by inwards gas migration, which triggers a burst of star formation in the bar-forming region. To confirm this mechanism, I reran Auriga 18 with the progenitors of the GES analogue removed at $z = 4$. This leads to a delay in bar formation of over 2 Gyr, indicating that the merger does indeed trigger bar formation in the original. Later in its evolution, the rerun develops a less radially extended disc than the original, and even a polar disc in the final 2 Gyr of the simulation. I found that this is due to a misalignment of angular momentum in the newly accreting gas, which hints at potential further importance of

GES in the Milky Way, realigning the disc and allowing it to build in angular momentum and extent.

Also in this same Chapter, I explored the other halos in Auriga with a GES-like merger (as defined in Fattahi et al., 2019) and found that the oldest bars in the simulation suite all form with 1 Gyr of such a merger. Further, these bar-forming GES-like mergers each have stellar mass ratios to the main galaxy of less than 10%, suggesting that higher mass mergers disrupt the disc too much for bar formation, and implying that specific properties of the real GES merger were required to trigger bar formation in the Milky Way (rather than any merger being sufficient).

6.2 What drives bar rotation?

In Chapter 4, I used the high temporal resolution reruns from Sec. 2.1.2 to compare the bar rotation rates in Auriga to both galaxy properties and galaxy interaction histories. This aimed to identify the most important influences on bar rotation from their formation to present day, and whether the primary factors in determining bar rotation rates are internal properties of the host galaxy or external interactions with other galaxy halos.

I found that almost all bars in Auriga are not only fast in terms of rotation rate $\mathscr{R}$ (as seen in Fragkoudi et al., 2021), but speed up in $\mathscr{R}$ over the course of their evolution. This is in contrast to expectations from the literature surrounding dynamical friction, which should consistently slow bars down as they evolve. The primary reason for this appears to be the high baryon dominance of the Auriga galaxies, which is highly correlated to bar rotation rate at both bar formation and $z = 0$. High baryon dominance likely counters dynamical friction in most cases to allow the bar to remain fast and even speed up in $\mathscr{R}$ even if the pattern speed decreases. This also leads to galaxies with lower stellar masses hosting slower bars by $z = 0$, which has been observed in weak bars for $M_\star < 3 \times 10^{10} \mathrm{M}_\odot$ (Géron et al., 2023). Further observations to confirm the extent of this relation will act as a test of the cosmology and baryon physics used in Auriga.

Other bar properties also correlate with their rotation. I found that older bars in Auriga have a faster rotation rate by $z = 0$. However, rather than being due to the speed up observed above, this relation emerges almost immediately, with younger bars being slower than older bars within 0.5 Gyr of formation. Also at $z = 0$, I found that stronger bars tend to be faster rotators, a result which is confirmed in some, but not all, observational works which examine this (Rautiainen et al., 2008; Géron et al., 2023).

I found that galaxy interactions have only a secondary effect at most on pattern speeds across my sample. Stronger galaxy interactions around the bar formation time lead to slightly faster bars which have sped up more on average by $z = 0$. The mechanism by which galaxy interactions would affect bars at $z = 0$ but not at their bar formation time is unclear, but does contradict an expectation that tidally formed bars are slower (Miwa & Noguchi, 1998; Martinez-Valpuesta et al., 2017; Gajda et al., 2017; Bi et al., 2022). Galaxy interactions after the bar has formed have an even weaker speeding effect on bar rotation rates.

Taken together, these correlations suggest that internal galaxy properties, particularly baryon dominance, are the primary influence on bar rotation in Auriga. In combination with the observational tests on bar strength and stellar mass which I have mentioned, this could suggest that baryon dominance is the main factor setting bar rotation rates in approximately Milky Way-mass disc galaxies.

6.3 The reliability of the Tremaine-Weinberg method

In Chapter 5, I used the same simulations as in Chapter 4 to investigate how well the pattern speeds of these fast bars in baryon dominated galaxies can be observed with the Tremaine-Weinberg (TW) method. I applied the TW method to each of the barred galaxies from my sample, at each snipshot in which the galaxy is barred. I compared this to the previously calculated true pattern speed (the rate of change of angle of the bar) to uncover any effects which may lead to errors in the TW method.

I found the TW method to be generally accurate to within 10% of the true pattern speed, with six notable exceptions. The worst of these is Auriga 23, due to the presence of a double bar system. In the remaining five, I found a warp of more than 1° reaching to the inner regions of the disc. This appeared to be responsible for the errors in the TW method, with the most pronounced effect for warps visible in the plane of the sky; at other angles where the warp occurs along the line of sight, the asymmetry caused by vertical velocity components largely cancels itself out in the integral.

I also considered the possibility that these warps are in fact a misalignment of the whole disc, leading to errors in inclination angle and position angle. Under this assumption, I saw that inclination angle errors produced relatively small errors in the pattern speed, whereas position angle errors produced TW errors even larger than those seen in the literature for idealised simulations. In either case, warps or disc misalignment, the errors in the TW method are likely accentuated by the cosmological interactions which the disc experiences.

Appendix A

Comprehensive correlations

I present in Fig. A.1 an overview of the correlations existing between each of the parameters presented in Chapter 4. This includes interdependencies between each pair of parameters, in addition to the relations with pattern speed and rotation rate shown in the lower 4 rows. Each panel contains points for each relevant galaxy, a line of best fit, and a colour to indicate the strength of the correlation between the pair of parameters, with yellow as the most correlated and blue as the least. For example, the panel in the third column from the left and third row from the top shows the relation between the most strongly correlated pair of parameters, $M_\star$ and $\sigma(M)$ – as seen in Fig. 4.4 and explored further in Fragkoudi et al. (2025), galaxies in the Auriga simulations with higher stellar masses tend to lie further above the abundance matching relation from Moster et al. (2013). In contrast, the panel in the 5th column from the left and 6th row from the bottom shows the relation between the least correlated pair of parameters, $A_{2,\mathrm{max}}$ and $\frac{\Delta \frac{V_\star}{V_{\mathrm{all}}}|_{\mathrm{eff}}}{\frac{V_\star}{V_{\mathrm{all}}}|_{\mathrm{eff,i}}}$ – this indicates that the relative change in baryon dominance in the inner regions since the bar formed has no relation to the final strength of the bar.

In Chapter 4, I directly mention 6 of the relations shown here, outside of the focal relations with measures of bar speed. In Fig. A.1, these 6 relations are labelled (a)-(f) and each have a thick border. In Sec. 4.1.1 I refer to the weak correlation between t_{bar} and $\frac{\Delta \mathscr{R}}{\mathscr{R}_{\mathrm{i}}}$, shown in panel (f), as well as the positive correlation between $A_{2,\mathrm{max}}$ and t_{bar}, shown in panel (e). In Sec. 4.1.3 I refer to 4 relations. The positive correlation between $\log_{10} S_{\mathrm{form}}$ and t_{bar} is shown in panel (c). The weak positive correlation between $\frac{V_\star}{V_{\mathrm{all}}}|_{\mathrm{eff,i}}$

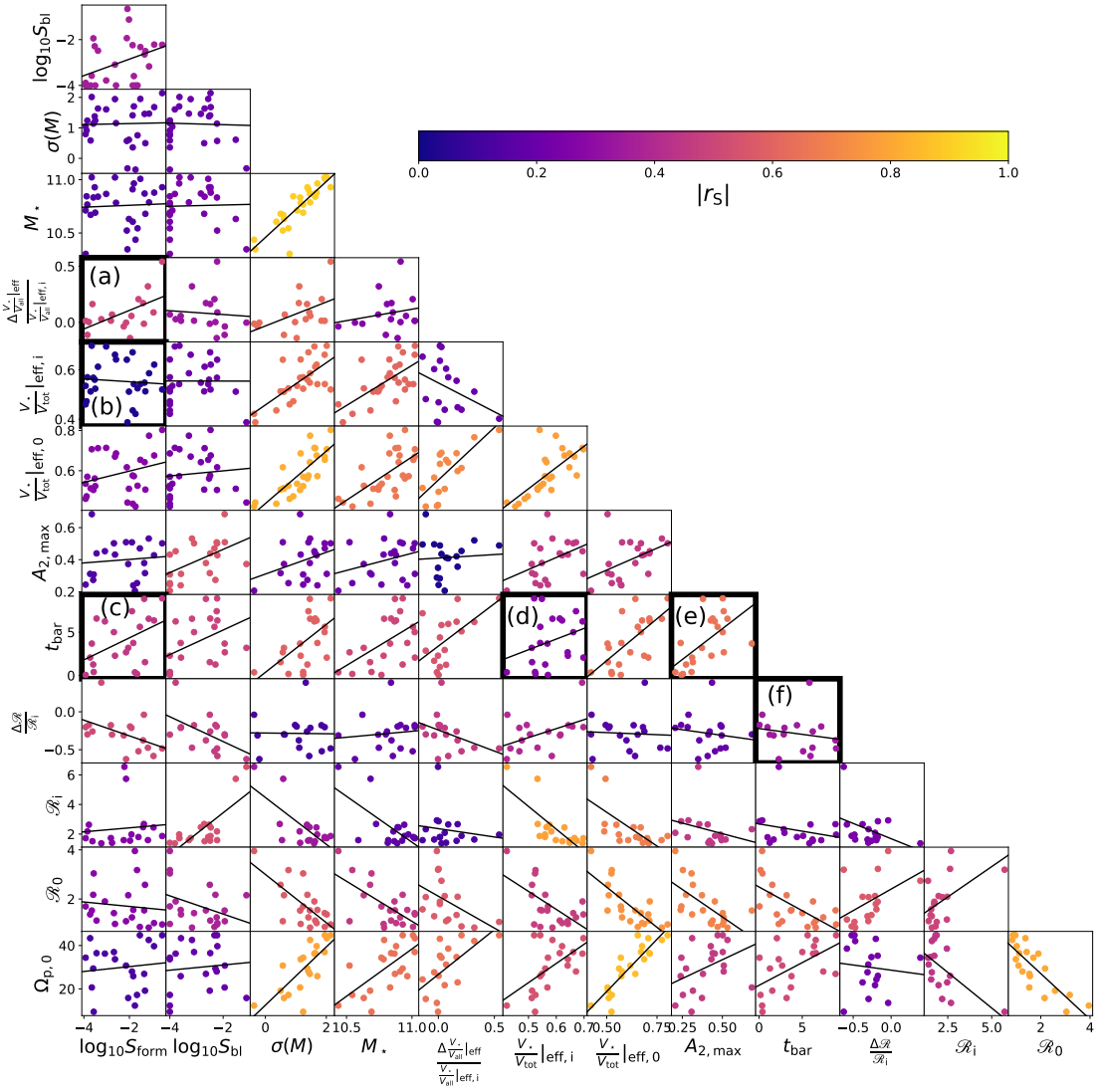


FIGURE A.1: Plots comparing, in pairs, the parameters shown in figures within Sec. 4.1: $\Omega_{p,0}$ the pattern speed at $z = 0$ in units of rad Gyr^{-1}; $\mathscr{R}_0$ the rotation rate at $z = 0$; $\mathscr{R}_i$ the rotation rate at time t_i; $\frac{\Delta\mathscr{R}}{\mathscr{R}_i}$ the fractional change in rotation rate from t_i until $z = 0$; t_{bar} the lookback time to bar formation in units of Gyr; $A_{2,max}$ the bar strength at $z = 0$; $\frac{V_\star}{V_{all}}|_{eff,0}$ the baryon dominance within the effective radius at $z = 0$; $\frac{V_\star}{V_{all}}|_{eff,i}$ the baryon dominance within the effective radius at t_i; $\frac{\Delta\frac{V_\star}{V_{all}}|_{eff}}{\frac{V_\star}{V_{all}}|_{eff,i}}$ the relative change in baryon dominance within the effective radius from t_i until $z = 0$; $M_\star$ the stellar mass in units of $M_\odot$; $\sigma(M)$ the vertical offset from the abundance matching relation in units of the 1σ dispersion in the relation (see Sec. 4.1.2.1); $\log_{10} S_{bl}$ the logarithm of the maximum interaction strength from t_i until $z = 0$; $\log_{10} S_{form}$ the logarithm of the maximum interaction strength from 1 Gyr before to 0.5 Gyr after t_{bar}. In each panel, I include all halos in my sample for which the parameters involved have a physical meaning (e.g. unbarred galaxies are not included in panels involving pattern speed). Each panel contains a linear line of best fit. The colours of points indicate the magnitude of the Spearman's rank correlation coefficient r_S between the two parameters in the panel, with high correlation in yellow and no correlation in blue. The 6 labelled panels with thick borders indicate the panels referred to from the main body of this paper.

and t_{bar} is shown in panel (d). The lack of correlation between $\log_{10} S_{\mathrm{form}}$ and $\frac{V_\star}{V_{\mathrm{all}}}|_{\mathrm{eff,i}}$ is shown in panel (b). Lastly, the positive relation between $\log_{10} S_{\mathrm{form}}$ and $\frac{\Delta \frac{V_\star}{V_{\mathrm{all}}}|_{\mathrm{eff}}}{\frac{V_\star}{V_{\mathrm{all}}}|_{\mathrm{eff,i}}}$, which is also referred to in Sec. 4.2.1, is shown in panel (a).

Bibliography

Aguerri J. A. L., et al., 2015, Astronomy & Astrophysics, 576, A102

Algorry D. G., et al., 2017, Monthly Notices of the Royal Astronomical Society, 469, 1054

Amvrosiadis A., et al., 2025, Monthly Notices of the Royal Astronomical Society, 537, 1163

Ann H. B., Park J.-C., 2006, New Astronomy, 11, 293

Ansar S., Pearson S., Sanderson R. E., Arora A., Hopkins P. F., Wetzel A., Cunningham E. C., Quinn J., 2025, The Astrophysical Journal, 978, 37

Antoja T., et al., 2014, Astronomy & Astrophysics, 563, A60

Asano T., Fujii M. S., Baba J., Bédorf J., Sellentin E., Portegies Zwart S., 2020, Monthly Notices of the Royal Astronomical Society, 499, 2416

Athanassoula E., 1996, in Buta R., Crocker D. A., Elmegreen B. G., eds, Astronomical Society of the Pacific Conference Series Vol. 91, IAU Colloquium 157: Barred Galaxies. p. 309

Athanassoula E., 2002, The Astrophysical Journal, 569, L83

Athanassoula E., 2003, Monthly Notices of the Royal Astronomical Society, 341, 1179

Athanassoula E., 2008, Monthly Notices of the Royal Astronomical Society, 390, L69

Athanassoula E., 2014, Monthly Notices of the Royal Astronomical Society, 438, L81

Athanassoula E., Sellwood J. A., 1986, Monthly Notices of the Royal Astronomical Society, 221, 213

Athanassoula E., Machado R. E. G., Rodionov S. A., 2013, Monthly Notices of the Royal Astronomical Society, 429, 1949

Baba J., Kawata D., 2020, Monthly Notices of the Royal Astronomical Society, 492, 4500

Beane A., et al., 2023, The Astrophysical Journal, 953, 173

Belokurov V., Erkal D., Evans N. W., Koposov S. E., Deason A. J., 2018, Monthly Notices of the Royal Astronomical Society, 478, 611

Belokurov V., Sanders J. L., Fattahi A., Smith M. C., Deason A. J., Evans N. W., Grand R. J. J., 2020, Monthly Notices of the Royal Astronomical Society, 494, 3880

Berentzen I., Shlosman I., Martinez-Valpuesta I., Heller C. H., 2007, The Astrophysical Journal, 666, 189

Bi D., Shlosman I., Romano-Díaz E., 2022, The Astrophysical Journal, 934, 52

Binney J., 1977, The Astrophysical Journal, 215, 483

Binney J., Tremaine S., 1988, Galactic Dynamics. Princeton University Press

Bissantz N., Gerhard O., 2002, Monthly Notices of the Royal Astronomical Society, 330, 591

Bissantz N., Englmaier P., Gerhard O., 2003, Monthly Notices of the Royal Astronomical Society, 340, 949

Borodina O., Williams T. G., Sormani M. C., Meidt S., Schinnerer E., 2023, Monthly Notices of the Royal Astronomical Society, 524, 3437

Bournaud F., Combes F., 2002, Astronomy & Astrophysics, 392, 83

Bournaud F., Combes F., Semelin B., 2005, Monthly Notices of the Royal Astronomical Society, 364, L18

Bovy J., Leung H. W., Hunt J. A. S., Mackereth J. T., García-Hernández D. A., Roman-Lopes A., 2019, Monthly Notices of the Royal Astronomical Society, 490, 4740

Briggs F. H., 1990, The Astrophysical Journal, 352, 15

Brook C. B., Kawata D., Gibson B. K., Flynn C., 2003, The Astrophysical Journal, 585, L125

Brook C., Richard S., Kawata D., Martel H., Gibson B. K., 2007, The Astrophysical Journal, 658, 60

Brunetti M., Chiappini C., Pfenniger D., 2011, Astronomy & Astrophysics, 534, A75

Bundy K., et al., 2015, The Astrophysical Journal, 798, 7

Buta R. J., Zhang X., 2009, The Astrophysical Journal Supplemental Series, 182, 559

Buta R. J., et al., 2015, The Astrophysical Journal Supplemental Series, 217, 32

Buttitta C., et al., 2023, Monthly Notices of the Royal Astronomical Society, 521, 2227

Canzian B., 1993, The Astrophysical Journal, 414, 487

Cavanagh M. K., Bekki K., Groves B. A., Pfeffer J., 2022, Monthly Notices of the Royal Astronomical Society, 510, 5164

Chabrier G., 2003, Publications of the Astronomical Society of the Pacific, 115, 763

Chaplin W. J., et al., 2020, Nature Astronomy, 4, 382

Clarke J. P., Gerhard O., 2022, Monthly Notices of the Royal Astronomical Society, 512, 2171

Cole A. A., Weinberg M. D., 2002, The Astrophysical Journal, 574, L43

Cole S., Aragon-Salamanca A., Frenk C. S., Navarro J. F., Zepf S. E., 1994, Monthly Notices of the Royal Astronomical Society, 271, 781

Cole D. R., Debattista V. P., Erwin P., Earp S. W. F., Roškar R., 2014, Monthly Notices of the Royal Astronomical Society, 445, 3352

Collier A., Shlosman I., Heller C., 2018, Monthly Notices of the Royal Astronomical Society, 476, 1331

Combes F., Elmegreen B. G., 1993, Astronomy & Astrophysics, 271, 391

Conselice C. J., 2014, Annual Review of Astronomy and Astrophysics, 52, 291

Contopoulos G., 1980, Astronomy & Astrophysics, 81, 198

Contopoulos G., Mertzanides C., 1977, Astronomy & Astrophysics, 61, 477

Corsini E. M., 2011, Memorie della Societa Astronomica Italiana Supplementi, 18, 23

Crain R. A., et al., 2015, Monthly Notices of the Royal Astronomical Society, 450, 1937

Cuomo V., Lopez Aguerri J. A., Corsini E. M., Debattista V. P., Méndez-Abreu J., Pizzella A., 2019, Astronomy & Astrophysics, 632, A51

Cuomo V., Aguerri J. A. L., Corsini E. M., Debattista V. P., 2020, Astronomy & Astrophysics, 641, A111

Cuomo V., Lee Y. H., Buttitta C., Aguerri J. A. L., Corsini E. M., Morelli L., 2021, Astronomy & Astrophysics, 649, A30

D'Onghia E., Vogelsberger M., Faucher-Giguere C.-A., Hernquist L., 2010, The Astrophysical Journal, 725, 353

Deason A. J., Belokurov V., Sanders J. L., 2019, Monthly Notices of the Royal Astronomical Society, 490, 3426

Debattista V. P., 2003, Monthly Notices of the Royal Astronomical Society, 342, 1194

Debattista V. P., Sellwood J. A., 1998, The Astrophysical Journal, 493, L5

Debattista V. P., Sellwood J. A., 2000, The Astrophysical Journal, 543, 704

Dehnen W., 2000, The Astronomical Journal, 119, 800

Di Matteo P., Haywood M., Lehnert M. D., Katz D., Khoperskov S., Snaith O. N., Gómez A., Robichon N., 2019, Astronomy & Astrophysics, 632, A4

Dillamore A. M., Belokurov V., Evans N. W., 2024, Monthly Notices of the Royal Astronomical Society, 532, 4389

Dubois Y., et al., 2021, Astronomy & Astrophysics, 651, A109

Dzyuba B. M., Yakubov V. B., 1970, Soviet Astronomy, 14, 1

Efstathiou G., Lake G., Negroponte J., 1982, Monthly Notices of the Royal Astronomical Society, 199, 1069

Elmegreen B. G., Elmegreen D. M., Seiden P. E., 1989, The Astrophysical Journal, 343, 602

Elmegreen D. M., Sundin M., Elmegreen B., Sundelius B., 1991, Astronomy & Astrophysics, 244, 52

Elmegreen B. G., Elmegreen D. M., Knapen J. H., Buta R. J., Block D. L., Puerari I., 2007, The Astrophysical Journal, 670, L97

Erwin P., 2018, Monthly Notices of the Royal Astronomical Society, 474, 5372

Eskridge P. B., et al., 2000, The Astronomical Journal, 119, 536

Eskridge P. B., et al., 2002, The Astrophysical Journal Supplemental Series, 143, 73

Euclid Collaboration et al., 2025, Astronomy & Astrophysics, 697, A5

Fall S. M., Efstathiou G., 1980, Monthly Notices of the Royal Astronomical Society, 193, 189

Fathi K., Beckman J. E., Piñol-Ferrer N., Hernandez O., Martínez-Valpuesta I., Carignan C., 2009, The Astrophysical Journal, 704, 1657

Fattahi A., et al., 2016, Monthly Notices of the Royal Astronomical Society, 457, 844

Fattahi A., et al., 2019, Monthly Notices of the Royal Astronomical Society, 484, 4471

Faucher-Giguère C.-A., Lidz A., Zaldarriaga M., Hernquist L., 2009, The Astrophysical Journal, 703, 1416

Feuillet D. K., Feltzing S., Sahlholdt C. L., Casagrande L., 2020, Monthly Notices of the Royal Astronomical Society, 497, 109

Fragkoudi F., et al., 2020, Monthly Notices of the Royal Astronomical Society, 494, 5936

Fragkoudi F., Grand R. J. J., Pakmor R., Springel V., White S. D. M., Marinacci F., Gomez F. A., Navarro J. F., 2021, Astronomy & Astrophysics, 650, L16

Fragkoudi F., Grand R. J. J., Pakmor R., Gómez F., Marinacci F., Springel V., 2025, Monthly Notices of the Royal Astronomical Society, 538, 1587

Frankel N., et al., 2022, The Astrophysical Journal, 940, 61

Frosst M., Obreschkow D., Ludlow A., Bottrell C., Genel S., 2025, Monthly Notices of the Royal Astronomical Society, 537, 3543

Frosst M., Obreschkow D., Ludlow A., Fraser-McKelvie A., 2026, Monthly Notices of the Royal Astronomical Society, 547, stag428

Gadotti D. A., 2011, Monthly Notices of the Royal Astronomical Society, 415, 3308

Gadotti D. A., Seidel M. K., Sánchez-Blázquez P., Falcón-Barroso J., Husemann B., Coelho P., Pérez I., 2015, Astronomy & Astrophysics, 584, A90

Gaia Collaboration et al., 2016, Astronomy & Astrophysics, 595, A1

Gaia Collaboration et al., 2023, Astronomy & Astrophysics, 674, A1

Gajda G., Lokas E. L., Athanassoula E., 2017, The Astrophysical Journal, 842, 56

Gallart C., Bernard E. J., Brook C. B., Ruiz-Lara T., Cassisi S., Hill V., Monelli M., 2019, Nature Astronomy, 3, 932

García-Benito R., et al., 2015, Astronomy & Astrophysics, 576, A135

Garma-Oehmichen L., Cano-Díaz M., Hernández-Toledo H., Aquino-Ortíz E., Valenzuela O., Aguerri J. A. L., Sánchez S. F., Merrifield M., 2020, Monthly Notices of the Royal Astronomical Society, 491, 3655

Garma-Oehmichen L., et al., 2022, Monthly Notices of the Royal Astronomical Society, 517, 5660

Gerin M., Combes F., Athanassoula E., 1990, Astronomy & Astrophysics, 230, 37

Géron T., et al., 2023, Monthly Notices of the Royal Astronomical Society, 521, 1775

Géron T., et al., 2025, The Astrophysical Journal, 987, 74

Ghafourian N., Roshan M., Abbassi S., 2020, The Astrophysical Journal, 895, 13

Ghosh S., Di Matteo P., 2024, Astronomy & Astrophysics, 683, A100

Gómez F. A., White S. D. M., Grand R. J. J., Marinacci F., Springel V., Pakmor R., 2017, Monthly Notices of the Royal Astronomical Society, 465, 3446

Gowanlock M. G., Patton D. R., McConnell S. M., 2011, Astrobiology, 11, 855

Grady J., Belokurov V., Evans N. W., 2020, Monthly Notices of the Royal Astronomical Society, 492, 3128

Grand R. J. J., et al., 2017, Monthly Notices of the Royal Astronomical Society, 467, 179

Grand R. J. J., et al., 2018, Monthly Notices of the Royal Astronomical Society, 474, 3629

Grand R. J. J., et al., 2019, Monthly Notices of the Royal Astronomical Society, 490, 4786

Grand R. J. J., et al., 2020, Monthly Notices of the Royal Astronomical Society, 497, 1603

Grand R. J. J., Fragkoudi F., Gómez F. A., Jenkins A., Marinacci F., Pakmor R., Springel V., 2024, Monthly Notices of the Royal Astronomical Society, 532, 1814

Guo R., Mao S., Athanassoula E., Li H., Ge J., Long R. J., Merrifield M., Masters K., 2019, Monthly Notices of the Royal Astronomical Society, 482, 1733

Guo Y., et al., 2025, The Astrophysical Journal, 985, 181

Habibi A., Roshan M., Hosseinirad M., Khosroshahi H., Aguerri J. A. L., Cuomo V., Abbassi S., 2024, Astronomy & Astrophysics, 691, A122

Hasan H., Norman C., 1990, The Astrophysical Journal, 361, 69

Hawarden T. G., Mountain C. M., Leggett S. K., Puxley P. J., 1986, Monthly Notices of the Royal Astronomical Society, 221, 41P

Haywood M., Di Matteo P., Lehnert M. D., Snaith O., Khoperskov S., Gómez A., 2018, The Astrophysical Journal, 863, 113

Hehl F. W., Mashhoon B., 2009, Physics Letters B, 673, 279

Helmi A., Babusiaux C., Koppelman H. H., Massari D., Veljanoski J., Brown A. G. A., 2018, Nature, 563, 85

Hernquist L., Weinberg M. D., 1992, The Astrophysical Journal, 400, 80

Hilmi T., et al., 2020, Monthly Notices of the Royal Astronomical Society, 497, 933

Hirashima K., et al., 2025, arXiv e-prints, p. arXiv:2510.23330

Hohl F., 1971, The Astrophysical Journal, 168, 343

Hohl F., 1976, The Astronomical Journal, 81, 30

Holmberg E., 1941, The Astrophysical Journal, 94, 385

Hopkins P. F., et al., 2018, Monthly Notices of the Royal Astronomical Society, 480, 800

Hoyle F., 1953, The Astrophysical Journal, 118, 513

Huang S., Carlberg R. G., 1997, The Astrophysical Journal, 480, 503

Hubble E. P., 1926, The Astrophysical Journal, 64, 321

Hubble E. P., 1936, Realm of the Nebulae. Yale University Press

Huertas-Company M., et al., 2025, Astronomy & Astrophysics, 704, A94

Hunt J. A. S., Vasiliev E., 2025, New Astronomy Reviews, 100, 101721

Hunt J. A. S., Hong J., Bovy J., Kawata D., Grand R. J. J., 2018, Monthly Notices of the Royal Astronomical Society, 481, 3794

Hunter Jr. J. H., Ball R., Huntley J. M., England M. N., Gottesman S. T., 1988, The Astrophysical Journal, 324, 721

Irodotou D., et al., 2022, Monthly Notices of the Royal Astronomical Society, 513, 3768

Jiménez-Arranz Ó., Roca-Fàbrega S., 2025, Astronomy & Astrophysics, 698, L7

Jin Y., Zhu L., Tahmasebzadeh B., Mao S., van de Ven G., Guo R., Cai R., 2025, Astronomy & Astrophysics, 700, A249

Kannan R., Macciò A. V., Fontanot F., Moster B. P., Karman W., Somerville R. S., 2015, Monthly Notices of the Royal Astronomical Society, 452, 4347

Karakas A. I., 2010, Monthly Notices of the Royal Astronomical Society, 403, 1413

Kataria S. K., Das M., 2018, Monthly Notices of the Royal Astronomical Society, 475, 1653

Kataria S. K., Das M., 2019, The Astrophysical Journal, 886, 43

Kawata D., Baba J., Hunt J. A. S., Schönrich R., Ciucă I., Friske J., Seabroke G., Cropper M., 2021, Monthly Notices of the Royal Astronomical Society, 508, 728

Kelly A. J., Jenkins A., Deason A., Fattahi A., Grand R. J. J., Pakmor R., Springel V., Frenk C. S., 2022, Monthly Notices of the Royal Astronomical Society, 514, 3113

Kennicutt Jr. R. C., 1998, Annual Review of Astronomy and Astrophysics, 36, 189

Khalil Y. R., et al., 2025, Astronomy & Astrophysics, 699, A263

Khoperskov S., Minchev I., Steinmetz M., Ratcliffe B., Walcher J. C., Libeskind N. I., 2024, Monthly Notices of the Royal Astronomical Society, 533, 3975

Kim J. H., Peirani S., Kim S., Ann H. B., An S.-H., Yoon S.-J., 2014, The Astrophysical Journal, 789, 90

Klypin A., Valenzuela O., Colín P., Quinn T., 2009, Monthly Notices of the Royal Astronomical Society, 398, 1027

Kraljic K., Bournaud F., Martig M., 2012, The Astrophysical Journal, 757, 60

Kranz T., Slyz A., Rix H.-W., 2003, The Astrophysical Journal, 586, 143

Kuno N., Nishiyama K., Nakai N., Sorai K., Vila-Vilaró B., Handa T., 2000, Publications of the Astronomical Society of Japan, 52, 775

Lane J. M. M., Bovy J., Mackereth J. T., 2023, Monthly Notices of the Royal Astronomical Society, 526, 1209

Lang M., Holley-Bockelmann K., Sinha M., 2014, The Astrophysical Journal, 790, L33

Le Conte Z. A., et al., 2024, Monthly Notices of the Royal Astronomical Society, 530, 1984

Le Conte Z. A., et al., 2026, Monthly Notices of the Royal Astronomical Society, 545, staf2010

Lee J. H., Park C., Hwang H. S., Kwon M., 2024, The Astrophysical Journal, 966, 113

Lelli F., McGaugh S. S., Schombert J. M., 2016, The Astronomical Journal, 152, 157

Li X., Shlosman I., Heller C., Pfenniger D., 2023, Monthly Notices of the Royal Astronomical Society, 526, 1972

Lintott C. J., et al., 2008, Monthly Notices of the Royal Astronomical Society, 389, 1179

Little B., Carlberg R. G., 1991, Monthly Notices of the Royal Astronomical Society, 250, 161

Lokas E. L., 2018, The Astrophysical Journal, 857, 6

Lokas E. L., Athanassoula E., Debattista V. P., Valluri M., Pino A. d., Semczuk M., Gajda G., Kowalczyk K., 2014, Monthly Notices of the Royal Astronomical Society, 445, 1339

López-Corredoira M., Cabrera-Lavers A., Mahoney T. J., Hammersley P. L., Garzón F., González-Fernández C., 2007, The Astronomical Journal, 133, 154

Lucchini S., D'Onghia E., Aguerri J. A. L., 2024, Monthly Notices of the Royal Astronomical Society, 531, L14

Mackereth J. T., et al., 2019, Monthly Notices of the Royal Astronomical Society, 482, 3426

Marasco A., Posti L., Oman K., Famaey B., Cresci G., Fraternali F., 2020, Astronomy & Astrophysics, 640, A70

Marinacci F., Pakmor R., Springel V., 2014, Monthly Notices of the Royal Astronomical Society, 437, 1750

Marinacci F., et al., 2018, Monthly Notices of the Royal Astronomical Society, 480, 5113

Marinova I., Jogee S., 2007, The Astrophysical Journal, 659, 1176

Martinez-Valpuesta I., Shlosman I., Heller C., 2006, The Astrophysical Journal, 637, 214

Martinez-Valpuesta I., Aguerri J. A. L., González-García A. C., Dalla Vecchia C., Stringer M., 2017, Monthly Notices of the Royal Astronomical Society, 464, 1502

Matsuda T., Nelson A. H., 1977, Nature, 266, 607

Meidt S. E., Rand R. J., Merrifield M. R., Debattista V. P., Shen J., 2008, The Astrophysical Journal, 676, 899

Menéndez-Delmestre K., Sheth K., Schinnerer E., Jarrett T. H., Scoville N. Z., 2007, The Astrophysical Journal, 657, 790

Merrifield M. R., Rand R. J., Meidt S. E., 2006, Monthly Notices of the Royal Astronomical Society, 366, L17

Milgrom M., 1983, The Astrophysical Journal, 270, 365

Miller R. H., Prendergast K. H., Quirk W. J., 1970, The Astrophysical Journal, 161, 903

Minchev I., Famaey B., 2010, The Astrophysical Journal, 722, 112

Miwa T., Noguchi M., 1998, The Astrophysical Journal, 499, 149

Mo H. J., Mao S., White S. D. M., 1998, Monthly Notices of the Royal Astronomical Society, 295, 319

Mo H., van den Bosch F. C., White S., 2010, Galaxy Formation and Evolution. Cambridge University Press, doi:10.1017/CBO9780511807244

Moetazedian R., Polyachenko E. V., Berczik P., Just A., 2017, Astronomy & Astrophysics, 604, A75

Moffat J. W., 2006, Journal of Cosmology and Astroparticle Physics, 2006, 004

Monari G., Famaey B., Siebert A., Wegg C., Gerhard O., 2019, Astronomy & Astrophysics, 626, A41

Moster B. P., Naab T., White S. D. M., 2013, Monthly Notices of the Royal Astronomical Society, 428, 3121

Nagesh S. T., et al., 2023, Monthly Notices of the Royal Astronomical Society, 519, 5128

Naidu R. P., et al., 2021, The Astrophysical Journal, 923, 92

Naidu R. P., et al., 2026, The Open Journal of Astrophysics, 9, 56033

Naiman J. P., et al., 2018, Monthly Notices of the Royal Astronomical Society, 477, 1206

Nelson D., et al., 2018, Monthly Notices of the Royal Astronomical Society, 475, 624

Nelson D., et al., 2019, Monthly Notices of the Royal Astronomical Society, 490, 3234

Nepal S., et al., 2024, Astronomy & Astrophysics, 681, L8

Ness M., et al., 2013, Monthly Notices of the Royal Astronomical Society, 432, 2092

Noguchi M., 1987, Monthly Notices of the Royal Astronomical Society, 228, 635

Nogueras-Lara F., et al., 2020, Nature Astronomy, 4, 377

O'Neill J. K., Dubinski J., 2003, Monthly Notices of the Royal Astronomical Society, 346, 251

Okamoto T., Frenk C. S., Jenkins A., Theuns T., 2010, Monthly Notices of the Royal Astronomical Society, 406, 208

Ostriker J. P., Peebles P. J. E., 1973, The Astrophysical Journal, 186, 467

Pakmor R., Marinacci F., Springel V., 2014, The Astrophysical Journal, 783, L20

Pakmor R., Springel V., Bauer A., Mocz P., Munoz D. J., Ohlmann S. T., Schaal K., Zhu C., 2016, Monthly Notices of the Royal Astronomical Society, 455, 1134

Pakmor R., et al., 2017, Monthly Notices of the Royal Astronomical Society, 469, 3185

Paturel G., Dubois P., Petit C., Woelfel F., 2002, LEDA, p. 0

Pérez-Villegas A., Portail M., Wegg C., Gerhard O., 2017, The Astrophysical Journal, 840, L2

Peschken N., Lokas E. L., 2019, Monthly Notices of the Royal Astronomical Society, 483, 2721

Peters III W. L., 1975, The Astrophysical Journal, 195, 617

Pettitt A. R., Wadsley J. W., 2018, Monthly Notices of the Royal Astronomical Society, 474, 5645

Pillepich A., et al., 2018, Monthly Notices of the Royal Astronomical Society, 475, 648

Pillepich A., et al., 2019, Monthly Notices of the Royal Astronomical Society, 490, 3196

Planck Collaboration et al., 2014, Astronomy & Astrophysics, 571, A16

Portinari L., Chiosi C., Bressan A., 1998, Astronomy & Astrophysics, 334, 505

Posti L., Fraternali F., Marasco A., 2019, Astronomy & Astrophysics, 626, A56

Quillen A. C., Dougherty J., Bagley M. B., Minchev I., Comparetta J., 2011, Monthly Notices of the Royal Astronomical Society, 417, 762

Quinn T., Binney J., 1992, Monthly Notices of the Royal Astronomical Society, 255, 729

Ramos P., Antoja T., Figueras F., 2018, Astronomy & Astrophysics, 619, A72

Rand R. J., Wallin J. F., 2004, The Astrophysical Journal, 614, 142

Rautiainen P., Salo H., Laurikainen E., 2008, Monthly Notices of the Royal Astronomical Society, 388, 1803

Reddish J., et al., 2022, Monthly Notices of the Royal Astronomical Society, 512, 160

Reshetnikov V. P., Mosenkov A. V., Moiseev A. V., Kotov S. S., Savchenko S. S., 2016, Monthly Notices of the Royal Astronomical Society, 461, 4233

Rey M. P., et al., 2023, Monthly Notices of the Royal Astronomical Society, 521, 995

Robin A. C., Marshall D. J., Schultheis M., Reylé C., 2012, Astronomy & Astrophysics, 538, A106

Rodriguez-Fernandez N. J., Combes F., 2008, Astronomy & Astrophysics, 489, 115

Romano-Díaz E., Shlosman I., Heller C., Hoffman Y., 2008, The Astrophysical Journal, 687, L13

Romeo A. B., Agertz O., Renaud F., 2023, Monthly Notices of the Royal Astronomical Society, 518, 1002

Rosas-Guevara Y., et al., 2020, Monthly Notices of the Royal Astronomical Society, 491, 2547

Rosas-Guevara Y., et al., 2022, Monthly Notices of the Royal Astronomical Society, 512, 5339

Roshan M., 2018, The Astrophysical Journal, 854, 38

Roshan M., Rahvar S., 2019, The Astrophysical Journal, 872, 6

Roshan M., Ghafourian N., Kashfi T., Banik I., Haslbauer M., Cuomo V., Famaey B., Kroupa P., 2021, Monthly Notices of the Royal Astronomical Society, 508, 926

Roshan M., et al., 2025, Astronomy & Astrophysics, 701, A160

Roškar R., Debattista V. P., Brooks A. M., Quinn T. R., Brook C. B., Governato F., Dalcanton J. J., Wadsley J., 2010, Monthly Notices of the Royal Astronomical Society, 408, 783

Rubin V. C., Ford Jr. W. K., Thonnard N., 1978, The Astrophysical Journal, 225, L107

Ruchti G. R., et al., 2015, Monthly Notices of the Royal Astronomical Society, 450, 2874

Saha K., Naab T., 2013, Monthly Notices of the Royal Astronomical Society, 434, 1287

Sakamoto K., Okumura S. K., Ishizuki S., Scoville N. Z., 1999, The Astrophysical Journal, 525, 691

Salo H., Rautiainen P., Buta R., Purcell G. B., Cobb M. L., Crocker D. A., Laurikainen E., 1999, The Astronomical Journal, 117, 792

Sánchez S. F., et al., 2012, Astronomy & Astrophysics, 538, A8

Sanders R. H., Huntley J. M., 1976, The Astrophysical Journal, 209, 53

Sanders J. L., Smith L., Evans N. W., 2019, Monthly Notices of the Royal Astronomical Society, 488, 4552

Sanders J. L., Kawata D., Matsunaga N., Sormani M. C., Smith L. C., Minniti D., Gerhard O., 2024, Monthly Notices of the Royal Astronomical Society, 530, 2972

Sawala T., et al., 2016, Monthly Notices of the Royal Astronomical Society, 457, 1931

Schaye J., et al., 2015, Monthly Notices of the Royal Astronomical Society, 446, 521

Schödel R., et al., 2023, Astronomy & Astrophysics, 672, L8

Schwarz M. P., 1984, Monthly Notices of the Royal Astronomical Society, 209, 93

Schwarzkopf U., Dettmar R.-J., 2001, Astronomy & Astrophysics, 373, 402

Sellwood J. A., 1980, Astronomy & Astrophysics, 89, 296

Sellwood J. A., 1996, The Astrophysical Journal, 473, 733

Sellwood J. A., 2016, The Astrophysical Journal, 819, 92

Sellwood J. A., Debattista V. P., 2006, The Astrophysical Journal, 639, 868

Sellwood J. A., Evans N. W., 2001, The Astrophysical Journal, 546, 176

Semczuk M., Dehnen W., Schönrich R., Athanassoula E., 2024, Astronomy & Astrophysics, 692, A159

Sempere M. J., Garcia-Burillo S., Combes F., Knapen J. H., 1995, Astronomy & Astrophysics, 296, 45

Seo W.-Y., Kim W.-T., Kwak S., Hsieh P.-Y., Han C., Hopkins P. F., 2019, The Astrophysical Journal, 872, 5

Shen J., Sellwood J. A., 2006, Monthly Notices of the Royal Astronomical Society, 370, 2

Sheth K., Vogel S. N., Regan M. W., Thornley M. D., Teuben P. J., 2005, The Astrophysical Journal, 632, 217

Sheth K., et al., 2008, The Astrophysical Journal, 675, 1141

Shlosman I., Noguchi M., 1993, The Astrophysical Journal, 414, 474

Simkin S. M., Su H. J., Schwarz M. P., 1980, The Astrophysical Journal, 237, 404

Sormani M. C., Binney J., Magorrian J., 2015, Monthly Notices of the Royal Astronomical Society, 454, 1818

Sparke L. S., Casertano S., 1988, Monthly Notices of the Royal Astronomical Society, 234, 873

Sparke L. S., Sellwood J. A., 1987, Monthly Notices of the Royal Astronomical Society, 225, 653

Springel V., 2010, Monthly Notices of the Royal Astronomical Society, 401, 791

Springel V., Hernquist L., 2003, Monthly Notices of the Royal Astronomical Society, 339, 289

Springel V., Di Matteo T., Hernquist L., 2005, Monthly Notices of the Royal Astronomical Society, 361, 776

Springel V., et al., 2018, Monthly Notices of the Royal Astronomical Society, 475, 676

Springel V., Pakmor R., Zier O., Reinecke M., 2021, Monthly Notices of the Royal Astronomical Society, 506, 2871

Sundin M., Donner K. J., Sundelius B., 1993, Astronomy & Astrophysics, 280, 105

Tagger M., Sygnet J. F., Athanassoula E., Pellat R., 1987, The Astrophysical Journal, 318, L43

Tahmasebzadeh B., Zhu L., Shen J., Gerhard O., van de Ven G., 2022, The Astrophysical Journal, 941, 109

Thielemann F.-K., et al., 2003, Nuclear Physics A, 718, 139

Toomre A., 1964, The Astrophysical Journal, 139, 1217

Toomre A., Toomre J., 1972, The Astrophysical Journal, 178, 623

Travaglio C., Hillebrandt W., Reinecke M., Thielemann F.-K., 2004, Astronomy & Astrophysics, 425, 1029

Tremaine S., Weinberg M. D., 1984a, Monthly Notices of the Royal Astronomical Society, 209, 729

Tremaine S., Weinberg M. D., 1984b, The Astrophysical Journal, 282, L5

Trick W. H., 2022, Monthly Notices of the Royal Astronomical Society, 509, 844

Vasiliev E., Valluri M., 2020, The Astrophysical Journal, 889, 39

Villa-Vargas J., Shlosman I., Heller C., 2010, The Astrophysical Journal, 719, 1470

Vogelsberger M., Genel S., Sijacki D., Torrey P., Springel V., Hernquist L., 2013, Monthly Notices of the Royal Astronomical Society, 436, 3031

Vogelsberger M., et al., 2014, Nature, 509, 177

Walcher C. J., et al., 2014, Astronomy & Astrophysics, 569, A1

Walmsley M., et al., 2022, Monthly Notices of the Royal Astronomical Society, 509, 3966

Wegg C., Gerhard O., Portail M., 2015, Monthly Notices of the Royal Astronomical Society, 450, 4050

Weinberg M. D., 1985, Monthly Notices of the Royal Astronomical Society, 213, 451

Weinberg M. D., 1992, The Astrophysical Journal, 384, 81

Weinberg M. D., 2025, The Open Journal of Astrophysics, 8, 70

Weinberg M. D., Katz N., 2002, The Astrophysical Journal, 580, 627

Weinberger R., et al., 2017, Monthly Notices of the Royal Astronomical Society, 465, 3291

Weinberger R., et al., 2018, Monthly Notices of the Royal Astronomical Society, 479, 4056

Weiner B. J., Sellwood J. A., 1999, The Astrophysical Journal, 524, 112

Weiner B. J., Sellwood J. A., Williams T. B., 2001, The Astrophysical Journal, 546, 931

Wetzel A., et al., 2023, The Astrophysical Journal Supplemental Series, 265, 44

White S. D. M., Frenk C. S., 1991, The Astrophysical Journal, 379, 52

Williams T. G., et al., 2021, The Astronomical Journal, 161, 185

Wylie S. M., Clarke J. P., Gerhard O. E., 2022, Astronomy & Astrophysics, 659, A80

Yurin D., Springel V., 2015, Monthly Notices of the Royal Astronomical Society, 452, 2367

Zana T., Dotti M., Capelo P. R., Mayer L., Haardt F., Shen S., Bonoli S., 2018, Monthly Notices of the Royal Astronomical Society, 479, 5214

Zhang H., Belokurov V., Evans N. W., Kane S. G., Sanders J. L., 2024, Monthly Notices of the Royal Astronomical Society, 533, 3395

Zheng Y., Shen J., 2025, The Astrophysical Journal, 979, 60

Zimmer P., Rand R. J., McGraw J. T., 2004, The Astrophysical Journal, 607, 285

Zou Y., Shen J., Bureau M., Li Z.-Y., 2019, The Astrophysical Journal, 884, 23

de Sá-Freitas C., et al., 2025, Astronomy & Astrophysics, 698, A5

van der Kruit P. C., 2007, Astronomy & Astrophysics, 466, 883